Computational Fluid Dynamics Modeling of a Two-Step Ethanol Oxidation Mechanism in a Supercritical Water Oxidation Reactor

Dzaki Pahlevi

A thesis

submitted in partial fulfillment

of the requirements for the degree of

Master of Science

University of Washington

2026

Committee:

Igor V. Novosselov

John C. Kramlich

John Palmore Jr.

Program Authorized to Offer Degree:

Department of Mechanical Engineering

University of Washington

Abstract

Computational Fluid Dynamics Modeling of a Two-Step Ethanol Oxidation Mechanism in a Supercritical Water Oxidation Reactor

Dzaki Pahlevi

Chair of the Supervisory Committee:

Igor V. Novosselov

Department of Mechanical Engineering

Supercritical water oxidation (SCWO) reactors are used to destroy recalcitrant chemicals, including perfluoroalkyl substances (PFAS). Addition of fuel enables autogenic operation, where heat is generated to achieve the reaction temperature necessary for PFAS destruction in a SCWO reactor. This study utilizes a Computational Fluid Dynamics (CFD) model of a two-step ethanol oxidation mechanism to gain insight into the operation of the University of Washington (UW) continuous-flow SCWO reactor. The reactor uses ethanol as a fuel and compressed air as an oxidant. Compared to the single-step mechanism, the global two-step reaction mechanism is expected to yield a more accurate temperature distribution and reaction zone characterization and can be validated against the experimental data that includes O_2, CO, and CO_2 measurements at the reactor exit. However, the use of a two-step ethanol oxidation mechanism in continuous-flow reactors under a wide range of reaction temperatures (475- 650 °C) has not been reported in the literature. The development of the two-step ethanol oxidation mechanism and its validation in a laboratory-scale system are

useful for optimizing SCWO for the destruction of recalcitrant compounds and reactor scale-up.

The CFD model of ethanol oxidation in a continuous-flow UW SCWO reactor is based on the two-step mechanism published by Helling et al. [1]. The model simulates ethanol oxidation under four different fuel loadings. The baseline case (100% loading) uses the injection of a 5% molar ethanol/ water mixture, which corresponds to a fluid temperature of 650 °C. Experimentally, the fuel injection rate was varied in the 49-100% range, resulting in fluid temperatures of 475- 650 °C. These conditions were modeled using a perfectly stirred reactor and in 2D axisymmetric CFD simulations to study the fluid flow, species, and temperature distribution inside the reactor.

The reaction temperature and incomplete products of decomposition from the PSR and CFD simulations were compared with the experimental data. The predicted reaction temperatures from the CFD model agreed within ~9% with the temperature measurements from the experiment, and the CO concentrations in the exhaust – within ~28% across all test cases. The two-step mechanism is an improvement of the single-step global kinetic allowing to gain insight into oxidation. The approach can be further validated based on the temperature measurements, but also on the CO and O2 data over a wide range of operational conditions.

Keywords: CFD, SCWO, ethanol, supercritical water oxidation, two-step mechanism, modeling

Table of Contents

List of Figures

List of Tables

Nomenclature

A	=	Arrhenius pre-exponential factor
A_1, A_2	=	Pre-exponential factor, reaction step 1 / step 2
C	=	Concentration of combustible species
c_p	=	Specific heat capacity
D	=	Hydraulic diameter
Ea	=	Activation energy
Ea_1, Ea_2	=	Activation energy, reaction step 1 / step 2
f	=	Flow rate percentage (per case)
F_x, F_r	=	Body force, axial / radial direction
Gr	=	Grashof number
h_0	=	Reference/standard enthalpy
htf	=	Heat transfer factor
J_i	=	Diffusion flux of species i
k	=	Thermal conductivity
k_{eff}	=	Effective thermal conductivity
$\dot{m}$	=	Mass flow rate
$\dot{m}_{air}$, $\dot{m}_{H2O}$, $\dot{m}_{oxidant}$	=	Mass flow rate, air / water / oxidant stream
m, n	=	Reaction order (species-dependent)
M_w	=	Molecular weight
p	=	Pressure
Q_{air}	=	Air volumetric flow rate
R	=	Universal gas constant
Re	=	Reynolds number
r_1, r_2	=	Reaction rate, step 1 / step 2
S_h, S_i, S_m, S_φ	=	Source term (energy, species, mass, general scalar)

T	=	Temperature
t_{res}, τ_{res}	=	Residence time
$\tau_{apparent}$	=	Apparent residence time (CFD model)
u, u_x, u_r	=	Velocity (general, axial, radial)
U_∞	=	Freestream velocity
x_i	=	Mole fraction of species i
Y_i	=	Mass fraction of species i
y^+	=	Non-dimensional wall distance
Δs	=	Maximum near-wall element width
μ	=	Dynamic viscosity
ρ	=	Density
σ	=	Collision diameter (Lennard-Jones)
φ	=	Equivalence ratio
φ_{ij}	=	Viscosity/thermal conductivity interaction parameter
Ω	=	Collision integral (Lennard-Jones)
ω	=	Specific dissipation rate (k-ω turbulence model)
C_2H_5OH	=	Ethanol
O_2	=	Oxygen
N_2	=	Nitrogen
CO	=	Carbon monoxide
CO_2	=	Carbon dioxide
H_2O	=	Water
i, j	=	Species index

PFAS	=	Per- and polyfluoroalkyl substances
SCWO	=	Supercritical water oxidation

CFD	=	Computational fluid dynamics
SST	=	Shear stress transport (turbulence model)
NIST	=	National Institute of Standards and Technology

Acknowledgments

I would like to express my deepest gratitude to my parents, Reza Shah Pahlevi and Eva Zhoriva Yusuf, and my little brother, Nabil Pahlevi, for the everlasting support and prayers they have given me from back home since the very beginning of my journey in America.

I want to give my sincerest gratitude to Professor Igor Novosselov for his instrumental mentorship on my research and graduate studies. I also would like to extend my gratitude to my committee members: Professor John Kramlich and Professor John Palmore Jr. for their valuable guidance and review on my work. I would also like to thank my graduate advisor, Jane Park, and my Responsible Officer, Sophia Schuessler, for supporting my studies.

I also want to thank all of my labmates in the Novosselov Research Group (NRG) for being my source of inspiration and for making this lab feel like my home away from home. I would like to specifically thank Anmol Laxmankumar Purohit for having mentored me throughout this research and for having been my moral support in the lab. I would also like to thank Shuyuan Bai, who provided me with the experimental data that I referred to in this study and taught me about supercritical water oxidation. I am also grateful to Benjamin Price, who introduced me to the lab, taught me a great deal about fluid dynamics, and set up the computational resources necessary for this research. Finally, I would like to thank Holle Lam for being my informal mentor throughout my studies in mechanical engineering. You guys are truly great people I look up to.

To all my friends who have personally supported me during my graduate studies in America, I sincerely thank you. I would like to specifically thank my best friend and mentor, Satria Ardianuari, for his constant moral and academic support for me, especially during the hard times. Thank you to my best friends, Kaiyuma Raihan, Kevin Theodore, Theresia Brigita, Vito Kemas, and Vira Tias, for being my moral support from Indonesia. I also want to thank Audrey Dwinandita and Ghovindo Siadari for personally supporting me in Seattle.

Chapter 1. Introduction

1.1. Perfluoroalkyl substances (PFAS)

Per- and polyfluoroalkyl substances (PFAS) are a family of toxic compounds found in industrially manufactured products. PFAS are the active ingredients of fluorosurfactants and are commonly used as an ingredient to manufacture everyday products such as food packaging, nonstick cookware, stain-proof clothing, cosmetics, pesticides, and firefighting liquids [2], [3], [4] because of their desirable chemical properties that impart oil and water repellence, friction reduction, and temperature resistance [5]. PFAS can chemically accumulate and persist in the human body and the environment. For this reason, PFAS are termed “forever chemicals” [4].

United States National Institute of Environmental Health Sciences (NIH) [3] and multiple studies [4-7] have identified multiple health effects associated with PFAS exposure in humans, among them are cancer, liver and kidney diseases, hormone dysregulation, and fertility disorders. PFAS are most likely to be exposed to humans through dietary intake such as food and water [2, 3] and are becoming increasingly present in outdoor environments such as soil and water.

In the United States, PFAS contamination in form of particulate matter has been reported to be present in tap water and other water supply used for drinking, which carries the highest risk of exposure to humans [2, 3].The presence of PFAS in the environment, especially in ground and tap waters generates the urgency for PFAS remediation and destruction technologies [8].

1.2. Supercritical water oxidation (SCWO) with ethanol oxidation

Several end-of-life PFAS destruction technologies have been investigated and reported, such as electrochemical oxidation [9, 10], plasma treatment [11], photocatalysis [12, 13], sonochemical treatment [14], mechanochemical degradation [15-17], and hydrothermal

technologies [18], such as alkaline hydrolysis AH and supercritical water oxidation (SCWO) [19-22]. The hydrothermal technology benefits from operating in a close vessel environment, allowing for process control to avoid product of incomplete decomposition. Alkaline hydrolysis has been shown to fully mineralize PFAS under high-temperature high-pH conditions in a compressed liquid water environment (T = 200-374 °C, P = 10-25 MPa). [23-29]. However, destruction of perfluoroalkyl sulfonic acids (PFSAs) like PFOS requires high temperatures (T~350 ºC) and high levels of alkali (~ 3 M NaOH), which increase the operational cost and pose challenges associated with corrosion and effluent neutralization.[28, 30]

Supercritical water oxidation (SCWO) technology operates at high temperature and high pressure (T > 374 °C, P > 22.1 MPa) and leverages the high miscibility of organics with supercritical water (SCW) [31, 32]. This enables fast volumetric reaction chemistry, not limited by diffusion rates [33]. With addition of oxidizer, all organic contaminants (including PFAS) are rapidly oxidized to inorganic species, including CO_2, F^-, and water [34]. The SCWO chemistry of SCWO is similar to combustion. It is driven by free-radicals such as OH•, O•, and H•.

SCWO is well suited to treat wet hazardous and PFAS wastes, with high destruction and removal efficiencies (DRE>99%) and mineralization of organic contaminants at short residence time and temperatures greater than 600°C. Recent reports show that the SCWO process can effectively destroy neat PFAS [35, 36], simple PFAS matrices, e.g., AFFF [37, 38], environmental matrices [39, 40]. The literature also reports high conversion of recalcitrant nitrogen organics [41-48]. These findings underscore the potential of SCWO as a comprehensive method for PFAS destruction underscoring the advantages to SCWO for end-of-life PFAS treatment, [18, 38-40, 49]. However, the reaction routes, elemental reaction rates, temperatures, are still poorly understood [50]. Insights into the reaction kinetics and mechanisms, the effect of mixing rates (specific to reactor design), and fluorine fate, i.e., the

mass balance among reactants, intermediates, and products, are needed to optimize conditions for robust remediation and treatment.

The range of temperature (380-600 °C) also prevents the formation of NOx and SOx compounds which are highly toxic [51]. Previous notable studies of PFAS destruction using SCWO [19, 38, 52] have shown that SCWO processes with continuous flow reactor are able to achieve very high destruction rates and emphasized the importance of obtaining high reaction temperatures and high influent feed volume for the reactor [28, 52].

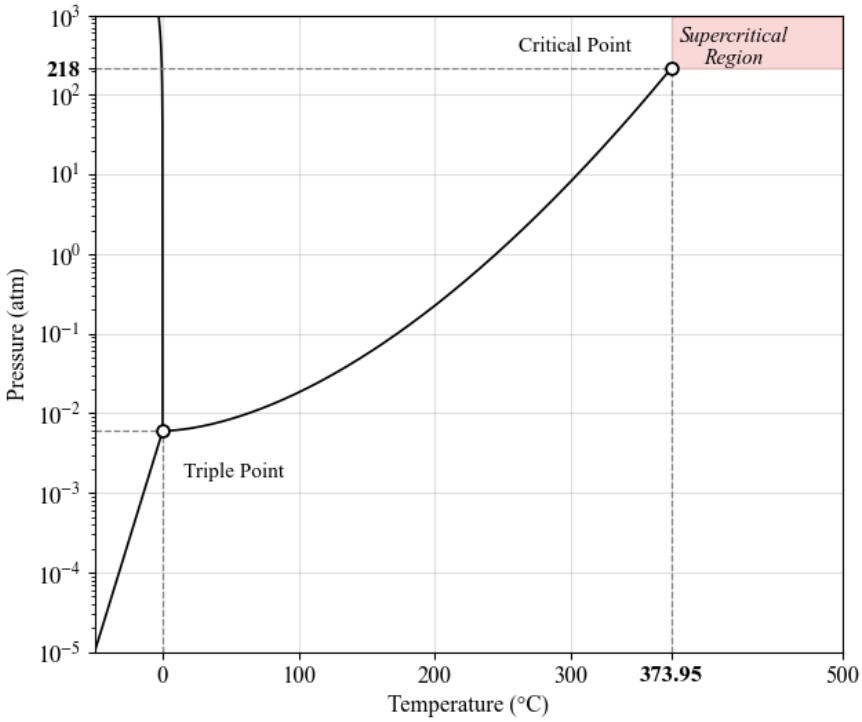

Figure 1. Phase diagram of water, showing the supercritical phase.

The UW lab scale SCWO reactor of interest in this study utilizes ethanol as the injected fuel, which generates heat for the reaction and achieves the high temperatures necessary for PFAS destruction through ethanol oxidation. Both concurrent studies done by Li et al. and Austin et al. [19, 52] provided the proof of concept for the high- efficiency degradation of

PFAS compounds in a volumetric autogenic SCWO reactor with ethanol as the auxiliary fuel and achieved >99% destruction rate.

SCWO has main advantages compared to other emerging PFAS destruction technologies in terms of its high destruction rates for PFAS for larger volumes and a relatively shorter residence time [19, 28]. The main documented disadvantage of SCWO processes are their low operational volumes due to their high requirements for high pressures and temperatures dealing with large volumes of substrates and the occurrence of salt formation within the reactors [51].

To advance SCWO technology for broad and robust deployment, the most research needs include: (i) temperature and reaction time requirements for specific PFAS species mineralization and desired treatment endpoints, (ii) impacts of oxidant concentration and feed stream composition, (iii) propensity for reactor fouling and plugging by inorganic compounds non-soluble in supercritical water, as a function of operating conditions and reactor design [53, 54].

1.3. CFD modeling approach on SCWO reactors

Successful scale-up of SCWO reactors can be assisted by numerical reactor models, validating these models against the available data, and then using the models to simulate the larger reactor's performance [55]. CFD modeling can be used for design and process optimization, as demonstrated by multiple studies [33, 55-58].

Efforts in optimizing the design and upscaling of SCWO reactors require thermophysical and chemical characterization. One approach to achieve such characterization is computational fluid dynamics (CFD) modeling. CFD is a fluid dynamic, thermophysical and chemical modeling method that can describe various fluid and chemical states within a system at any specified condition, such as fluid flow dynamics, temperature profiles, species distribution, and chemical reactions. CFD modeling achieves this by numerically solving fluid

flow and thermophysical mass, momentum, energy, and species transport balance equations across the modeled system.

Ethanol oxidation serves a purpose to generate heat to achieve the reaction temperature necessary for PFAS destruction in the SCWO reactor. Since PFAS destruction using SCWO is highly dependent on temperature, modeling the ethanol oxidation for SCWO will provide insights into the thermodynamic and reaction behavior necessary for the future design and upscaling of SCWO for PFAS destruction.

The insights into the reactor operation, such as temperature profiles of the fluid, the reactor components (wall, liner, injectors, etc.), and the spatial distribution of reacting species during the ethanol oxidation process are important in the reactor design and optimization of its operational parameters, which are essential in upscaling. Such insights can be provided by CFD modeling.

Novosselov Research Group (NRG) of the University of Washington has built and experimentally tested a lab-scale continuous flow SCWO reactor which was able to achieve temperatures ~700C and PFAS DRE>99.999% [19, 52]. At the time of writing the reactor has been operated for over 5000 hours. Purohit et al. [33] carried out a CFD modeling for the ethanol oxidation of the UW SCWO reactor using a single-step global kinetic rate. The study has also developed the thermodynamic polynomial fits for water transition that could be used in the CFD simulations. The model has been validated as it was able to provide temperature profiles, species distribution, and fluid flow dynamics to a good accuracy; however, validation with CO data could not be made.

1.4. Study motivation – SCWO two-step ethanol oxidation mechanism

There is a need for a high-throughput SCWO reactor characterization for its design improvement and upscaling. The modeling and characterization of SCWO reactors with ethanol oxidation, especially in continuous flow and inverted gravity arrangement under the

relevant conditions necessary for PFAS destruction, have not been well-studied in literatures [55-58]. The single-step ethanol oxidation mechanism in SCWO was limited in terms of the accuracy of the temperature distribution and the presence of intermediate species compared to the actual scenario observed in the experiments [33]. In the single-step mechanism, ethanol oxidation happens on the fastest reaction pathway, which limits the hotter fluid from spreading further along the reactor. The intermediate species of CO was also not able to be modeled under the single-step mechanism. CO is important because it is a rate-limiting intermediate, where its absence can overpredict the conversion or underpredict the residence time compared to experimental data [1]. The presence of CO is also helpful to improve the accuracy of temperature distribution, because the magnitude of heat release is controlled largely by the location and the rate of CO oxidation [59].

However, the modeling of continuous downflow SCWO reactors with a two-step ethanol oxidation mechanism has not been well studied and validated with existing experimental data. Hence, the motivation of this study is to present and validate a CFD model for a two-step ethanol oxidation mechanism inside the UW SCWO reactor to better characterize its fluid flow and temperature distribution.

1.5. Study needs and objectives

This study addresses the gap of validating CFD models of the SCWO process with experimental data. Modeling the two-step ethanol oxidation for SCWO is an effort to improve the prediction of thermodynamic and reaction behavior necessary for the future design and upscaling of SCWO for PFAS destruction. Ethanol oxidation serves a purpose to generate heat to achieve the reaction temperature necessary for PFAS destruction. The current study does not model PFAS destruction, which is intended to be the focus of future work.

The objective of this study is to characterize the fluid flow and thermodynamics of ethanol oxidation in the UW SCWO reactor using a CFD model and to validate the two-step

ethanol oxidation mechanism against experimental data. The points of interest are the temperature profiles, species distributions, and bulk fluid interactions with the injection of fuel and oxygen under multiple reaction operating conditions. Another objective is to study the applicability of the global two-step kinetic model of Helling et al [1], which was developed for a temperature range of 400-500 °C, to the temperature range of 475-650 °C. .

Chapter 2. Literature Review

2.1. PFAS destruction technologies

There have been many efforts to develop PFAS destruction methods [51], [60]. A study conducted by Leung et al. surmised that conventional water and wastewater treatment facilities are not capable of removing PFAS, with the main reason being that PFAS effluent concentrations can be significantly higher when compared to influent levels due to PFAS-like precursor compounds breaking down within such treatment systems [51], [60], [61], [62], [63]. Therefore, new methodologies in contrast of conventional wastewater treatment technologies are needed for PFAS removal and destruction. Even though destructive technologies are still in the development stage, they have shown great promise to destroy PFAS compounds and provide a solution to effectively address society's urgent need to remediate this harmful family of chemical compounds [51].

A study carried out in 2022 by Meegoda et al. [51] has described some of the most promising technologies that are currently in the development stage. Some of the technologies presented in the review are still under development at the lab scale, while others have already been tested in the field. Table 2.1 summarizes the working principles, advantages, and disadvantages of each method. Despite extensive published experimental and numerical research on the degradation or mineralization of PFASs, there are still major gaps in the experimental and numerical data, which makes it challenging to perform a complete evaluation of the efficiency of those technologies and there is an urgent societal need to investigate cost-effective and safe PFAS mineralization technologies with minimal adverse environmental impacts [51].

Table 2. 1. Summary of PFAS destruction technologies

No.	PFAS Destruction Technology	Working principle	Advantages	Disadvantages
1	Electrooxidation (EO)	Applies an electrical current through a conductive solution between an anode and a cathode, PFAS are then either adsorbed and degraded at the electrode or in the liquid medium [60], [64].	- High destruction rate of long-chain PFAS [64-67]. - Capable to operate at low temperature and small volume [60, 64]. - Does not require additional chemicals for post-treatment [68].	- Difficult to destroy short-chain PFAS and even increases its concentration [62, 69]. - Only efficient on low PFAS concentrations. - High energy consumption - High initial costs of electrodes [62, 68].
2	Plasma discharge	Forces the PFAS molecules to bond with ionized gases created from the water [60].	- Able to effectively remove both short and long-chain PFAS. - Less sensitive to presence of other organic and non-organic contaminants [70].	- Sensitivity to some characteristics of contaminated water such as pH, the concentration of OM, and the nitrate concentration [71].
3	Photocatalysis	Breaks down PFAS with the help of photosensitive substances within the mixture which are excited by light [72].	- Able to be performed at ambient temperature. - Low energy consumption [12].	- Low destruction rate. - Generates toxic intermediate reaction products [60]. - Difficult recovery of the photocatalyst [73].
4	Sonolysis	Adsorbs PFAS into bubbles, then uses an acoustic field to induce implosion of the vapor bubbles at a very high temperature with the help of pyrolysis [74].	- High PFAS destruction rates [75].	- High energy consumption and costs. - Low power density. - The physicochemical properties are not well studied which hinders scalability [51].
5	Hydrothermal alkaline treatment (HALT)	Utilizes alkaline amendment under high pH, high pressure (>25 MPa) and moderately high temperature (>350 °C) to destroy PFAS [18].	- High destruction rates [18]. - Lower energy use [18].	- Long residence times to achieve 99% PFAS destruction [18] which hinders scalability.
6	Thermal degradation/incineration	Subjects PFAS to high temperatures and exposure to fire.	- High destruction rates for both long and short-chain PFAS [51]. - The technology is widely available for adaptation in already built incinerator facilities.	- Formation of smaller PFAS after incineration [76]. - Any incineration forms byproducts such as bottom ash, which contains non-combusted gases and volatile products which are proven to be problematic [77].
7	Supercritical water oxidation (SCWO)	Utilizes supercritical water to oxidize PFAS substrates.	- High destruction rates for larger volumes of PFAS [78], [19] - Shorter residence times to achieve high destruction rate [33]. - Lower environmental consequences due to absence of toxic byproducts.	- High energy demand [33, 51, 78]. - High material costs. - Low operational volume [51]. - Precipitation of salts [79].

SCWO has main advantages compared to other emerging PFAS destruction technologies in terms of its high destruction rates for PFAS for larger volumes, relatively shorter residence time, and high opportunity for scalability. Compared to thermal incineration, which also allows large volumes of PFAS destruction, SCWO produces less harmful waste byproducts to the environment. Compared to alkaline hydrolysis (aka HALT), SCWO can treat larger volumes of PFAS and achieve high destruction rates at lower residence time [33], [19]. Compared to EO, Sonolysis, Photocatalysis, and plasma discharge methods, SCWO can achieve higher PFAS DRE and mineralization, and it works well with more concentrated PFAS feeds (e.g., AFFF, foam fractionate) and offers greater opportunity for upscaling. The advantages of SCWO make it an attractive PFAS destruction technology.

A known disadvantage of SCWO is its operational volume. Meegoda et al. [51] reported that currently, it is not economically viable to work with volumes higher than 50,000 gallons/day of dilute waste streams. The high costs involved in heating and pumping large volumes of waste streams threaten the scalability of SCWO reactors [33], [51], [78]. An additional issue with SCWO reactors is the precipitation of salts [79]. Thus, treatment of high-concentration waste streams and legacy AFFF can be the best application for SCWO.

2.2. Previous experiments on SCWO reactors to treat PFAS

Supercritical water oxidation (SCWO) is one of the emerging PFAS destruction technologies that will be studied in this thesis. SCWO utilizes supercritical water, which is water at high pressure and temperature, to oxidize PFAS substrates. Compared to the other described emerging PFAS technologies, SCWO has a significant advantage in its destruction rate of larger volumes of PFAS [78], its capacity for continuous-flow reaction, which allows high-throughput destruction, lower environmental consequences, and might be more directly scalable reactor upscaling compared to other processes. The mechanism, advantages, and disadvantages of SCWO will be discussed in detail in the next section.

Krause et al. [38] conducted three sets of experiments in a continuous flow SCWO reactor treating diluted AFFF. Throughout this test, the maximum reactor temperature was maintained at 590 °C, and the reactor operation pressure was set at 24 MPa. The maximum reactor temperature was 595 °C with a feed rate of 0.35 kg/min and a reactor residence time of 6–8 s. The analysis of PFAS in the liquid influent and effluent was conducted by high-performance liquid chromatography followed by tandem mass spectrometry. The overall destruction efficiency was found to be greater than 99%. In all cases, the effluent PFAS concentrations were greater than the EPA drinking water health advisory limit (70 ng/L) or state-level limits. This finding pushed the hypothesis that SCWO needs to operate at higher reaction temperatures or higher residence times to achieve satisfactory levels of PFAS destruction.

Austin et al. [19] conducted a PFAS destruction experiment using UW SCWO with a bench-scale continuous flow reactor. Four influent streams introduce the reagents into the reactor: ethanol-water solution, compressed air-water mixture, PFAS-water solution, and a liquid water injection near the reactor exit. The SCWO treatment results in a DRE~99.999% at a T > 610 ◦. Fluoride recovery lags destruction of PFAS at 510ºC and at a residence time of ~30 s. C and reaches >100% above 610º, confirming the formation of liquid and gaseous phase intermediate products during lower temperature oxidation. The experiment concluded that PFAS destruction and removal efficiencies increase with temperature. It was found that destruction rates are low during lower temperature operations.

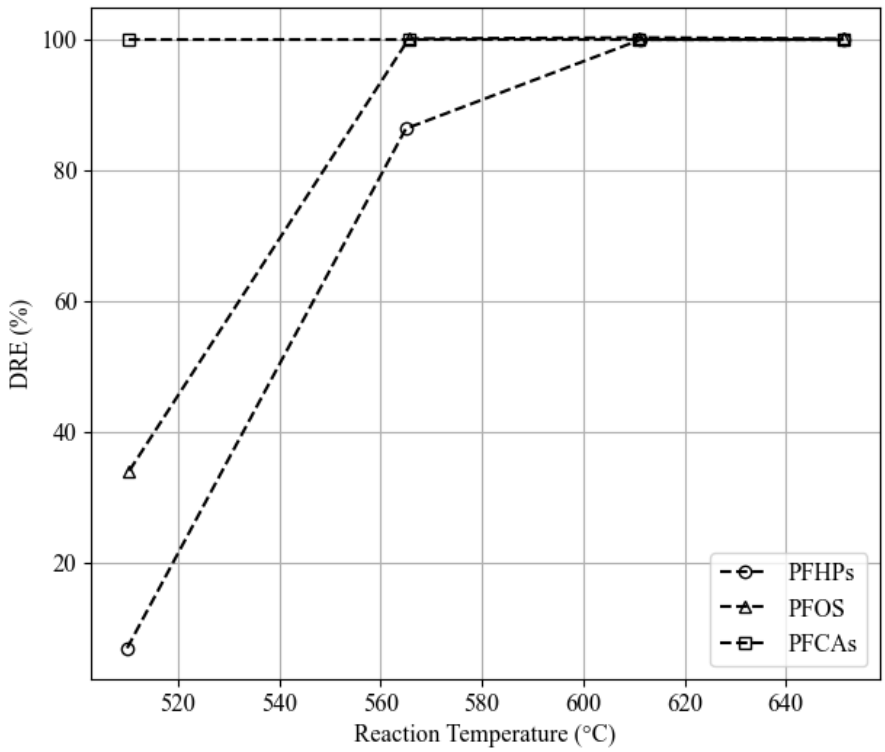

Figure 2. Destruction and removal rate (DRE) as a function of reaction temperature of a SCWO reactor (adapted from [19])

Li et al. [52] conducted an experiment on ammonia removal for PFOS, a PFAS compound, using the same setup of SCWO reactor that was used by Austin et al., using ethanol as the fuel and compressed air as the oxidant. The experiment reported the effects of auxiliary fuel concentration, preheating temperature, and excess air on the temperature distribution, stability, and operation of the lab-scale continuous flow SCWO system. High operating temperature (> 630 °C) was obtained when operating at subcritical injection temperatures in the reagent, fuel, and oxidizer lines. Moreover, the autogenic SCWO operation was achieved without preheating fuel and reagent when the initial concentration of ethanol reached 16.13 wt% in the fuel line; the exothermic heat generated from the oxidation of ethanol with air maintained the reaction operating in the supercritical condition (T = ~580 °C, P = 26.2 MPa) [52].

2.3. Reaction mechanisms and kinetics of SCWO using ethanol oxidation

In the SCWO process, organics containing only C, H, and O have a relatively simple transformation path, by which they can generate corresponding organic radicals and carboxylic acids, and are eventually converted into CO_2 and H_2O [80]. In actual ethanol oxidation, there can be hundreds of reaction steps which define the microscopic reactions of the intermediate species and radicals. Li and Kazakov [81] have reported 238 reversible elementary reactions and 39 intermediate species within the realistic ethanol oxidation reaction mechanism modeling under detailed oxidation and pyrolysis. The realistic reaction mechanism's purpose is to provide microscopic chemical kinetics.

Global empirical and semi-empirical reaction mechanisms are another set of models that provide macroscopic chemical kinetics. Although global kinetics are not able to provide detailed microscopic kinetics, they are able to inform macroscopic species formation, reaction zones, and reaction temperature distribution, which are useful for computational modeling because the brevity of the chemical steps simplify the amount of data needed for computational modeling and saves computational time while still able to provide useful information on how the reaction occurs within the reactor [33], [82], [83], [84].

Jiang et al. [80] conducted a literature review on mechanisms and kinetics for supercritical water oxidation processes. The reaction kinetics of SCWO have developed from empirical models to semi-empirical models and then to detailed chemical kinetic models (DCKMs). Empirical models, also known as global kinetics models, usually describe the laws of reaction through power exponential equations, which only involve the concentration changes of reactants rather than intermediates [80]. David et al. [85] and Anitescu [86] studied the empirical model of SCWO using ethanol, which was characterized using linear regressions. Although the oxygen concentration used as the input for the regression showed a mismatch against the stoichiometry, the kinetic rate obtained from the regression by David et al. was

shown to be consistent with Anitescu's findings, validating the consistency of the empirical mechanisms.

Semi-empirical models describe the SCWO process involving its intermediate species. Helling et al. [1] used this approach to model the two-step reaction which contains CO as the intermediary. Webley et al. [87] developed a global mechanism for methane oxidation in SCW on the basis of such a kinetic model. Methane was first converted to CO and H2O, and then CO was oxidized with O_2 to generate CO_2. The model well-predicted the changes in O2 and CO_2 concentrations during the reaction. Brock et al. [88] considered that formaldehyde was the initial reaction product and then converted to CO and CO_2. The concentration distribution expressions of each compound were obtained by solving the governing differential equation, which well-illustrated the basic characteristics of methanol SCWO. Pinkard [89] modeled the reaction mechanism for water-gas-shift gasification in supercritical water. The Arrhenius parameters for the gasification were able to be modeled by fitting the kinetic trends for a first-order decomposition reaction after obtaining the species yields for various temperatures, similar to the method used by Helling et al. Westbrook et al. [90] includes 21 elementary reactions and yields accurate predictions of oxidation rates for wet carbon monoxide under a wide range of combustion conditions. The elementary model predicted conversions of carbon monoxide to carbon dioxide slightly better than the best global model, typically being within a factor of 2 of the experimentally determined conversion [1]. The global, semi-empirical kinetic models have proven to be adequate to model the macroscopic phenomena occurring in SCWO reactions, as they yield results that are reasonably close with experiments [1], [33], [86], [88].

The detailed kinetic models (DCKMs), which contain hundreds of reaction steps, can reveal microscopic reaction mechanisms such as radical formation [80, 91]. The high temperature and pressure reaction conditions in SCWO make it difficult to apply some measurement techniques, creating a barrier to establishing DCKMs under SCWO conditions

[80]. However, the SCWO reaction process is similar to the gas-phase combustion process in some free radical reactions, and gas-phase combustion has developed numerous DCKMs for 25 of 44 organics. Currently, some scholars have developed DCKMs of various compounds based on gas-phase combustion [80].

Detailed reaction mechanisms and DCKMs create barriers in terms of reactor modeling, including the difficulty of applying measurement techniques to be used as a data feed for the modeling, the difficulty in physical chemistry characterization, and extensive computational modeling requirements. Empirical and semi-empirical models are more acceptable for modeling because of these challenges.

Although the aforementioned studies of empirical and semi-empirical models yield some inaccuracies in species predictions, they are expected to still be able to give a reasonable description of the occurring kinetics for chemistry modeling, including SCWO, in exchange for microscopical reaction accuracies [33], [19], [82, 83, 91].

2.4. Two-step ethanol oxidation for SCWO

To simplify the characterization of SCWO reactions using computational methods such as CFD, semi-empirical mechanisms have been investigated to determine the accuracy of the macroscopic physical and chemical phenomena. Empirical and semi-empirical mechanism models are relevant because they are expected to reduce computational processing times while still providing useful information on the physics and chemistry occurring within the reaction. The semi-empirical mechanism models provide a greater variety of intermediate species with each increase in mechanism steps. The simplest semi-empirical mechanism model for SCWO with ethanol oxidation is the global two-step ethanol oxidation mechanism.

The global two-step ethanol oxidation reaction mechanism involves the oxidation of ethanol into carbon monoxide (CO) and water, with CO as the intermediate species. The carbon monoxide is then oxidized one more step into carbon dioxide (CO_2) and water.

The global two-step ethanol oxidation reaction mechanism has been investigated using an experimental setup by Helling et al. [1] under the pressure of 25 MPa and the reactant temperature range of 400-500^0 C using a tubular continuous-flow reactor setup, which was designed to produce well-characterized data for the quantitative determination of reaction kinetics in supercritical water. The experiment used pure oxygen as an oxidant, and it was carried out using variable fuel and oxidant feed compositions. The experiment measured the concentrations of consumed fuel and oxidants and the product gases, which were then plotted against the chemical reaction mechanisms of two-step ethanol oxidation based on first principles to obtain the k-value of the reaction rates for the temperature range of 400-500^0 C. The resulting data were then subjected to linear regression to obtain the global rate of two-step ethanol oxidation kinetics, with uncertainties that were given as standard deviations due to the limited number of data points used in the experiment [1].

The obtained rates for the two-step ethanol oxidation by Helling et al. have uncertainty bounds within a small range to account for the variability of operating conditions within these temperature and pressure ranges. A set of 59 experiments with carbon monoxide and supercritical water confirmed that the two-step reaction pathway can describe ethanol oxidation. It was also observed that the oxidation of carbon monoxide is inhibited by the presence of other hydrocarbons in gas-phase combustion due to competition for hydroxyl (OH) radicals.

In this study, the existing SCWO reactor is modeled using the two-step kinetic rate to investigate its applicability and validity under the different SCWO operating conditions.

2.5. University of Washington SCWO reactor

The Novosselov Research Group (NRG) at the University of Washington has built a SCWO reactor for the purpose of PFAS destruction. The SCWO reactor is an inverted gravity vertical reactor with 30 mm in length. The reactor has coaxial inlets for injecting fuel and air.

The fuel and oxidant enter the reactor through different lines, and both can be preheated before entering the reactor. The SCWO reactor has two influent lines: (1) ethanol−water mixture and (2) oxidant−water mixture. The previous experiments have used ethanol and methanol as fuel, hydrogen peroxide and compressed air as an oxidant.

Waters 515 high-performance liquid chromatography (HPLC) pumps continuously introduce the influent streams into the reactor at preset flow rates. The reactor can sustain pressure up to 30 MPa and temperatures as high as 700^0 C. The inner liner of the reactor is made of titanium, and the nozzle is constructed from Inconel 625, a nickel-based alloy commonly used in SCWO systems to resist oxidative corrosion and provide structural performance at elevated temperatures. Reactor dimensions were determined based on commercially available tubing and off-the-shelf fittings rated to the operating temperatures and pressures [78]. As demonstrated by the previous experiments and characterizations carried out with the UW SCWO reactor [19, 52, 78], the reactor can achieve a high PFAS destruction rate (>99.9%), with the destruction levels increasing with reaction temperature.

2.6. Previous CFD model of UW SCWO reactor

Purohit et al. [33] modeled a global single-step supercritical water oxidation using ethanol as fuel and hydrogen peroxide as oxidant in the existing SCWO reactor under conditions of 25 MPa and an incoming reactant temperature of 400˚C, using a 2D axisymmetric model with hydrogen peroxide as the oxidant, while varying the incoming fuel percentage. The computational domain comprises a fluid volume representing the reactor zone and solid volumes to simulate heat transfer through the reactor's walls. In this model, the gravity term is modeled to capture the effects of buoyancy due to temperature gradients causing bodily forces of fluid flow. Due to exceptional reaction stability, inverted gravity reactors have been used to study chemical reactions and particle formation mechanisms.[92-99] The modeling approaches that use the k-ω turbulence model were shown to be in good agreement with experimental data.

The initial effort utilized a global single-step mechanism of ethanol oxidation with the reaction kinetics proposed by Schänzenbacher et al. [100]. The reacting species were modeled as a single-phase mixture. The thermophysical properties of the species were modeled using a piecewise polynomial fit based on the NIST data. The reacting species were modeled as mass-weighted average in terms of their densities and specific heat constants. The computational grid consisted of ~285 000 elements after an independent mesh study. The flow rate of water through the oxidant line is held constant at 10 mL/min, while the flow rate of water through the fuel line is varied, changing the overall concentration of ethanol. The global equivalence ratio is kept constant at 1.1 for all fuel loadings. To reduce the number of species, hydrogen peroxide was simplified so that the oxidant inlet only has O_2 and H_2O at the decomposition rate of hydrogen peroxide.

The model predicted the temperature distribution and local reaction rates within the SCWO reactor. Across all fuel percentages, the predicted temperatures were shown to be in good agreement with experimental data. The model also compared the results of using the finite-rate and eddy dissipation models. Both EDC and finite rate predict similar temperatures within 3 °C at the midpoint of the reactor. The most observable difference between the temperature predictions is in the primary fuel oxidation region (~25 mm from the nozzle). Indicating that turbulent mixing in EDC has slower heat release in the jet region.

The study provided a baseline of the chemical properties, thermodynamics, and hydrodynamics model that shall be used as a model for this thesis. However, it was recognized that the single-step mechanism underpredicts the length of the reaction region within the reactor [80]. In a two-step global mechanism, CO production influences the primary heat release [59], [83]. Since CO has been reported experimentally, the exhaust measurements can be used to tune the model [101]. Therefore, the motivation of the current study is to model a two-step ethanol oxidation mechanism that incorporates delayed reaction and CO formation, which is

expected to be an improvement in temperature distribution predictions and flow characterization within the reactor.

2.7. Global two-step reaction mechanism of SCWO ethanol oxidation

Helling et al. [1] experimentally investigated the global kinetic rate for a two-step ethanol oxidation under the pressure of 25 MPa and the reactant temperature range of 400-500^0 C. A tubular continuous flow reactor system was designed to provide characterization data for the quantitative determination of the kinetics. The system includes a fluidized sand bath, gas supply tanks, feed pumps, and a gas – liquid separator. Dilute inlet concentrations of combustibles (ammonia, carbon monoxide, and ethanol) and oxidant (oxygen) were used in this system. The feed solutions (combustibles and oxidants) were preheated and pressurized before entering the reactor through a narrow channel.

Reactor conditions for the experiments ranged in temperature from 397 – 541 °C at a nominally constant pressure of 24.6 MPa and a mass flow rate of 1.67 × 10^4 kg/s or 10 g/min. This flow arrangement yielded a typical Reynolds number of 3100 ± 400 in the reactor (turbulent flow) and residence times between 6 and 14 s. The inlet concentrations of the oxidant and combustibles were varied to provide datasets for a range of different feed concentrations.

The measured quantities in all experiments included the system temperatures and pressures, gas and liquid flow rates, gas-phase composition, and specific concentration of the species in the liquid phase. The calculated quantities are the reactor residence time, concentrations at the inlet and outlet, reactant conversion, an apparent first-order rate constant, average reaction rate, and solubilities in the saturators. The measured concentrations of the reaction products are then used as an input to the oxidation reaction Arrhenius model. The form of the global expression for oxidation reactions was assumed as

$$\frac{-dC}{dt} = A \exp\left(-\frac{E_a}{RT}\right)[C]^a[O_2]^b[H_2O]^c \quad (1)$$

Where A = preexponential factor $(L/mol)^{a+b+c}$ s^{-1}, [C] = concentration of combustible species, Ea = activation energy (kJ/mol), R = universal gas constant (8.31 kJ/mol), T = absolute temperature (K), and a, b, c = reaction orders.

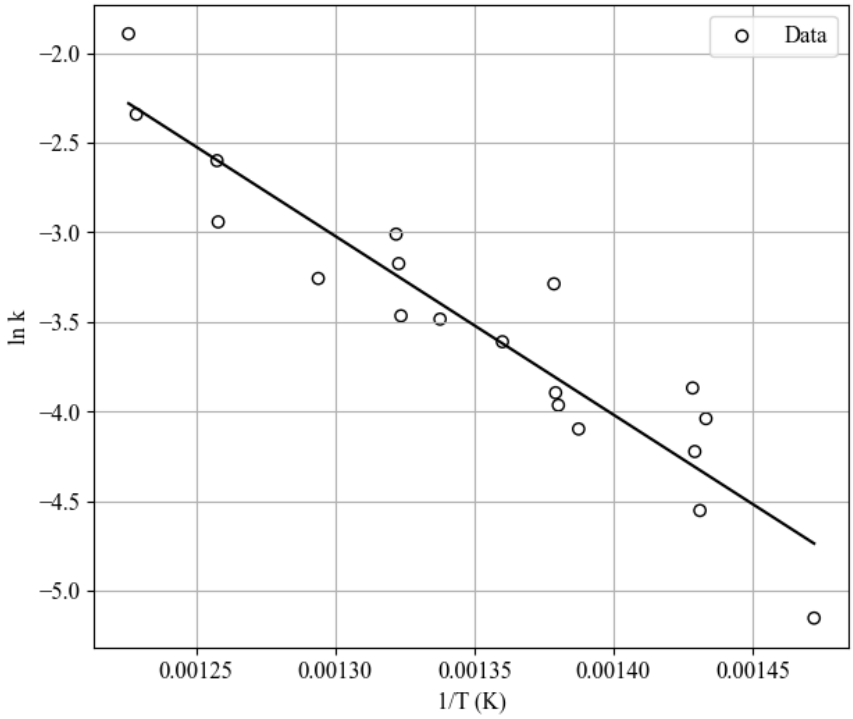

Figure 3 . Arrhenius temperature dependence of CO oxidation (adapted from [1])

The Arrhenius temperature dependence of the reaction was determined by plotting the natural log of the first-order rate constant k^* (s^{-1}), calculated from the measured rate with a=1, b=0, and c=0 versus the reciprocal absolute temperature. The slope yielded from this modeling is the apparent Ea, and the intercept yielded the preexponential constant. The uncertainties are given as standard deviations because of the limited number of data points.

Figure 3 shows the plot of the first-order oxidation of CO. Oxidation of CO can occur in two pathways, a direct oxidation pathway and a water-gas shift pathway. A Gauss-Newton

nonlinear optimization technique was used to determine the best fit equation for the global CO oxidation rate in supercritical water, to obtain the A, Ea, and the reaction order values. This regression was obtained to be

$$\frac{-dCO}{dt} = 10^{7.25\pm0.53} \exp\frac{(-120 \pm 7.7)}{RT}[CO]^{1.014\pm0.09}[O_2]^{0.03\pm0.04} \quad (2)$$

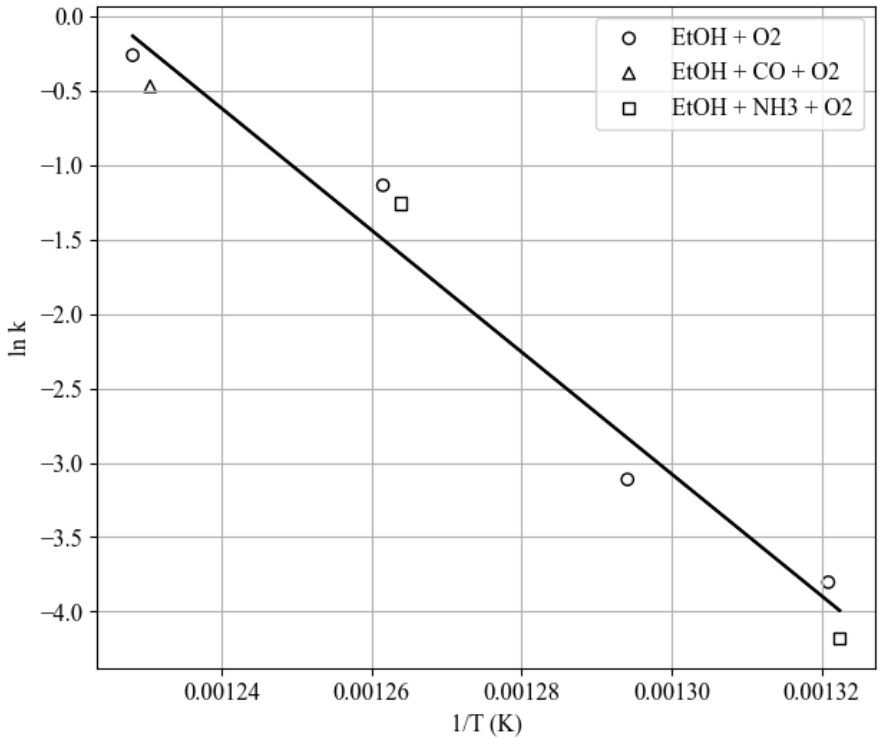

Figure 4. Arrhenius temperature dependence for the oxidation of ethanol (adapted from [1])

Figure 4 shows the plot of the first-order oxidation of ethanol. The first-rate ethanol oxidation mechanism was obtained to be

$$\frac{-dEtOH}{dt} = 10^{21.82\pm2.7} \exp\frac{(-340 \pm 41)}{RT}[EtOH] \quad (3)$$

Helling et al. provide the kinetic basis for the present two-step model, but its rates were derived from a tubular continuous-flow reactor with pure oxygen, which is a significantly

different setup from the UW SCWO reactor. Hence, applying the mechanism to the NRG reactor with air, coaxial injection, buoyancy effects, heat loss, and complex mixing serves the purpose of investigating the mechanism's applicability and its degree of applicability against experimental data.

Chapter 3. Methodology

3.1. Scope of modeling

This study modeled ethanol oxidation for PFAS destruction process heat generation in the UW SCWO reactor using 2D axisymmetric approach. This study modeled ethanol oxidation with Helling et al.'s two-step mechanism in the UW SCWO reactor using CFD. Ethanol oxidation uses compressed air mixed with supercritical water as the oxidant, which is different from previous work where H_2O_2 was used as the oxidant. The model simulates ethanol oxidation under four different fuel loading cases, which yield the oxidation temperature range of 475 – 650 ℃. Four fuel loadings were tested, where 5 mol% ethanol solutions were supplied at 49%, 56%, 69%, and 100% (nominal) of the total fuel-water mixture flow rate of 10 ml/min. The simulation results of interest are the fuel and wall temperature distribution, CO, O_2, CO_2, ethanol, and H_2O distribution, and oxidation rates.

A chemical reactor approach, using a single perfectly stirred reactor (PSR) modeled ethanol oxidation based on enthalpy equilibrium, was also used to simulate Helling's two-step mechanism under the same operating conditions. The model is a perfect mixing reactor, modeled with heat transfer present, and used the same species composition as in the experiment. The PSR model used an analytical enthalpy balance to estimate the reaction temperatures for all cases. This PSR model was developed to further investigate the degree of validity of the results from the CFD model.

The reactor was modeled as a 2D axisymmetric flow system in ANSYS Fluent 2025R1 CFD package. The boundary of the CFD model included up to the reactor's inner lining and did not incorporate the solid wall heat transfer. Instead, heat transfer was modeled implicitly using isothermal boundary conditions on the inner lining walls, where the values were set to be equal to the measured reactor wall temperatures from the experiments. Since the focus of

the study is to analyze the reaction temperature and chemical kinetics within the reaction zone, the model does not include the quenching flow simulation which happened downstream of the actual reactor to cool down the supercritical mixture.

The models also serve to investigate the degree of validity of the global two-step kinetic formulated by Helling et al. which was derived from 400-500 °C operating conditions to the reactor's operating conditions which is on the range of 475-650 °C.

3.2. Experimental setup, operating conditions, and data

The system has four lines: a fuel line, an oxidant line (consisting of an air line and a water line), a reagent line, and a quenching line. The fuel line continuously feeds the ethanol and water mixture into the reactor through a fuel nozzle/inlet. The water was first mixed with ethanol and then pressurized to 25 MPa by the fuel pump. The pressurized mixture was then heated to 400 °C by a cartridge heater, turning it into a supercritical mixture, and then fed into the reactor through the fuel inlet. The total flow rate of this line was kept constant at 10 ml/min for all cases.

The oxidant line continuously feeds the compressed air and water mixture. The compressed air at 25 MPa was introduced to the air line and then heated to 400 °C by a cartridge heater. Water was introduced to the water line, pumped to 25 MPa, and heated to 400 °C by a cartridge heater. The flow rate of the airline was varied from 5 – 10.6 SLPM, while flow rate of the water line was maintained constant at 10 ml/min. The preheated compressed air was then mixed with supercritical water and entered the reactor through the oxidant nozzle/inlet. The fuel and oxidant inlets are arranged as a coaxial nozzle. The experimental setup is described below.

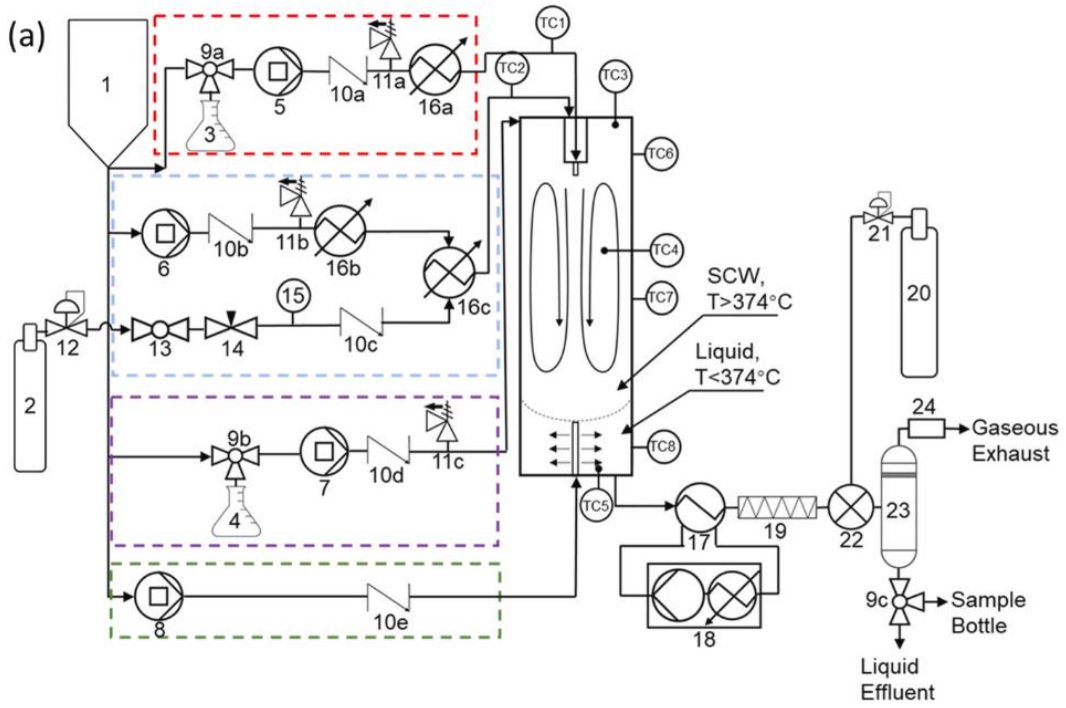

Figure 5. Schematic of the SCWO experiment using ethanol and air. Fuel line (red boundary), oxidant line (blue boundary), reagent line (purple boundary), quenching line (green boundary), reactor body, heat exchangers (17 and 18), a backpressure regulator, and combustion gas monitor. [52]

A set of experimental data from Bai et al. [101] was used as a case study for the CFD and ethanol oxidation modeling. The data were obtained from a set of experiments conducted with the UW SCWO reactor, with ethanol as the pilot fuel. The data from the experiments used as the basis for CFD modeling in this study are for 49%, 56%, 69%, and 100% fuel/water mixture flow rates at varying compressed air flow rates. The air-to-fuel ratio (AFR) was kept constant at 1.2. An analytically pure ethanol from Thermo Scientific was used as fuel, and high-pressure air from Linde Gas at a breathing grade from the air cylinder (6000 psi) was used as the oxidant.

The reagent line feeds the PFAS material into the reactor, and the quenching line feeds the cooling water for the products at the bottom of the reactor. Since the CFD model in this study strictly investigates the ethanol oxidation chemistry in the reaction zones without PFAS destruction, the reagent and quenching lines are not modeled.

The nomenclature of the experiment schematic is indexed as follows:

Table 3. 1. Nomenclature index for SCWO experimental setup

Schematic index	Component
1	Water
2	Air tank
3	Ethanol fuel
4	Reagent (PFAS)
5	Fuel pump
6	Oxidant pump
7	Reagent pump
8	Quenching pump
9a-c	Solenoid valves
10a-e	Check valves,
11a-c	Relief valves
12	Air tank regulator
13	Ball valve
14	Needle valve
15	Rotometer
16a~c	Cartridge heaters
TC1-TC8	Thermocouples
17	Liquid-liquid heat exchanger
18	Liquid-air heat exchanger
19	Particle filter
20	Nitrogen tank
22	Back pressure regulator
23	Gas liquid separator
24	Gas monitor

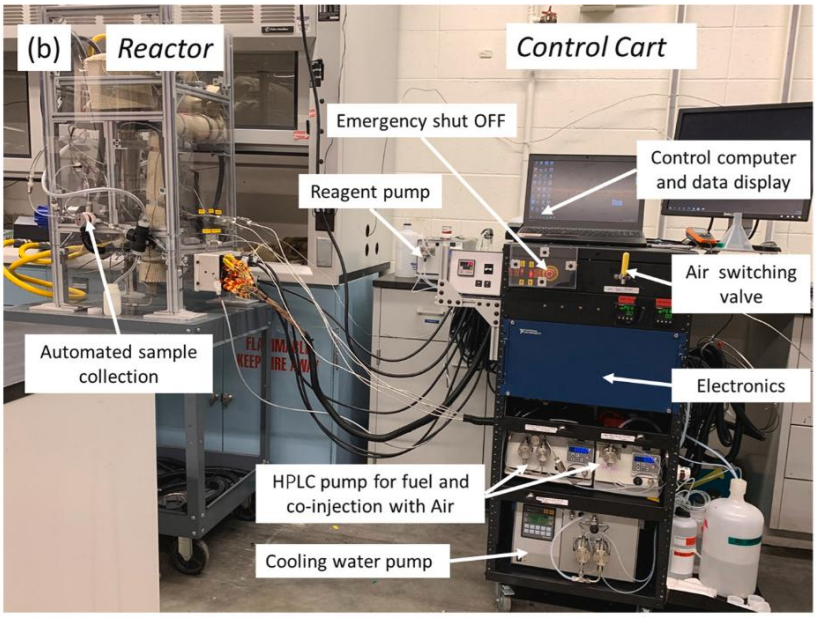

Figure 6. Photograph of the SCWO system configuration [52]

Table 3.2. Flow rate data from the experiment used for the CFD and PSR modeling

Case number	Flow rates				
	Fuel line (fuel-water mixture)			Oxidant line (air-water mixture)	
	Fuel [%]	Water [%]	Total flow rate [ml/min]	Water line [ml/min]	Air line (air) [SLPM]
1	49	51	10	10	5
2	56	44	10	10	6
3	69	31	10	10	7.3
4	100	0	10	10	10.6

Table 3.3. Temperature distribution from the experiment used for the CFD and PSR modeling

Case number	Temperature distribution		
	Reactor wall, top section [°C]	Reactor wall, mid section [°C]	Reactor center [°C]
1	405	410	475
2	420	420	500
3	465	458	550
4	528	525	650

The temperature of the reactor wall top section was measured by a thermocouple probe placed 26 mm from the reactor head, and the thermocouple for the wall mid-section was placed 178 mm from the reactor head. The reaction temperature for each experiment was obtained as the reactor center temperature. The reactor center temperature was measured by a thermocouple inside the reactor, which was placed 178 mm from the reactor head. The wall temperatures shall be used as a boundary condition for the CFD model to simulate heat transfer, and the reactor center temperature shall be used to validate the reaction temperature from the model.

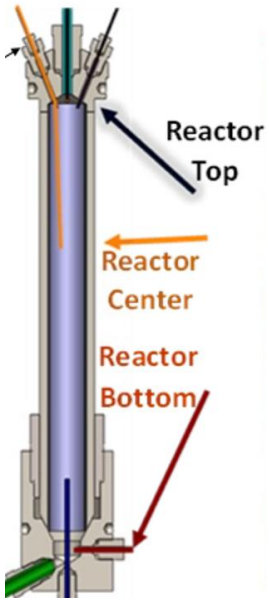

Figure 7. SCWO reactor schematic [102]

Table 3.4. CO concentration from the experiment

CO emission	
Case number	CO concentration, dry basis [ppm]
1	4000
2	400
3	70
4	0

The carbon monoxide (CO) concentration was measured using the combustion gas monitor. After cooling and depressurization, the products enter the separator for gas-liquid separation; the separated gas products first pass through a combustion monitor. The CO emission in Table 3.4 was measured on a dry basis by a desiccator with ~0% humidity.

3.3. CFD Modeling

3.3.1. Summary of CFD Modeling

The summary of the physical, chemical, numerical parameters, and boundary conditions used for the CFD and the PSR models are tabulated in this section. The upcoming sections shall elaborate each of the parameters and conditions used in the CFD model setup.

Table 3. 5. Summary of physical parameters

	Parameter	Model
1	Geometry	2D axisymmetric
2	Fluid	Single phase, supercritical mixture
3	Momentum	Navier-Stokes momentum equation
4	Thermodynamics	Navier-Stokes energy equation
5	Turbulence	RANS, SST k-ω
6	Mixture density	Volume-weighted mixing law, NIST thermophysical properties
7	Mixture specific heat	Mixing law, NIST thermophysical properties
8	Mixture thermal conductivity	Ideal-gas mixing law, NIST thermophysical properties
9	Mixture viscosity	Mass-weighted mixing law, NIST thermophysical properties
10	Mixture mass diffusivity	Kinetic theory, NIST thermophysical properties
11	Mixture thermal diffusion coefficient	Kinetic theory, NIST thermophysical properties

Table 3. 6. Summary of chemical parameters

	Parameter	Model
1	Reaction model	Finite-rate chemistry
2	Integration	ISAT
3	Reaction step 1: Arrhenius preexponential factor	$10^{21.82\pm2.7}$
4	Reaction step 1: Activation energy	-340 ± 41 kJ/mol
5	Reaction step 2: Arrhenius preexponential factor	$10^{7.25\pm0.53}$
6	Reaction step 2: Activation energy	-120 ± 7.7 kJ/mol
7	Thermal diffusion	Active
8	Diffusion energy source	Active

Table 3. 7. Modeled species

	Species
1	C_2H_5OH
2	O_2
3	N_2
4	CO
5	CO_2
6	H_2O

Table 3. 8. Summary of boundary conditions

	Boundary	Parameter	Model
1	Fuel inlet	Mass flow rate	Fuel-water mixture: 10 ml/min (constant)
		Temperature	400 °C
		Species	C_2H_5OH, H_2O
2	Oxidant inlet	Mass flow rate	Airflow: 2-10.6 SLPM (variable) Water: 10 ml/min
3	Wall	Temperature	400 °C
		Species	Air (21% O_2, 79% N_2) , H_2O
		Flux condition	Isothermal
		Temperature	Measured wall temperature
4	Outlet	Outlet model	Pressure outlet

Table 3. 9. Summary of numerical parameters

	Parameter	Model
1	Domain discretization	Structured mesh
2	No. of mesh elements	~200,000
3	Mesh sizing	0.1 mm (inlets and reaction zones), 0.5 mm (downstream)
4	Discretization method	Coupled
5	Discretization scheme	First-order upwind
6	Flow Courant number	<1
7	Solver	Pressure-based solver, transient

3.3.2. Geometry

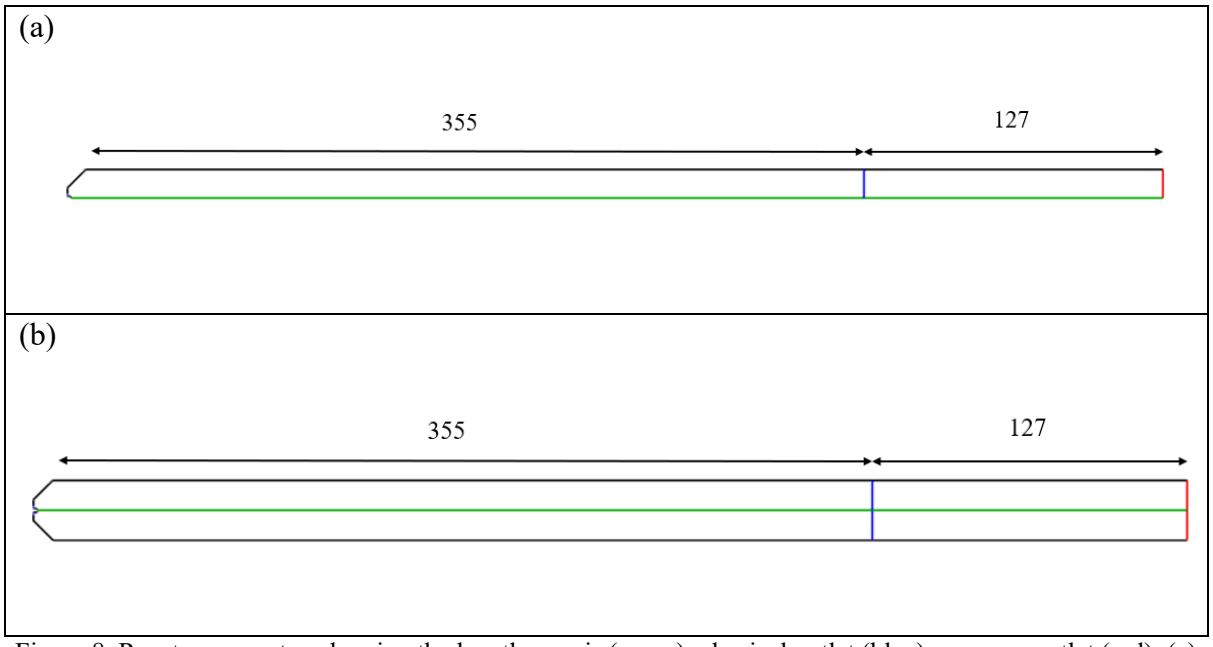

Figure 8. Reactor geometry, showing the length, x-axis (green), physical outlet (blue), pressure outlet (red). (a) the original axisymmetric geometry, (b) the full axisymmetric projected view. Dimensions are in mm.

The reactor was modeled as 2D axisymmetric and followed the dimensions of the actual SCWO reactor, with the length of 355 mm from the reactor head to the outlet. Figure 9 (a) shows the close-up of the reactor head and the hydraulic diameter of the reactor, and (b) shows the close-up on the coaxial nozzle and its dimensions. The coaxial nozzle has the arrangement so that the fuel inlet is enveloped by the oxidant inlet.

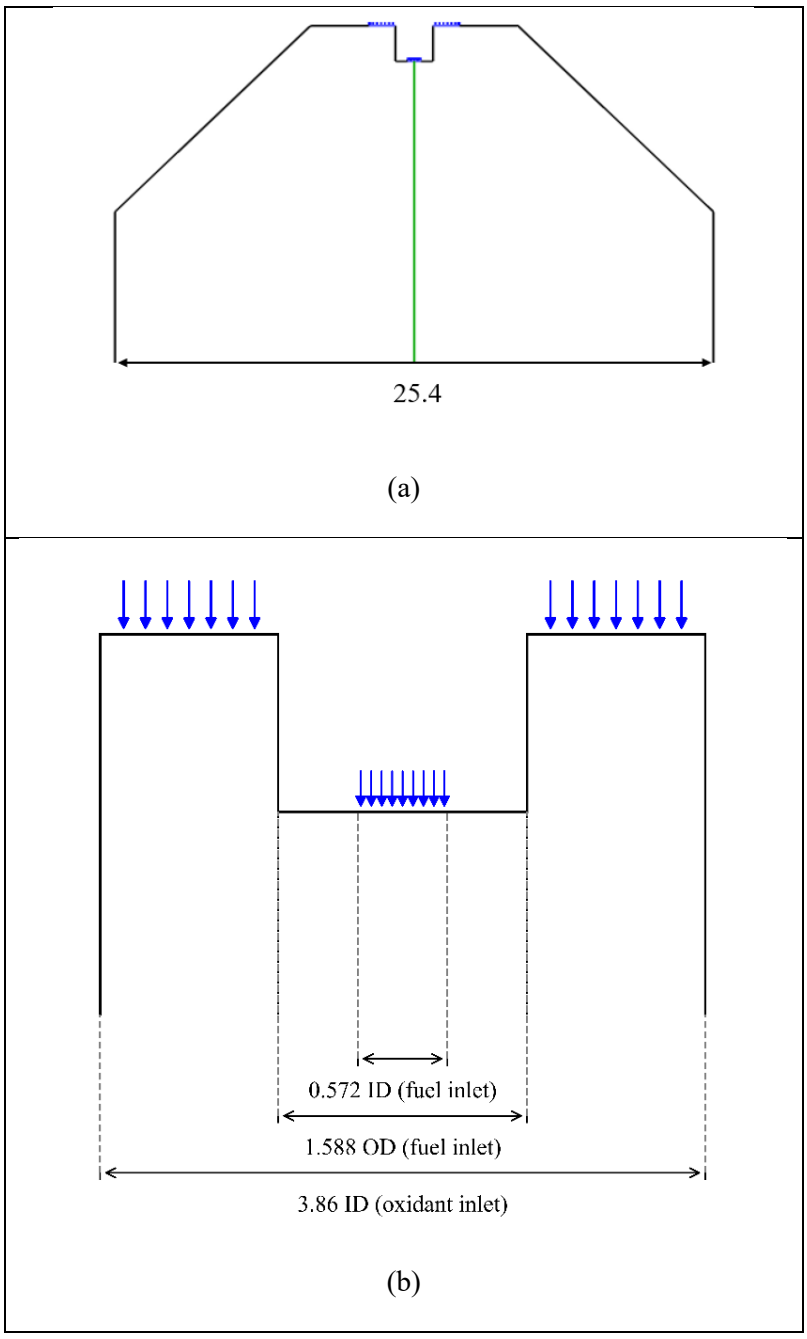

Figure 9. Reactor head dimension close-up, showing the sizing of the coaxial nozzle. Dimensions are in mm.

In the 2D-axisymmetric model, the fluid flow follows a tubular domain as if the modeled domain is rotated along the x-axis (green line) to become the full tubular reactor. Therefore, it implicitly models a 3D tubular reactor flow instead of explicitly modeling the fluid flow in a 3D domain, which significantly reduces computational overhead while still providing an adequate model of the continuous flow reactor [33] [83].

The actual converging nozzle at the bottom of the reactor was not modeled in the CFD to maintain good convergence at the pressure outlet. Due to dominant reversed flows in the lower-temperature simulations that hinder convergence, the model's pressure outlet (red) was extended further downstream by 5x the reactor's hydraulic diameter (127 mm). The model's physical outlet (blue) lies at 355 mm from the reactor head, the same as the original reactor. The species values to be validated against the experimental results shall be obtained from the physical outlet.

3.3.3. Mesh generation

The domain was discretized/meshed into structured quadrilateral elements. The mesh size at the reactor head and the reaction zones is ~0.1 mm, with variations of the size given by inflation as the domain reaches the centerline axis and the shear layers where the species were expected to mix during the reacting flow. The smallest elements at the expected shear layer and the center of the inlets are 0.015 mm, with gradually increasing size as they further go laterally.

The fine mesh structure of ~0.1 mm goes from the reactor head to approximately 45% of the reactor length (~160 mm) to well define the fluid dynamics in the reaction zone. As the domain goes further downstream from ~160 mm, the mesh gradually grows in size to become 0.25 mm. The downstream elements are structured in a rectangular manner and uniform.

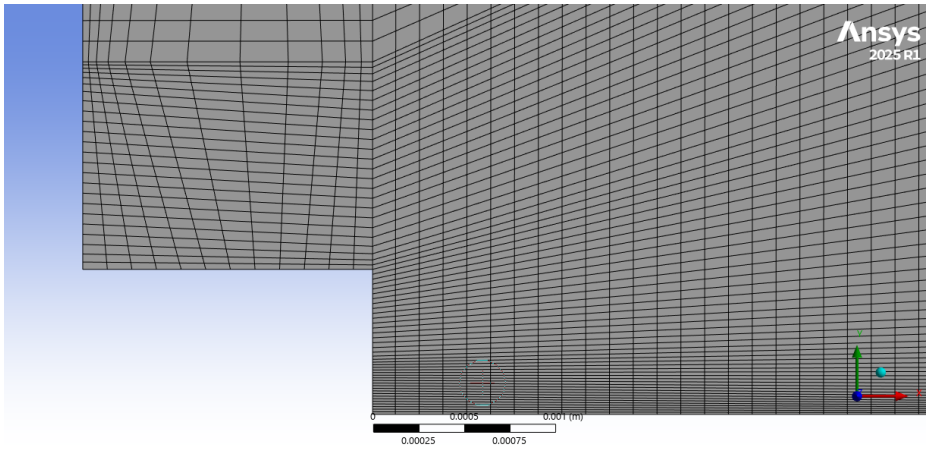

Figure 10. Mesh sizing at the inlets and the reactor head, showing finer mesh size at the expected reaction layer.

The analysis on the orthogonal quality shows that the mesh has excellent quality of ~99% in 97.2% of the domain, where the worst quality of the elements slightly occurs in the transition between the reaction and the downstream zones.

The wall boundary in the reaction zones and the downstream are also structurally meshed. This width corresponds to the wall y+ below 1.0. The calculation of the wall y+ target is given by the equation,

$$\Delta s = \frac{y^{+}\mu}{\sqrt{\frac{\left(\frac{0.026}{Re_x^{\frac{1}{7}}}\right)\rho U_\infty^2}{2\rho}}\,\rho} \tag{4}$$

The uniform width of the elements at the wall boundary was modeled to be 0.10 mm, which provides the y+ value in the range of 0.65 < y+ < 1. This ensured that the elements at the wall boundary have been properly sized to simulate boundary layer dynamics and convective heat transfer. At the downstream beyond the expected reaction zone, the fluid elements are uniformly structured as quadrilaterals of 0.25 mm. The statistics of the mesh are summarized in the table below.

3.3.4. Mesh refinement

A mesh refinement was conducted to determine the choice of mesh sizing to be used in the study. Coarser mesh resolutions were difficult to achieve convergence. The independence study was carried out on three different mesh modeling:

(1) a model with fine mesh (0.1 mm) that extends to 40 mm (fine 40 mm reaction zone),

(2) a model with fine mesh (0.1 mm) that extends to 90 mm (fine 90 mm reaction zone),

(3) a model with fine mesh (0.1 mm) that extends to 160 mm (fine 160 mm reaction zone).

All three models have the same maximum element size of 0.25 mm. The difference between the models lies in the length of the fine reaction zone, where the mesh was modeled to be fine and have the maximum size of 0.1 mm.

The temperature and CO distribution were observed between the three different meshing models for the baseline case of reaction temperature = 475 °C. The CO species contours were also observed for the three cases. It was observed that the CO distribution was the most sensitive parameter with respect to mesh refinement.

Table 3.10. Model results - mesh sensitivity study

Case	Mass weighted reaction temperature (°C)	Mass averaged CO mol fraction, outlet
(1)	469.7	0.00373
(2)	469.4	0.00053
(3)	471.6	0.00050

The reaction zone temperature between the three models only varies slightly within the range of ~3% differences. The CO mol fraction at the physical outlet has the highest variance, with an order of magnitude difference between the coarsest mesh and the finer mesh models. The % difference became significantly lower by using finer mesh (cases 2 and 3) and became

more agreeable with the CO mol fraction obtained from the experiment. This suggests that although the reaction temperatures only vary slightly with mesh resolution, the CO distribution is very sensitive to the mesh resolution in the reaction zone.

The coarser meshes (case 1 and 2) seemed to struggle with unsteady CO recirculation into the reaction zone. The finest mesh resolution (case 3) gave the best gradual distribution of CO from the reaction zone to the outlet and was able to resolve the unsteady recirculation.

The finest mesh settings were able to adequately model the thermodynamics and CO distribution that reasonably agreed with the experimental value (within a 28.42% difference) and achieved better convergence. Distributing a coarser mesh downstream from ~160 mm gave the benefit of lightening the computational demand, while the model was able to model the reaction zone properly. For this reason, the fine mesh model was selected as the mesh model to be used in this study.

Table 3.11. Mesh statistics

	Mesh parameters	**Model**
1	Element type	Structured quadrilateral
2	Maximum element size, upstream reaction zone	0.1 mm
3	Minimum element size, upstream reaction zone	0.015 mm
4	Uniform element size, downstream	0.25 mm
5	Orthogonal quality	~99% on 97.2% of the domain
6	Number of elements	207805

3.3.5. Governing equations

The CFD model solves the conservation of mass, momentum, energy and species transport. The detailed derivation of the governing equations is given in the Appendix. The momentum conservation for a 2D axisymmetric fluid flow in the axial and radial directions, respectively are defined [103] as:

$$\frac{\partial}{\partial t}(\rho u_x) + \frac{\partial}{\partial x}(r\rho u_x u_x) + \frac{1}{r}(r\rho u_r u_x) = -\frac{\partial p}{\partial x} + \frac{1}{r}\frac{\partial}{\partial x}\left[r\mu\left(2\frac{\partial u_x}{\partial x} - \frac{2}{3}\nabla\cdot\vec{u}\right)\right]$$

$$+\frac{1}{r}\frac{\partial}{\partial r}\left[r\mu\left(\frac{\partial u_x}{\partial r} + \frac{\partial u_r}{\partial x}\right)\right] + F_x \qquad (5)$$

(x-momentum)

And

$$\frac{\partial}{\partial t}(\rho u_r) + \frac{1}{r}\frac{\partial}{\partial x}(r\rho u_x u_r) + \frac{1}{r}\frac{\partial}{\partial r}\,(r\rho u_r u_r) = -\frac{\partial p}{\partial r} + \frac{1}{r}\frac{\partial}{\partial x}\left[r\mu\left(\frac{\partial u_r}{\partial x} + \frac{\partial u_x}{\partial x}\right)\right]$$

$$+\frac{1}{r}\frac{\partial}{\partial r}\left[r\mu\left(2\frac{\partial u_r}{\partial r} - \frac{2}{3}(\nabla\cdot\vec{u})\right)\right] - 2\mu\frac{u_r}{r^2} + \frac{2}{3}\frac{\mu}{r}(\nabla\cdot\vec{u}) + \rho\frac{u_z^2}{r}\,F_r \qquad (6)$$

(radial momentum),

Where

$$\nabla\cdot\vec{u} = \frac{\partial u_x}{\partial x} + \frac{\partial u_r}{\partial r} + \frac{u_r}{r} \qquad (7)$$

The momentum equation has multiple elements. The $\frac{\partial}{\partial t}$ term – the transient term, represents the rate of change of the momentum with respect to time.

The general form of the energy equation used in this model was derived from the NS equation and given by

$$\frac{\partial}{\partial t}(\rho E) + \nabla\cdot\left(\vec{u}(\rho E + p)\right) = \nabla\cdot\left(k_{eff}\nabla T\right) + S_h \qquad (8)$$

Similarly, the species transport equation follows the general scalar transport equation and follows the general form:

$$\frac{\partial}{\partial t}(\rho Y_i) + \nabla \cdot (\rho u Y_i) = -\nabla \cdot J_i + R_i + S_i \quad (9)$$

3.3.6. Turbulence model

Taking the mass-averaged density, bulk characteristic velocity, and viscosity from the lowest flow rate case, the average Reynolds number was obtained to be

$$Re_{average} = 1.17 \cdot 10^4 \quad (10)$$

Therefore, the flow in the reactor is determined to be turbulent. The preliminary simulation of the model also showed dominant recirculation in the reaction zone (as shown in the figure), signifying the need for turbulence modeling.

The study done by Purohit [33] concluded that the use of the SST model for the buoyancy-dominated SCWO reactor was able to well-define the recirculation (the Richardson number ranges from 4.11 – 23.90), for the convection heat transfer in the walls, and the layers between the different substances. The model also achieved good agreement with experiments.

The SST $k - \omega$ model can properly account for the transport of turbulent shear stress, especially in the mixing region [56], [104]. The model also incorporates a damped cross-diffusion derivative term to ensure that the model equations are relatively more stable in both the near-wall and far-field zones [103] [104].

3.3.7. Chemical reaction modeling

The first step of the mechanism is given by

$$C_2H_5OH + 2O_2 \rightarrow 2CO + 3H_2O \tag{11}$$

The ethanol dissociation into CO was modeled by Helling et al. [2] to be

$$\frac{-dC_2H_5OH}{dt} = 10^{21.82\pm2.7} \exp\frac{(-340 \pm 41)}{RT}[C_2H_5OH] \tag{12}$$

The first term of the mechanism shall be the Arrhenius preexponential factor, and the second term, which was divided by the gas constant and the temperature, shall be the activation energy. For ethanol dissociation, Helling et al. used 1.0 as the ethanol reaction order.

The second step is the CO oxidation into CO_2, which is given by

$$2CO + O_2 \rightarrow 2CO_2 \tag{13}$$

Similarly, the CO oxidation mechanism was modeled by Helling et al. [2] to be

$$\frac{-dCO}{dt} = 10^{7.25\pm0.53} \exp\frac{(-120 \pm 7.7)}{RT}[CO]^{1.014\pm0.09}[O_2]^{0.03\pm0.04} \tag{14}$$

The reaction order depends on the concentration of CO and O_2. This study investigates the validity of the mechanism in terms of their pre-exponential factors and activation energies within their respective uncertainty bounds, while keeping the reaction order unchanged from their baseline values.

This study uses a finite-rate model to describe the mechanism. The previous modeling of the SCWO reactor [33] and the initial simulation suggest that the mixing time is shorter than the kinetic time scale, making the reaction controlled by the chemical kinetics. In the finite rate model, reaction rates are determined by Arrhenius kinetic expressions and ignore the effects of turbulent fluctuations. The Damköhler number is used to estimate the reaction characteristics,

$$Da = \frac{\tau_{mixing}}{\tau_{kinetic}} \tag{15}$$

It was obtained from the initial simulation of the 49% injection case, to be in the range of $6.27 - 8.10 \times 10^{-3}$. The Da value from all the injection rate cases is also given in Table 4.1, which is shown to remain <1 across the majority of cases. This adds the justification for using the finite-rate chemistry model.

The previous modeling also showed that the finite-rate vs. eddy-dissipation concept models gave less than a 3% difference in the reaction temperature. Outside of the relatively small region near the fuel jet, the simulations do not show significant differences [1]. This finding suggests that mixing is only important in the relatively small region of the SCWO reactor, and heat release is controlled by kinetic rates. Hence, the finite rate model was considered appropriate for this model.

ISAT integration was also used to preserve stability during the reaction while allowing a faster chemistry integration than direct source integration. Thermal diffusion was also activated to model heat transfer between the reacting species. The summary of the reaction modeling is given in the table below.

Table 3. 12. Reaction modeling

Reaction parameters	Model
Volumetric Reaction	Finite rate
Rate 1 : Preexponential Factor	$10^{21.82\pm2.7}$
Rate 1: Activation Energy	340 ± 41 kJ/mol
Rate 2: Preexponential Factor	$10^{7.25\pm0.53}$
Rate 2: Activation Energy	120 ± 7.7 kJ/mol
$[C_2H_5OH]$ reaction order	1.0
$[O_2]$ reaction order	0.03
$[CO]$ reaction order	1.014

3.3.8. Species thermophysical properties

The thermophysical properties of C_2H_5OH, O_2, CO, CO_2, N_2, and H_2O referred to the NIST database [105]. The properties data were obtained for the range of temperature of 300-1100 ºC at 24.6 MPa. The thermophysical properties data for each species were modeled using temperature-dependent polynomials, given by

$$\emptyset = a + b \cdot T + c \cdot T^2 + d \cdot T^3 + \cdots \quad (16)$$

The polynomial coefficients (a, b, c, d…) and the detailed thermophysical properties for each species shall be given in the Appendix. This section shall elaborate on the thermophysical properties of scH_2O.

The thermophysical properties of scH_2O become discontinuous as water approaches ~394 °C. At the supercritical point, the molecular behavior of water changes significantly because of the phase change. The density, viscosity, and thermal conductivity change at a much slower rate as temperature increases. The specific heat of water at this pressure increases sharply as water goes from 100 < T < ~394 °C, where it is in the vapor phase. Beyond that point, the specific heat decreases sharply and then reaches an almost asymptotic value. Due to the nonlinearity, the thermophysical properties of scH_2O were modeled as polynomials in the CFD model to capture the sharp changes in the properties with respect to temperature.

The thermophysical properties of CO at 25 MPa for the temperature range of 100-220 °C are given in the Appendix. The available property data from NIST only covers this temperature range at 25 MPa. Due to the near-linearity, the thermophysical properties of CO above 220 °C were extrapolated. The density of supercritical CO was extrapolated using a second-order polynomial fit to get its estimate in the temperature range of 200<T<800 °C. From the polynomial fit, it was estimated that the density dependence on temperature was given by

$$\rho(T) = 6.57 * 10^2 - 1.82 * T + 1.62 * 10^{-3} * T^2 \quad (17)$$

In this model, the specific heat of CO was assumed to have a negligible gradient for temperatures above 220 °C and therefore was modeled to be

$$Cp(T)_{scCO} = 1043 \frac{J}{kg * K} \quad (18)$$

This assumption was considered acceptable due to the monotonically decreasing gradient of CO's Cp above 220°C and the very low percentage of CO as an intermediate species within the overall mixture, which was dominated by supercritical water.

The thermal conductivity and viscosity of CO and C_2H_5OH were modeled as functions of the Lennard-Jones kinetic theory of gas [58] [106]. The kinetic theory definition shall be described in the Appendix. All the thermophysical properties were modeled into a single-phase supercritical mixture.

3.3.9. Boundary conditions

The fuel and oxidant flow rates and the wall temperature measurements from the experiment setup were converted into the appropriate boundary conditions for the CFD model. The fuel and oxidant flow rates were calculated using mass-weighted averaging and mol fractioning. The derivation for the flow rates is given in detail in the Appendix.

Table 3. 13. Inlet boundary conditions

Ethanol flow rate	Total flow rate, fuel inlet (kg/s)	Flow rate, oxidant inlet (kg/s)	Inlet temperature (°C)
49%	0.000162127	0.000266226	400
56%	0.000162127	0.000285871	400
69%	0.000162127	0.000311409	400
100%	0.000162127	0.000376238	400

Table 3. 14. Inlet boundary conditions - mass fractions

Ethanol flow rate	Species mass fractions, fuel inlet		Species mass fractions, oxidant inlet		
	C_2H_5OH	H_2O	O_2	N_2	H_2O
49%	0.060348171	0.939651829	0.085896075	0.283060091	0.631043833
56%	0.069609155	0.931390845	0.095991928	0.316329747	0.587678325
69%	0.083724265	0.916275735	0.107212228	0.353304886	0.539482886
100%	0.11862241	0.88137759	0.128853451	0.42462091	0.446525639

Table 3. 15. Wall temperature boundary conditions

Ethanol flow rate	Model reactor wall temperature (°C)
49%	407.5
56%	420
69%	461.5
100%	526.5

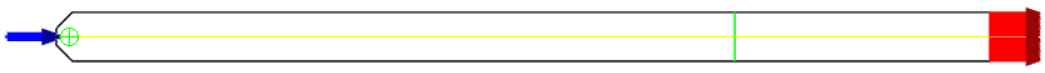

Figure 11. Schematic of the model showing the boundary conditions. Inlets (blue), pressure outlet (red), physical outlet (green), walls (black)

The wall temperatures from the experiment were modeled as isothermal wall temperature boundary conditions. The measurements from the reactor top wall and mid wall temperatures were averaged and used as the input for the wall boundary conditions in the CFD model to implicitly model the convective heat transfer from the reactor to the outside surface.

The outlet of the model was modeled to be a pressure outlet with a backflow temperature of 400 °C and zero backflow mass fractions. Due to recirculation occurring in the test simulations for the low-temperature cases, the pressure outlet was extended by 5x the reactor diameter (125 mm) to ensure the reacting flow was not disturbed by recirculation. ion. In this model, the physical outlet remained at 355 mm from the reactor inlet, which is the original position of the reactor's outlet. The CFL number was targeted to be equal to 1 and was calculated from

$$CFL = u\frac{\Delta t}{\Delta x} \tag{19}$$

Where the time-steps for each of the case were adjusted depending on the velocity of the jet.

3.4. Chemical Reactor Approach

A chemical reactor network is a computationally lean approach for modeling reacting flow. It is a reduced-order zonal model representing fluid dynamic interactions without the significant overhead of solving the flow field. [83, 91, 107-110]. The analysis of local Reynolds and Damkohler numbers [111] from CFD can be used to inform the type of reactor elements and their linkages in the CRN network. This approach can streamline the screening of promising reaction mechanisms and utilize the developed CRNs to optimize SCWO reactor operations. A commercial package, ANSYS Chemkin-Pro, can be used. Here, a zero-dimensional perfectly mixed reactor model was developed to provide a reduced-order

comparison for the reaction temperatures and product compositions predicted by the CFD model. This model was created based on the reaction temperature and the CO product concentration data from the experiment.

The initial concentrations for the reactants were still based on the experimental setup but were modeled as if the species entered through one inlet and underwent mixing. The mol and mass fractions of the reacting species were first converted to molar concentrations using the mixture density and species molecular weight. The initial mol fractions were given on the table below.

Table 3. 16. Mole fractions of the reactants for the PSR model (mol/mol)

Ethanol flow rate	C_2H_5OH	O_2	N_2	H_2O
49%	0.009925811	0.033398056	0.125640305	0.83103583
56%	0.010959144	0.038921999	0.146420852	0.80369801
69%	0.012903851	0.045691999	0.17188895	0.769515
100%	0.016773163	0.060870012	0.228987189	0.69336964

The enthalpy balance of the reaction was given by

$$\sum n\left(h_o + \Delta h_{25^oC-T_{adiabatic}}\right)_{products} = \sum n(h_o + \Delta h_{25^oC-400^oC})_{reactants} \quad (20)$$

The reference enthalpy value (h_o) for scH$_2$O in the subcritical region was determined to start from the liquid phase, which is at -241.8 kJ/mol. The enthalpy values were determined based on the NIST database [105]. The reaction steps were modeled according to the mechanism by Helling et al [2]. Rewriting the equations,

$$r_1 = A_1 \exp\left(-\frac{E_{a1}}{RT}\right)[C_2H_5OH]^{n1}[O_2]^{m1} \quad (21)$$

$$r_2 = A_2 \exp\left(-\frac{E_{a2}}{RT}\right)[CO]^{n2}[O_2]^{m2} \quad (22)$$

Where A, Ea, m, and n are the Arrhenius preexponential factors, activation energies, and reaction orders, respectively. The molar reaction rates (r1, r2) were then converted to mass-fraction rates. The general $\frac{dY}{dt}$ equation for each species was modeled as

$$\frac{dY}{dt} = f(r1, r2) \tag{23}$$

Where Y is the mass fraction of each species. The detailed equations for each species are given in the Appendix. To model the heat transfer coming from the reactor as in the experiment, the $\frac{dT}{dt}$ equation was modified to include a constant heat transfer factor (htf).

$$\frac{dT}{dt} = -\frac{htf}{c_{p,mixture}} \sum_i h_i \frac{d[M]_i}{dt} \tag{24}$$

The regression of the temperature trend obtained the value of htf to be

$$htf = 0.3345 \cdot \frac{x_i}{0.01677} + 0.3999 \tag{25}$$

Where x_i is the mole fraction of each reacting species. Once the heat transfer coefficient htf was applied to the dT/dt function, the reaction temperatures from the PSR model matched very well with the experimental data with <5% difference.

For each time step, the reaction temperature was obtained, and the temperature was used to determine the enthalpy (h). The temperature was then used to determine the reaction rates and, in turn, the species concentrations at the next time step, which are then used to

determine the temperature at the next time step. The process repeats until the final reaction temperature and enthalpy were obtained at a given residence time (τ_{res}). This time step iteration process was solved numerically using the Radau solver. As an assumption, the t = τ_{res} approximation was used to represent this PSR model.

Chapter 4. Results and Discussion

4.1. Non-dimensional parameters

In this study, various non-dimensional parameters are described to characterize the ethanol oxidation process within the reactor.

4.1.1. Equivalence ratio

The oxidant—fuel equivalence ratio ϕ_{AF} for this model is defined by the ethanol and air flow fractions divided by the mass-based stoichiometric air-to-fuel ratio.

$$\phi_{AF} = \frac{\dot{m}_{air}/9}{\dot{m}_{ethanol}} \tag{26}$$

For all of the cases, a combination of ethanol injection and air rates at the boundary condition was maintained to give a value of ϕ_{AF} to be

$$\phi_{AF} = 1.2 \tag{27}$$

The value of ϕ_{AF} characterizes the reaction to be fuel-lean. A fuel-lean condition indicates that excess air is supplied more than the stoichiometric requirement. This ensures that a more complete oxidation of fuel is achieved and excess O_2 is present for all of the ethanol injection rate cases studied. Excess oxidant availability drives further oxidation of CO toward CO2.

4.1.2. Reynolds number

The Reynolds number in the reaction zone was defined using the fuel nozzle diameter and the mean fuel velocity at the fuel nozzle exit to characterize the injection.

$$Re = \frac{\rho V D_{fuel}}{\mu} \tag{28}$$

The density and viscosity vary slightly across the four injection cases due to small differences in local fluid conditions at the nozzle; however, since the total fuel flow rate is held constant across all cases, the resulting Reynolds numbers are nearly identical.

Table 4. 1. Reynolds number of the CFD model, measured at the fuel inlet

Ethanol flow rate (%)	Re
49	14456
56	14403
69	14305
100	14080

The computed Reynolds numbers (14,080–14,456) fall well above the threshold for turbulent pipe/jet flow, indicating that the fuel injection is turbulent for all four operating conditions. This is consistent with the injection Reynolds numbers reported by Purohit et al. [33] for the same reactor geometry (5,415–17,542), supporting the validity of the injection characterization approach used in this study. Turbulent injection promotes rapid mixing between the fuel and oxidant streams near the nozzle.

4.1.3. Damköhler number

The Damköhler number (Da) describes the time scale characteristics of the reaction. It is given as

$$Da = \frac{\tau_{mixing}}{\tau_{kinetic}} \tag{29}$$

The time scales were obtained at the highest oxidation peak location for all the cases with respect to each of the reaction rates, consistent with the approach used by Purohit et al. [33]

Table 4. 2. Damköhler number of the CFD model

Ethanol flow rate (%)	Da_{r1}	Da_{r2}
49	8.10×10^{-3}	6.27×10^{-3}
56	2.57×10^{-2}	1.95×10^{-3}
69	1.88×10^{-2}	5.37×10^{-4}
100	1.04×10^{1}	6.75×10^{-3}

The Damköhler numbers for both reactions were below unity for the majority of operating conditions (49%, 56%, and 69% ethanol injection rates), indicating that mixing occurs faster than chemical reaction at these conditions. This supports the use of the finite-rate chemistry model, as the reaction rate is expected to be governed primarily by the reaction kinetics rather than turbulent mixing.

At the 100% ethanol injection case, Da_{r1} increased to approximately 10.4, suggesting that ethanol oxidation approaches a mixing-influenced regime at this condition. This indicates that the eddy-dissipation concept (EDC) model may provide a more physically appropriate representation of the turbulence-chemistry interaction for this specific case. However, Purohit et al. [33] found that the finite-rate and EDC models predicted similar temperatures outside of the region immediately near the fuel injector, with differences only appearing in the primary reaction zone. Given this, the finite-rate model used in this study is still assumed to provide a

reasonable temperature prediction for the 100% case, despite the shift toward a more mixing-influenced regime for the primary oxidation reaction.

4.1.4. Turbulent Reynolds number

The oxidation regime shall be characterized by the turbulent Reynolds number, Re_t at the peak oxidation locations for both rates. Re_t is given as

$$Re_t = \frac{\rho k}{\mu \omega} \tag{30}$$

This definition of Re_t was obtained from Wilcox et al.'s turbulent model [112] and consistent with the general Damköhler–Reynolds regime characterization approach used by Purohit et al. [33]. For all ethanol injection rate cases, Re_t was obtained from the CFD to be

Table 4. 3. Turbulence Reynolds number of the CFD model

Ethanol flow rate (%)	Ret,r1	Ret,r2
49%	194.09	428.29
56%	159.06	178.28
69%	115.82	111.74
100%	75.81	76.11

4.1.5. Oxidation regime

The oxidation regime shall be determined by the combination of Re_t and the Klimov-Williams-based Karlovitz number, Ka, which is consistent with the approach used by Purohit et al. [33] and shall be calculated for both reaction steps at their respective peak oxidation points.

$$Ka = \frac{\sqrt{Re_t}}{Da} \tag{31}$$

Table 4. 4. Oxidation regime, reaction 1, CFD model

Ethanol flow rate (%)	Da_{r1}	Ka_{r1}	Regime
49	8.10×10^{-3}	1719.95	Distributed
56	2.57×10^{-2}	490.74	Distributed
69	1.88×10^{-2}	572.45	Distributed
100	1.04×10^{1}	0.84	Flamelet-like

Table 4. 5. Oxidation regime, reaction 2, CFD model

Ethanol flow rate (%)	Da_{r2}	Ka_{r2}	Regime
49	6.27×10^{-3}	3300.70	Distributed
56	1.95×10^{-3}	6847.30	Distributed
69	5.37×10^{-4}	19684.80	Distributed
100	6.75×10^{-3}	1292.50	Distributed

The fuel and oxidant streams are injected separately through a coaxial nozzle, resulting in a non-premixed combustion configuration. As shown in Table 4.4 and Table 4.5, the calculated Karlovitz numbers indicate that the reactor operates predominantly in a distributed reaction regime (Ka >> 1) across both reactions and nearly all operating conditions, consistent with the distributed regime reported by Purohit et al. [33] for the same reactor geometry. The only exception is Reaction 1 (ethanol oxidation) at the 100% duty cycle case, where Ka_{r1} falls to 0.84 — just below the Klimov-Williams threshold of unity. This indicates that at this specific condition, the primary ethanol oxidation reaction approaches a flamelet-like regime, where turbulent mixing timescales become comparable to the chemical reaction timescale rather than remaining fast relative to it.

This result supports the use of the finite-rate chemistry model throughout the majority of this study, as the reaction remains kinetically controlled — and therefore insensitive to turbulence-chemistry interaction effects. For the 100% ethanol flow rate case specifically, the borderline Ka_{r1} value suggests that an EDC-based approach may provide a more physically accurate representation of ethanol oxidation at this condition. However, as discussed in Section 4.1.3, the finite-rate model used in this study remains a reasonable approximation for the reactor as a whole.

4.2. Helling's two-step mechanism rate optimization

The 49% (of nominal 100%) ethanol flow rate case serves as the calibration case for the rate parameters, and the 56%/69%/100% ethanol flow rate cases are then evaluated predictively using the resulting optimized kinetic parameters. The two-step mechanism of ethanol oxidation published by Helling et al. [1] includes uncertainty bounds to account for different types of systems and measurement uncertainties. The baseline values of the kinetic parameters (activation energy and pre-exponential factors) are not guaranteed to predict the same temperature and chemical product formation in the SCWO reactor. This is because Helling et al. conducted the experiment on a sand bath reactor under different flow rates and a range of temperatures. For this specific reason, Helling's two-step mechanism shall be optimized for ethanol oxidation in the SCWO reactor. Additionally, the degree of its validity across all the SCWO reactor cases shall be investigated in this study.

In this study, the exact kinetic parameters are tuned within Helling's uncertainty bounds for use in the SCWO reactor modeling. The values were to be obtained through an iteration process between the CFD model and the PSR model.

A reaction simulation using the baseline kinetic values was conducted in the PSR model, with the effects of heat transfer released from the reactor. In the initial PSR model, the baseline values of A1, A2, E_{a1}, and E_{a2} were used for the 49% ethanol flow rate case. The reaction residence time was set to $\tau_{res} = \sim 45\ s$, which was the estimated residence time from Bai et al.'s experiment [101]. Where A1 and A2 denote the Arrhenius preexponential factor for step-1 and step-2, respectively. And Ea_1 and Ea_2 denote the activation energy for step-1 and step-2, respectively, in kJ/mol.

Table 4. 6. Initial conditions for PSR model

Initial conditions, PSR model	Values
A1	$10^{21.82}$
Ea1	340 kJ/mol
A2	$10^{7.25}$
Ea2	120 kJ/mol
τ_{res}	45 s

It was observed that the reaction did not ignite using the initial baseline values of the kinetic parameters. From studying the Helling's rate in the PSR simulation, it was found that Ea_1 had a significant effect on the ignition. Afterward, a set of simulations was run to investigate the effects of Ea_1 on the ignition and to determine the appropriate value for the reaction. The simulations were carried out by changing the values of Ea_1 within the uncertainty bounds given by Helling et al. [1], which is within $\pm 41\ kJ/mol$. The rest of the kinetic parameters such as $A1, A2, Ea_2, m, n$, and t_{res} were kept constant.

Figures 12 and 13 show the dependence of CO and reaction temperature with Ea_1. It can be observed from the concentration of CO and ethanol and the temperature that the ignition started to happen in the range of $Ea_1 = 310 - 320\ kJ/mol$, which is in the lower uncertainty bound of Helling's mechanism. At the upper bounds of the Ea_1, the reaction did not start. This implies that the reaction needs lower activation energy to start the ethanol oxidation because of the heat loss from the reactor.

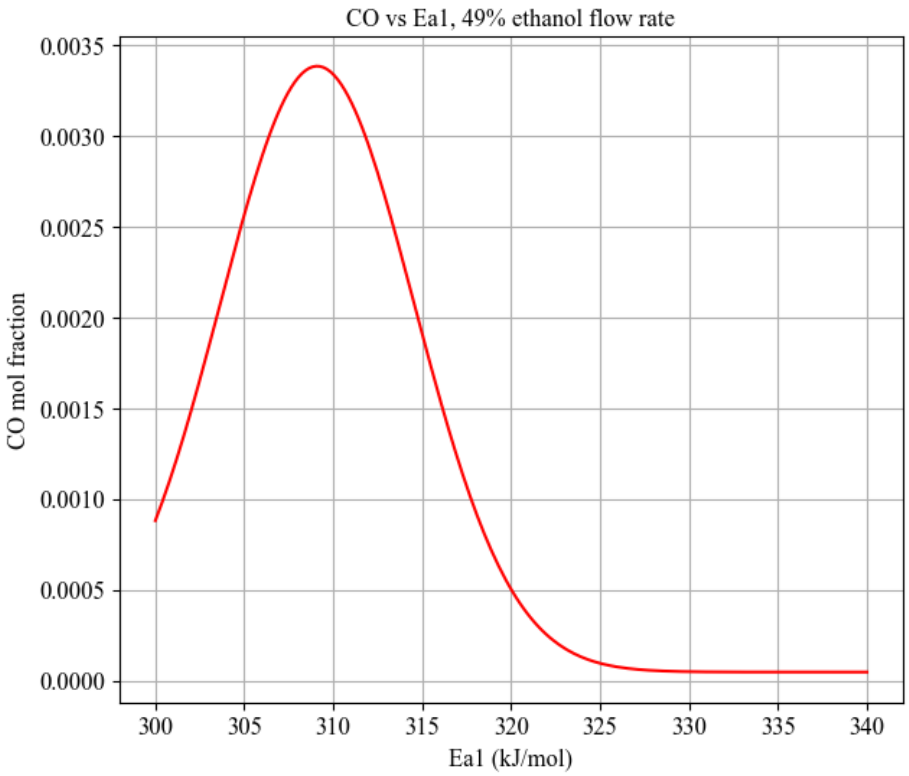

Figure 12. CO mol fraction with respect to Ea1

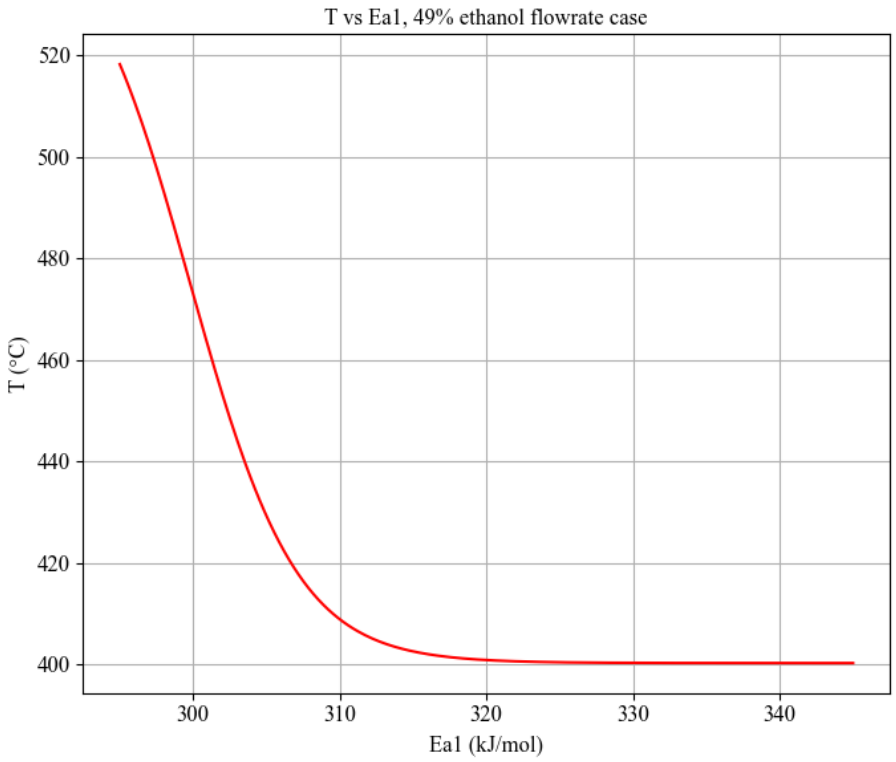

Figure 13. Reaction temperature with respect to Ea1

Lowering the Ea_1 further from ~320 kJ/mol has the effect of providing a more complete ethanol oxidation. The minimum bound $Ea_1 = 299\ kJ/mol$ gave the closest CO mol fraction and reaction temperature agreement with experiment with all the other baseline parameters.

Figures 14 and 15 show the CO mol fraction (in PPM) and reaction temperature for all the cases using $Ea_1 = 299\ kJ/mol$ and the other baseline kinetic parameters in the PSR model with $t_{res} = 45\ s$.

The reaction temperature matches closely with the experiment for each ethanol flow rate case. However, the CO concentration for the PSR model using these rate parameters were overpredicted by an order of magnitude.

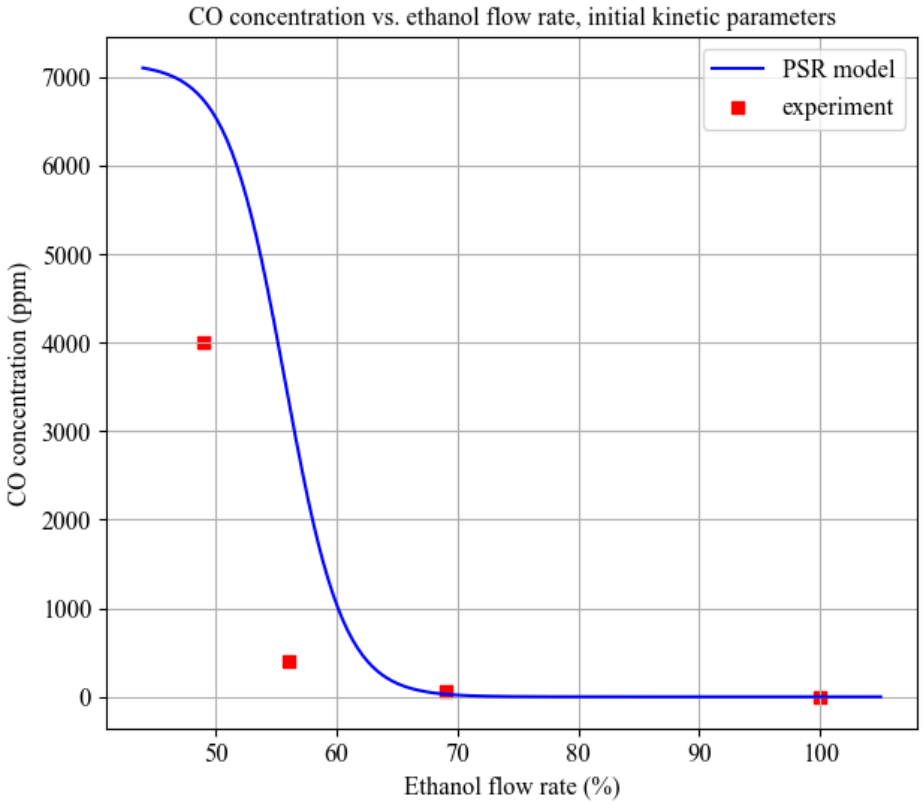

Figure 14. CO concentration, PSR model vs. experiment, Ea1 = 299 kJ/mol, baseline kinetic parameters

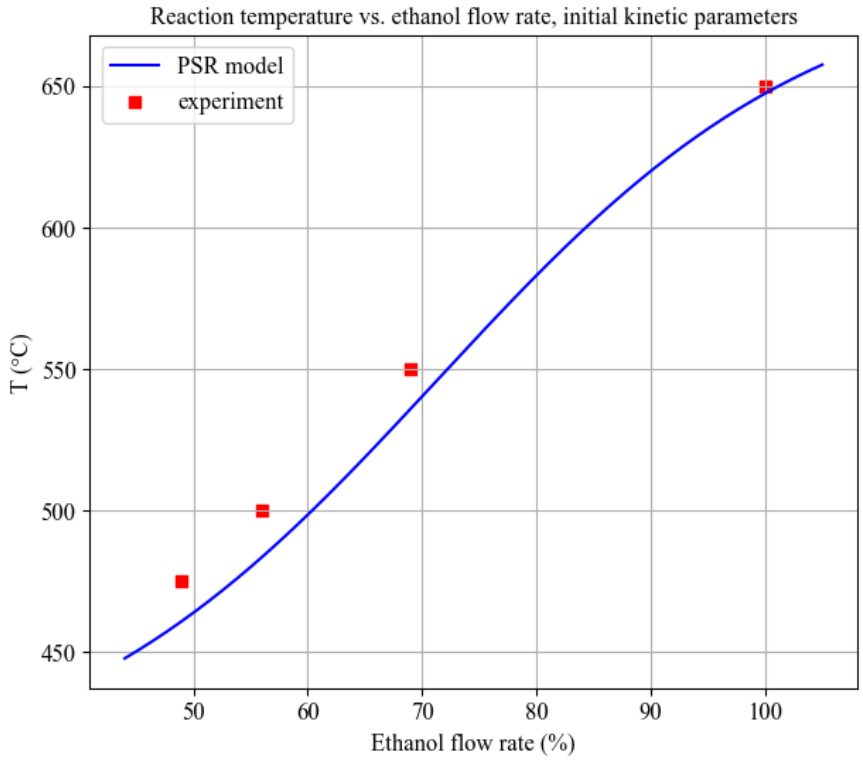

Figure 15. Reaction temperature, PSR model vs. experiment, Ea1 = 299 kJ/mol, baseline kinetic parameters

Ea_1 has a significant effect on the reaction temperature and ignition. Since the ignition was successful at this value, the reaction temperatures have been well-predicted and $Ea_1 = 299\ kJ/mol$ is the lowest uncertainty bound and therefore cannot be decreased further, the kinetic parameter that shall be increased is A2, which holds a significant effect on predicting CO concentration.

Simulations using the PSR model indicated that the prediction of CO concentration for all cases is highly sensitive to A2 and the residence time. Therefore, an initial CFD model was run using the ignition and the baseline kinetic parameters to determine the apparent residence time, $\tau_{apparent}$, which was then run afterward in the PSR model to estimate the appropriate A2.

The Ea_1 from the PSR simulation and all the other baseline values were then used in the initial CFD model. The results of the initial CFD model are shown in Table 4.2.

Table 4. 7. Kinetic parameters for the initial CFD model

Initial conditions, initial CFD model	Values
Ethanol flow rate	49% of 5 mol%
A1	$10^{21.82}$
Ea1	299 kJ/mol
A2	$10^{7.25}$
Ea2	120 kJ/mol

Table 4. 8. Initial CFD model results

Initial CFD model results	Values
$T_{reaction}$ (°C)	472.39
[CO] (ppm)	24,000

The initial CFD model gave a good temperature prediction but overpredicted the outlet CO concentration by orders of magnitude. To estimate the $\tau_{apparent}$, another set of CFD simulations was run using $A_2 = 4.01 \cdot 10^7$ and $A_2 = 5.20 \cdot 10^7$, increasing the A2 logarithmically within Helling's uncertainty bound while keeping the other kinetic parameters constant. The results for this test are shown in Table 4.4.

Table 4. 9. A2 vs. CO PPM

$A2$	$T_{reaction}$ (°C)	[CO] (ppm)
$1.78 \cdot 10^7$	472.39	24,000
$4.01 \cdot 10^7$	476	8528
$5.20 \cdot 10^7$	476	5136

Simulating these conditions in the PSR model, the apparent residence time was approximated to be

$$\tau_{apparent} = 38\ s \tag{32}$$

This is the apparent residence time in the CFD reactor model resulting from the effects of fluid recirculation, mixing, and density gradients. The obtained $\tau_{apparent}$ also agreed reasonably with the residence time estimation from the experiment [101]. At this residence time, $A_2 = 5.20 \cdot 10^7$ and the other previously established kinetic parameters well predicted

the reaction temperature, CO concentration, and the physical behavior of the SCWO reactor for the 49% ethanol case within 28.42%. The combination of the exact kinetic parameters is given in the table below.

Table 4. 10. Exact kinetic parameters for the CFD model

Initial conditions, CFD model	Values
A1	$10^{21.82} = 6.60 \cdot 10^{21}$
Ea1	$340 - 41\ kJ/mol = 299$ kJ/mol
A2	$10^{7.25+0.47} = 5.20 \cdot 10^{7}$
Ea2	120 kJ/mol

These kinetic parameters were used to model the CFD reaction for all the fuel loadings.

4.3. Reaction temperature comparison – model vs. experiment

The reaction temperature of the CFD model was measured at 178 mm from the inlet, which was the measurement point in the experiment.

Table 4. 11. Reactor center temperature

Ethanol flow rate	T center, CFD	T center, experiment	% difference
49%	471.13	475.00	0.82
56%	480.98	500.00	3.80
69%	526.02	550.00	4.36
100%	622.64	650	4.21

The reaction temperature between the CFD model and the experiment agrees within 4.36%. This agreement shows that the two-step mechanism model can accurately predict the reaction temperature at the center of the reactor.

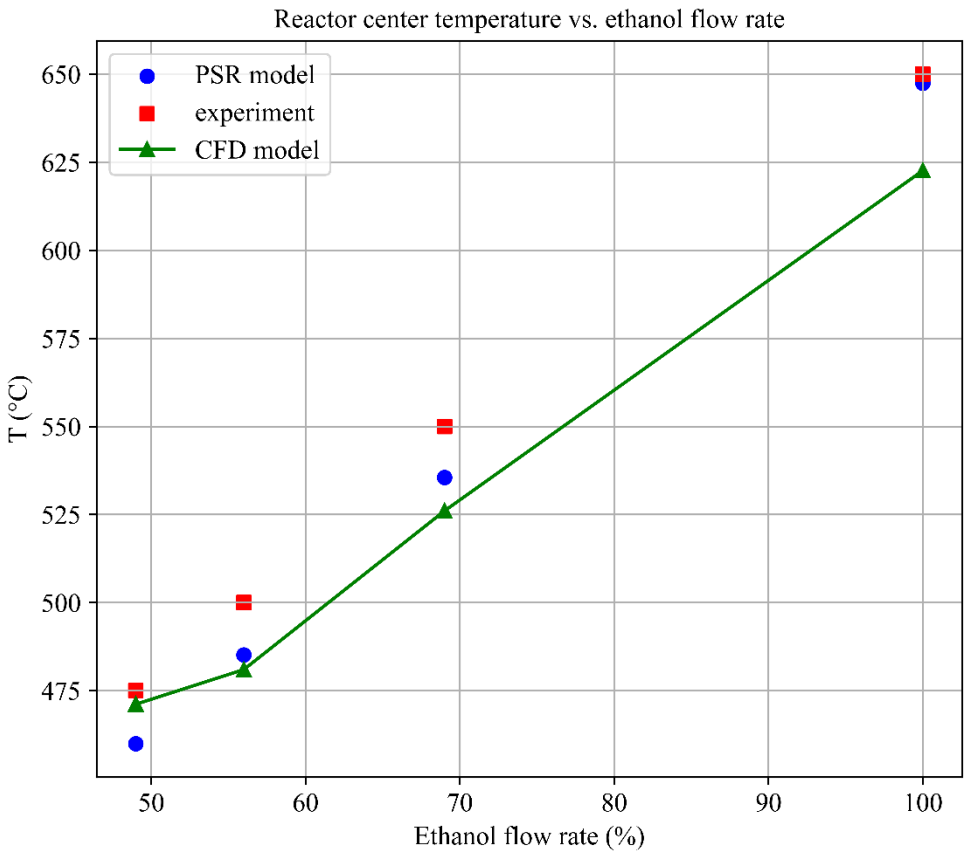

Figure 16. Reactor center temperature comparison, models vs. experiment

The reaction temperature in the PSR model was also assumed to be the reaction temperature present at the center of the reactor and was therefore compared in this data. The CFD model was able to arrive at a reasonable agreement with the PSR model.

The top section temperature was measured at 26 mm from the inlet. The comparison between the reactor top section temperature from the CFD model and the experiment is shown below.

Table 4. 12. Reactor top section temperature

Ethanol flow rate	T top, CFD	T top, experiment	% difference
49%	435.24	400.00	8.81
56%	444.00	415.00	6.99
69%	447.50	450.00	0.56
100%	484.51	510	4.99

For all cases, the top section temperature is overpredicted by the CFD by up to 8.81%. Similar overprediction behavior was also reported in the previous single-step mechanism modeling [1].

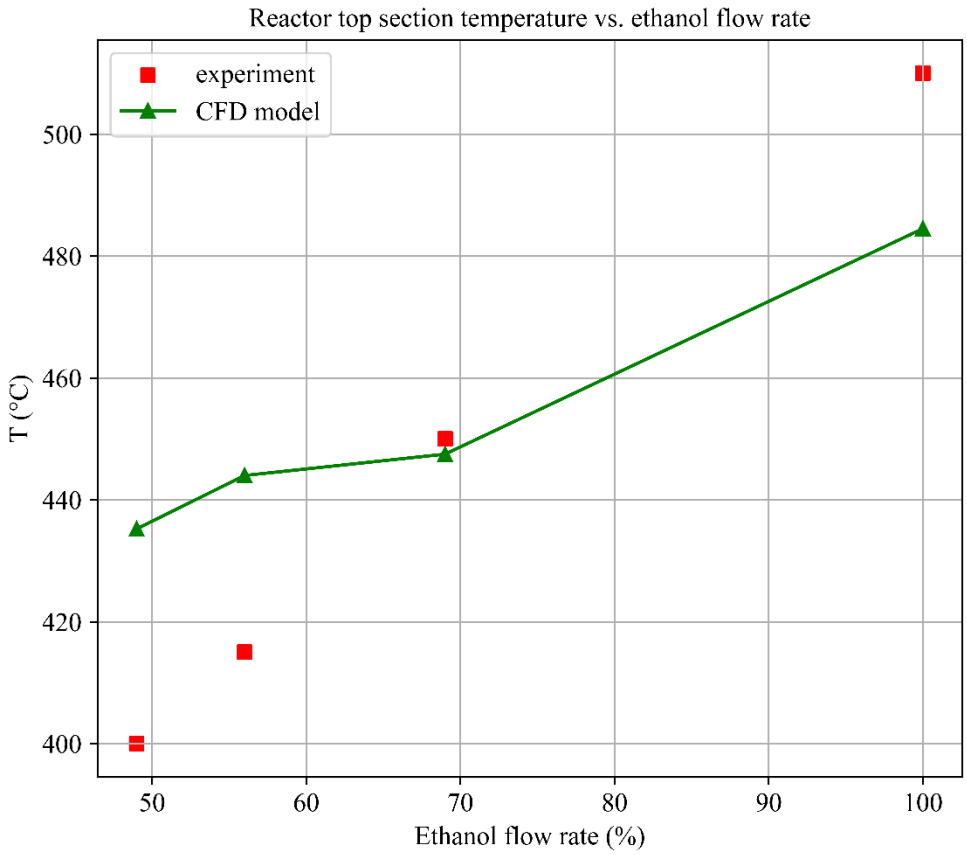

Figure 17. Reactor top section temperature vs. ethanol flow rate

Both observations suggest that the two-step mechanism model was still predicting early heat generation. However, compared to the single-step mechanism model, the two-step mechanism was able to predict the center temperature more accurately and predict a wider hot zone downstream of the reactor. The data from the table below were taken for the 100% ethanol flow rate with the modeled effects of heat transfer.

Table 4. 13. Reactor center temperature comparison (single vs two step mechanism)

Temperature (°C)		
CFD model, single-step mechanism	CFD model, two-step mechanism	Experiment
580.00	622.64	650.00

The single-step mechanism temperature prediction was obtained from Purohit et al.'s reactor model by using the same boundary conditions as the current modeling for a 5% fuel flow rate. It was suggested that the reaction rate of the single-step reaction might be too fast to convect heat downstream, while the two-step mechanism produces a delayed reaction that widens the range of the hot zone in the reactor, therefore providing a better prediction of the reactor center temperature.

4.4. Flow recirculation

Figure 18 shows the velocity vector of the fluid flow inside the reactor for all ethanol % cases all the way to the estimated end of the reaction zone. It can be observed that recirculation is present for all cases. Recirculation occurs because of density gradients. The hot reaction zone lowers the density of the supercritical mixture and induces buoyant flow. Recirculation in the reaction zone has been confirmed in previous modeling [33, 78] and has always been considered in SCWO reactor design. This recirculation brings hot product oxidation to the fresh charge, providing the opportunity for ignition.

The recirculation provides a higher residence time in the SCWO reactor [1], [2] as the reactants are being brought back to the reaction zone from the downstream. The higher residence time for the local reaction helps to promote a more complete oxidation of ethanol that is able to sustain heat generation. The incorporated effect of buoyancy in the reactor allows mixtures in higher temperature cases to achieve a more complete oxidation due to the lower mixture density.

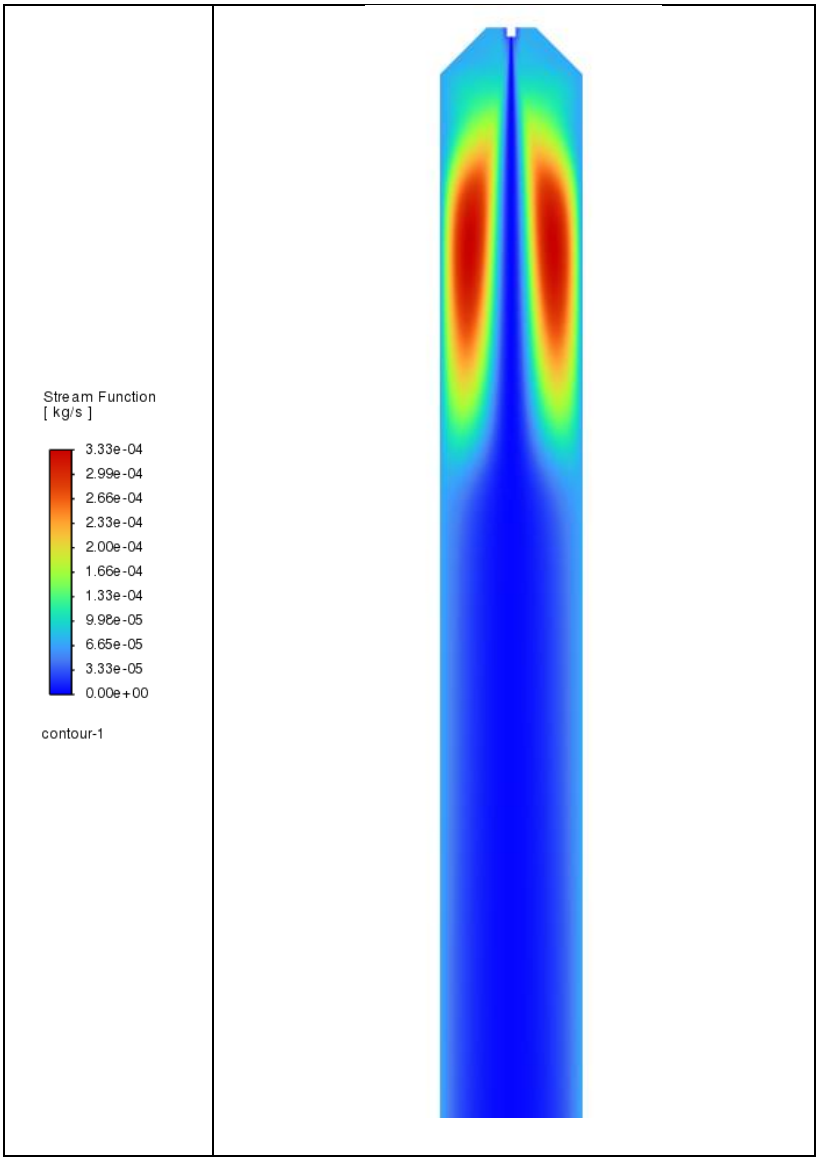

Figure 18. Stream function of the reactor

As had been well recognized by previous modeling and experiments of the SCWO reactor [33, 78], recirculating flow takes place at the outer radius of the nozzle. The heat generated by the reaction lowers the mixture density and therefore creates buoyant flow.

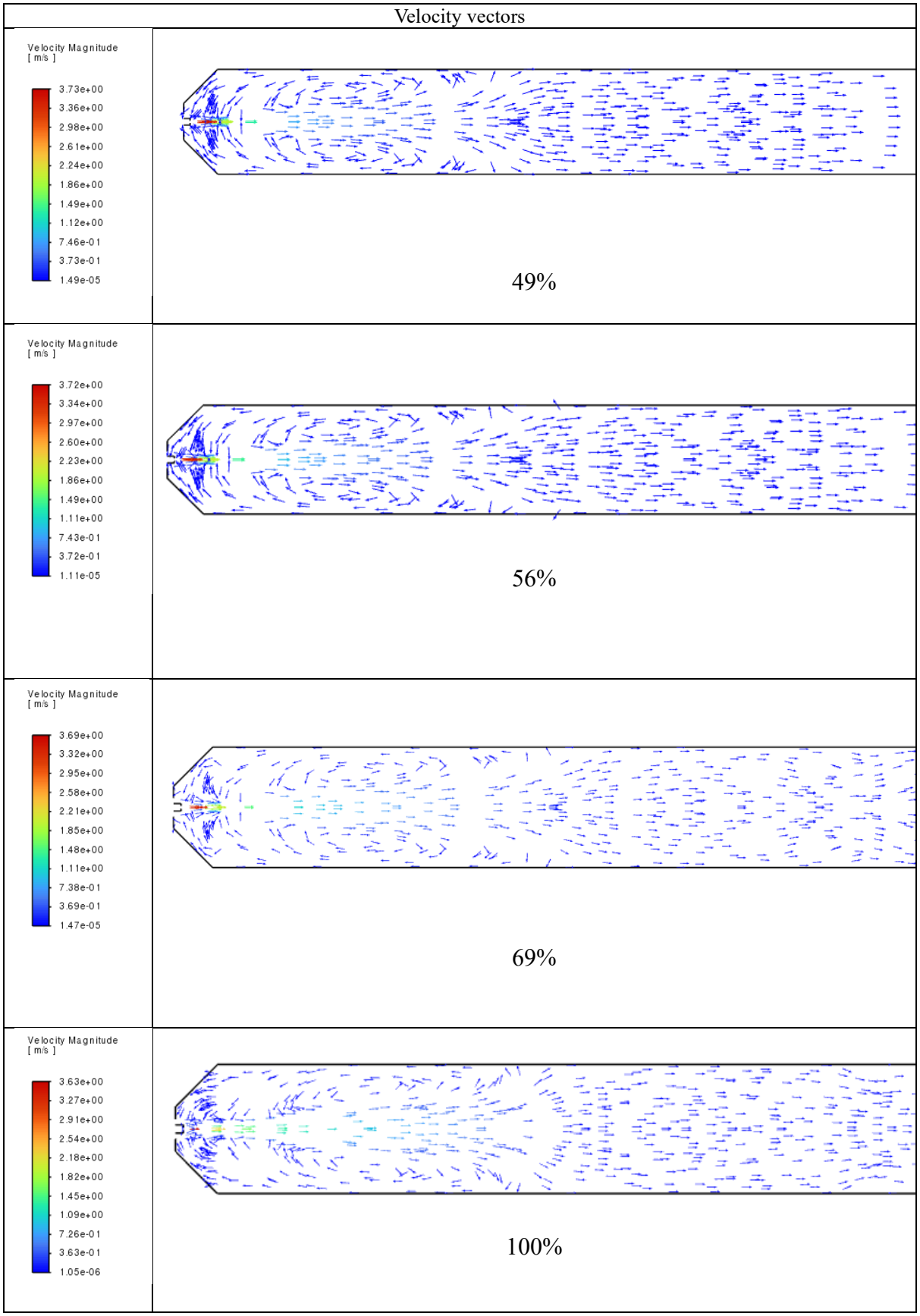

Figure 19. Velocity vectors

4.5. Temperature distribution

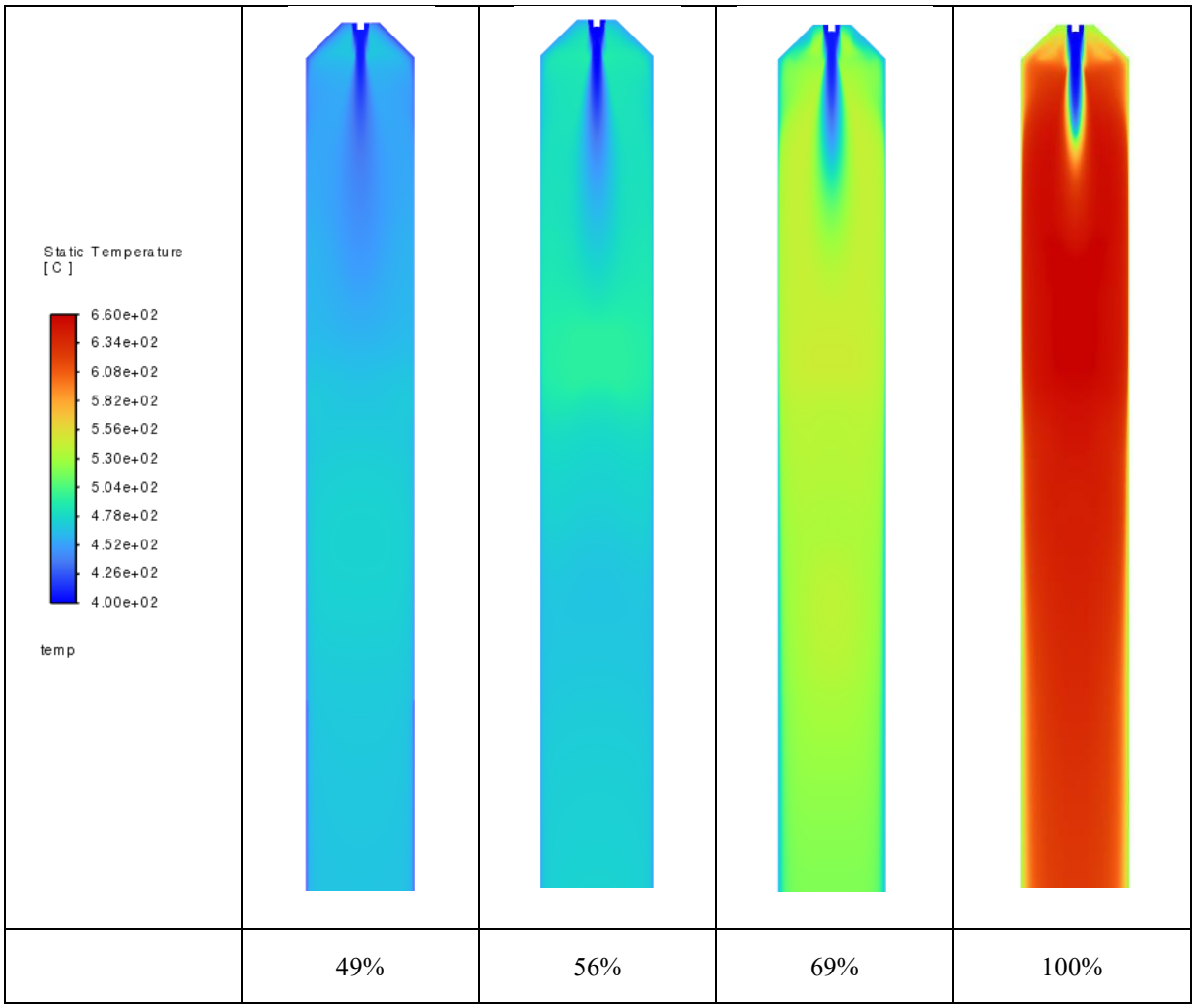

Figure 20. Temperature distribution (uniform scaling)

Figure 20 shows the temperature profile predictions for each of the fuel loadings all the way to 200 mm (eight diameters) downstream of the reactor. The overall temperature inside the reactor becomes higher with increasing ethanol flow rates. The heat released by the reaction moves from the reaction zone to the downstream. This thermal behavior is consistent with the exothermic reaction generating increasing heat with ethanol flow rates, as was observed in the previous SCWO model [1] and the experiment [101]. Autoignition was able to take place and sustain under the established kinetic rates. Once the oxidation takes place, it generates heat that

increases the temperature inside the reaction zone. It can also be observed that as the ethanol flow rate increases, the oxidation front becomes shorter and sharper. The increase in ethanol flow rate increases the temperature, which in turn accelerates the local oxidation rate. Therefore, oxidation takes place earlier upstream in higher ethanol flow rates. This behavior was also confirmed by the previous modeling of the SCWO reactor [1].

In lower temperature cases, the temperature is not inherently uniform along the reactor. Heat transfer to the titanium liner lowers the temperature as the supercritical mixture flows downstream. Weaker oxidation induces lower sustaining heat downstream of the reaction zone. The same behavior was reported in previous SCWO reactor modeling and experiments [33, 101]. The high temperature in the reaction zone induces buoyancy effects due to the reduction of the mixture density. As the fluid recirculates in the reaction zone, the residence time increases, which promotes a higher rate of oxidation. Hence, the reaction zone remains as the hottest region across all cases.

4.6. CO concentration comparison – model vs. experiment

The CO concentration, along with the scH_2O, was measured at the physical outlet using mass-weighted average calculation. The CO concentration in PPM was calculated on a dry basis. In the lower reaction temperature cases, higher CO concentration is consistent with its slower conversion rate. This phenomenon was confirmed by experiment [52]. Overall, the CO concentration between the CFD model and the experiment is in agreement within a 28.42% difference.

Table 4. 14. CO concentration vs. ethanol flow rate, CFD model vs. experiment

Ethanol flow rate	CFD model			Experiment	% difference
	Mol fraction, wet basis		Mol fraction, dry basis	Mol fraction, dry basis	
	CO	H_2O	CO (PPM)	CO (PPM)	
49%	$7.57 \cdot 10^{-4}$	0.85	5136.67	4000	28.42%
56%	$7.83 \cdot 10^{-5}$	0.83	452.39	400	13.10%
69%	$1.62 \cdot 10^{-5}$	0.79	78.19	70	11.70%
100%	$1.55 \cdot 10^{-7}$	0.73	0.57	0	-

The difference percentages between the CFD model and the experiment may be attributable to physical differences in the model's setup compared to the experiment, where the experiment incorporated the effects of reagent flow and quenching, and the sensitivity of CO values to the mesh resolution selected for the model. The values of the CO mol fraction measured from the CFD model for the 49% case changed by less than 0.5% over the last 50 timesteps, while the 56% and 69% flow rate cases changed within 5.5% over the last 100-time steps after approximately 500,000 timesteps in the simulations.

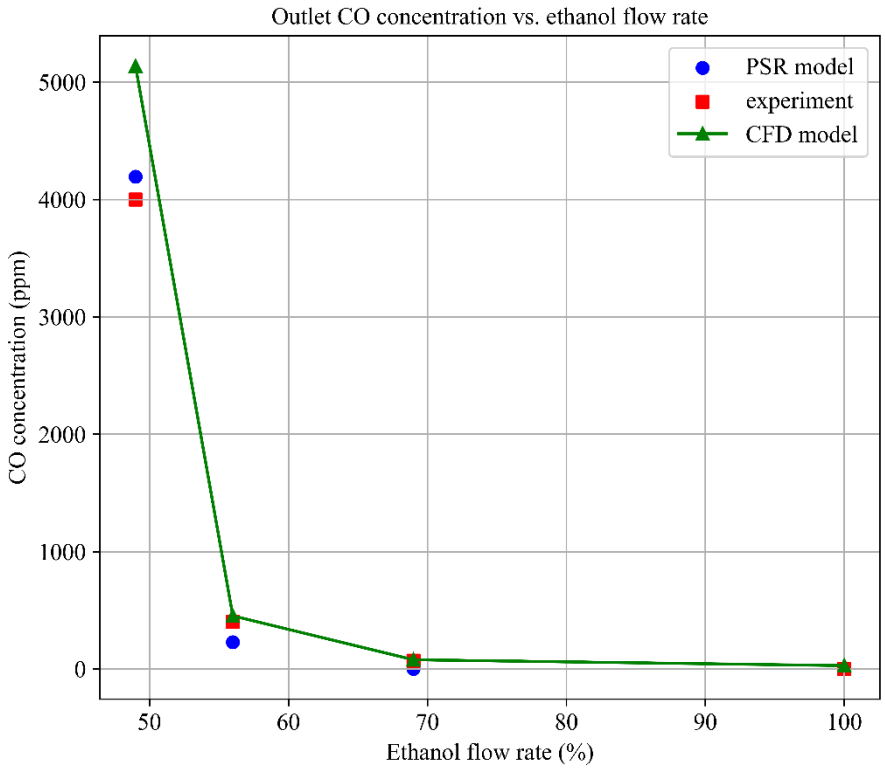

Figure 21. CO concentrations in PPM vs. ethanol flow rate (%)

This finding suggests that even though the established kinetic rate was originally adjusted for the 49% ethanol case, the rate remained reasonably applicable across all the test cases and was able to reasonably predict the CO concentrations.

4.7. CO distribution

Figure 22 shows the CO mol fraction distribution all the way to eight diameters of the reactor (200 mm downstream). At lower ethanol flow rates (and therefore lower reaction temperatures), CO becomes more concentrated in the reactor due to the slower rate of CO oxidation into CO_2. Across all fuel loadings, the highest CO concentration remains relatively similar. However, it was observed that as the ethanol flow rate becomes higher, the region where CO is present becomes shorter.

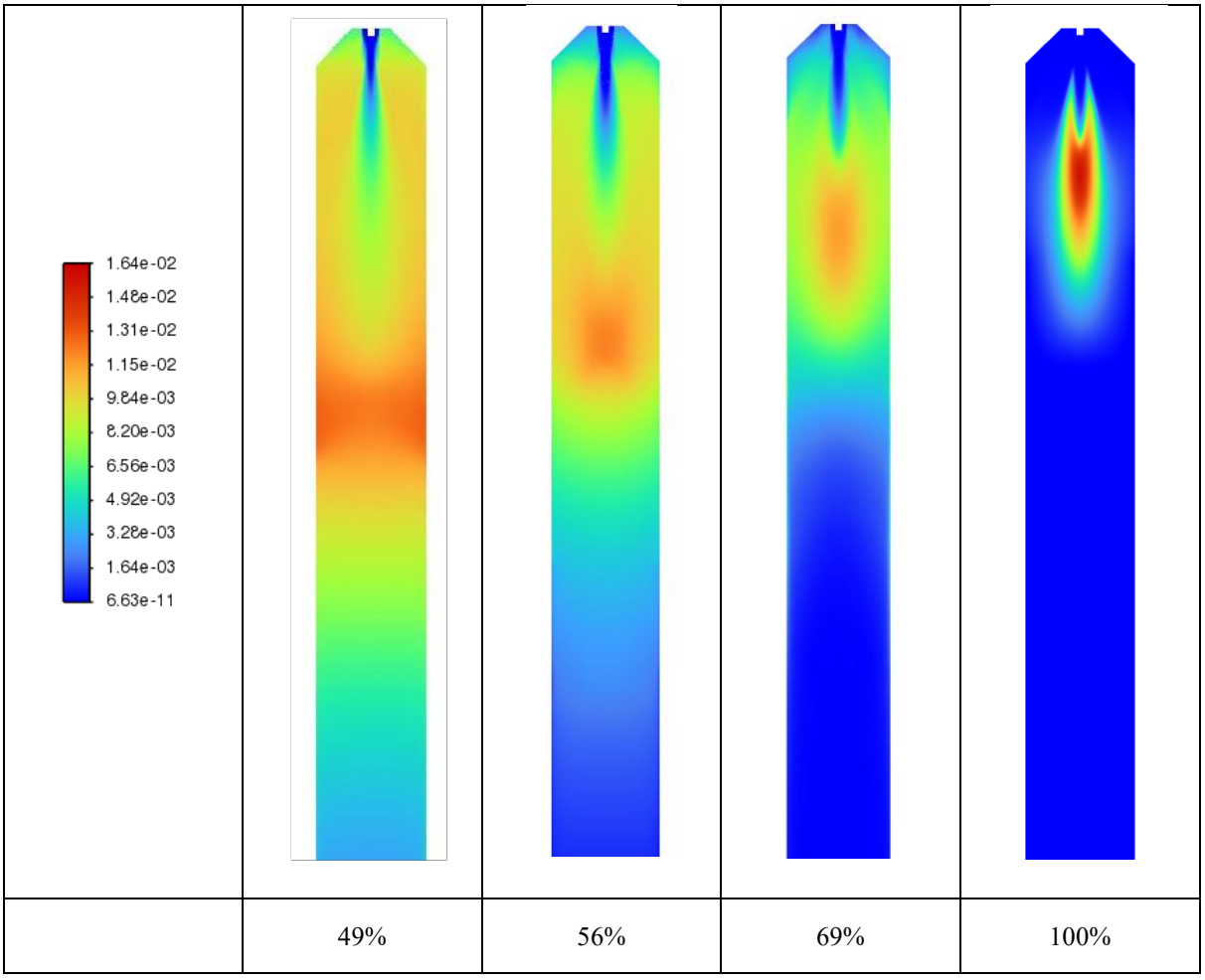

Figure 22. CO distribution map for each % ethanol case

The CO region decreases with an increase in ethanol flow rate and reaction temperature due to the strengthening influence of the second step kinetic rate. At lower temperatures, the

second-step kinetic rate becomes less concentrated as the fluid goes downstream, allowing CO to populate downstream without being immediately converted into CO_2. At the lower temperatures, it was also observed that more CO remained around the mixing zone due to incomplete oxidation in the reaction layer. At the highest ethanol flow rate (100% flow rate of 5 mol% ethanol), the intermediate CO around the mixing area becomes less present due to a higher and more concentrated rate of CO consumption. The higher concentration of CO downstream promotes higher CO presence in the outlet product, as confirmed by the outlet measurements from experiment [101].

4.8. Oxidation characteristics

Table 4.10 shows the local peak oxidation rates of reaction-1 (ethanol conversion into CO) and reaction-2 (CO conversion into CO_2). The local peaks of both reaction steps increase with the ethanol flow rate. Reaction-1 showed a higher rate of exponential increase compared to reaction-2 at the higher reaction temperature. This is consistent with Helling's reaction mechanism for CO production, which has roughly double the exponential factor for the temperature dependence.

Table 4. 15. Local peak oxidation rates vs. ethanol flow rate

Ethanol flow rate	R1, local peak (kmol/m^3/s)	R2, local peak (kmol/m^3/s)
49%	$1.87 \cdot 10^{-2}$	$3.90 \cdot 10^{-3}$
56%	$4.43 \cdot 10^{-2}$	$7.80 \cdot 10^{-3}$
69%	$3.82 \cdot 10^{-1}$	$1.25 \cdot 10^{-2}$
100%	$3.86 \cdot 10^{1}$	$6.64 \cdot 10^{-2}$

Figures 23 and 24 show the kinetic rate distributions for reaction-1 and reaction-2 along the reactor up to 200 mm. The main reaction takes place in the mixing layer where the coaxially injected ethanol and oxygen streams meet. Both reaction-1 and reaction-2 show similar behavior. The local kinetic rate increases with ethanol flow rate, while the reaction zone becomes more concentrated into the mixing region. As the ethanol % increases, the reaction happens more immediately as the ethanol mixes with oxygen.

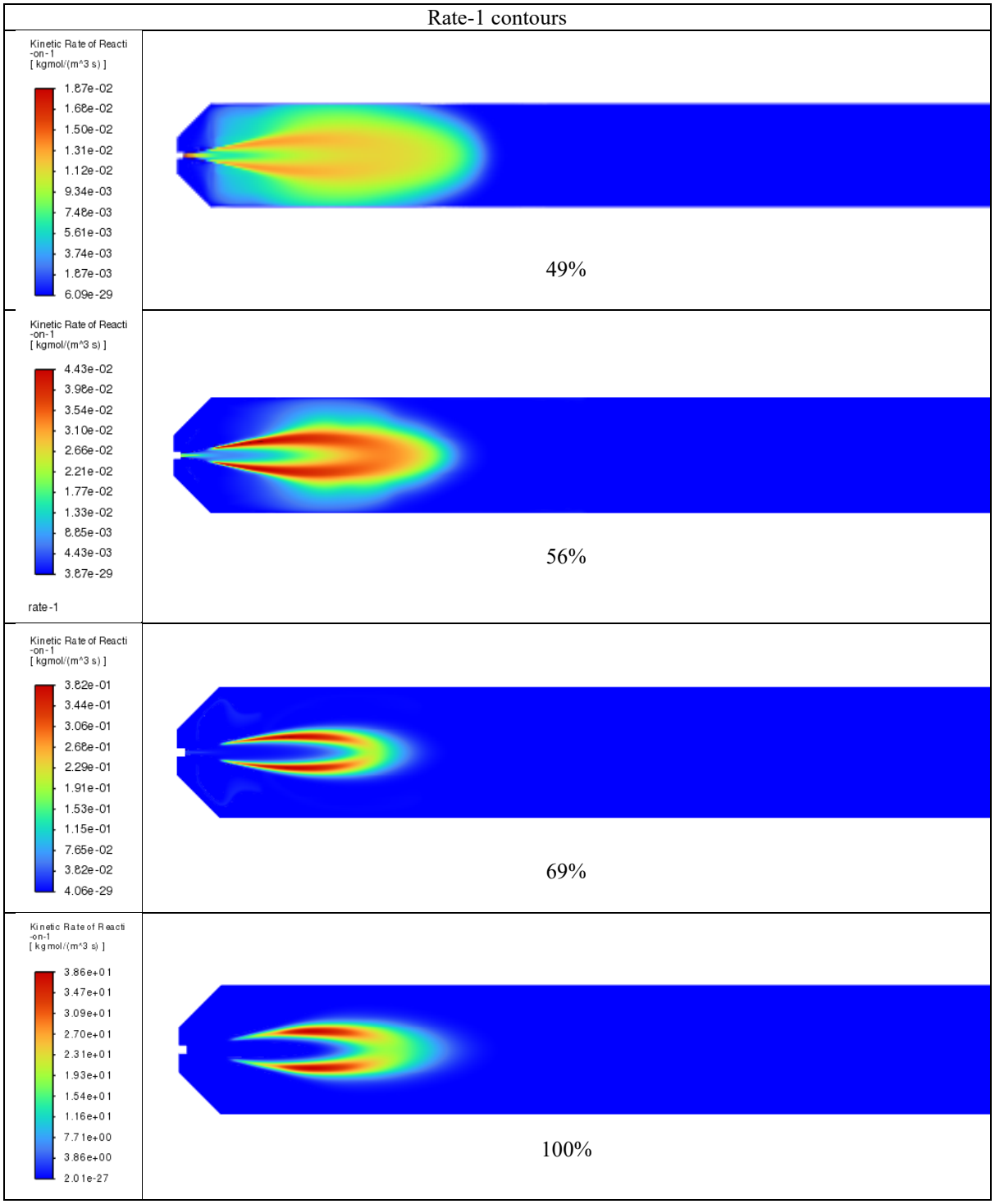

Figure 23. Rate-1 contour for each ethanol flow rate case

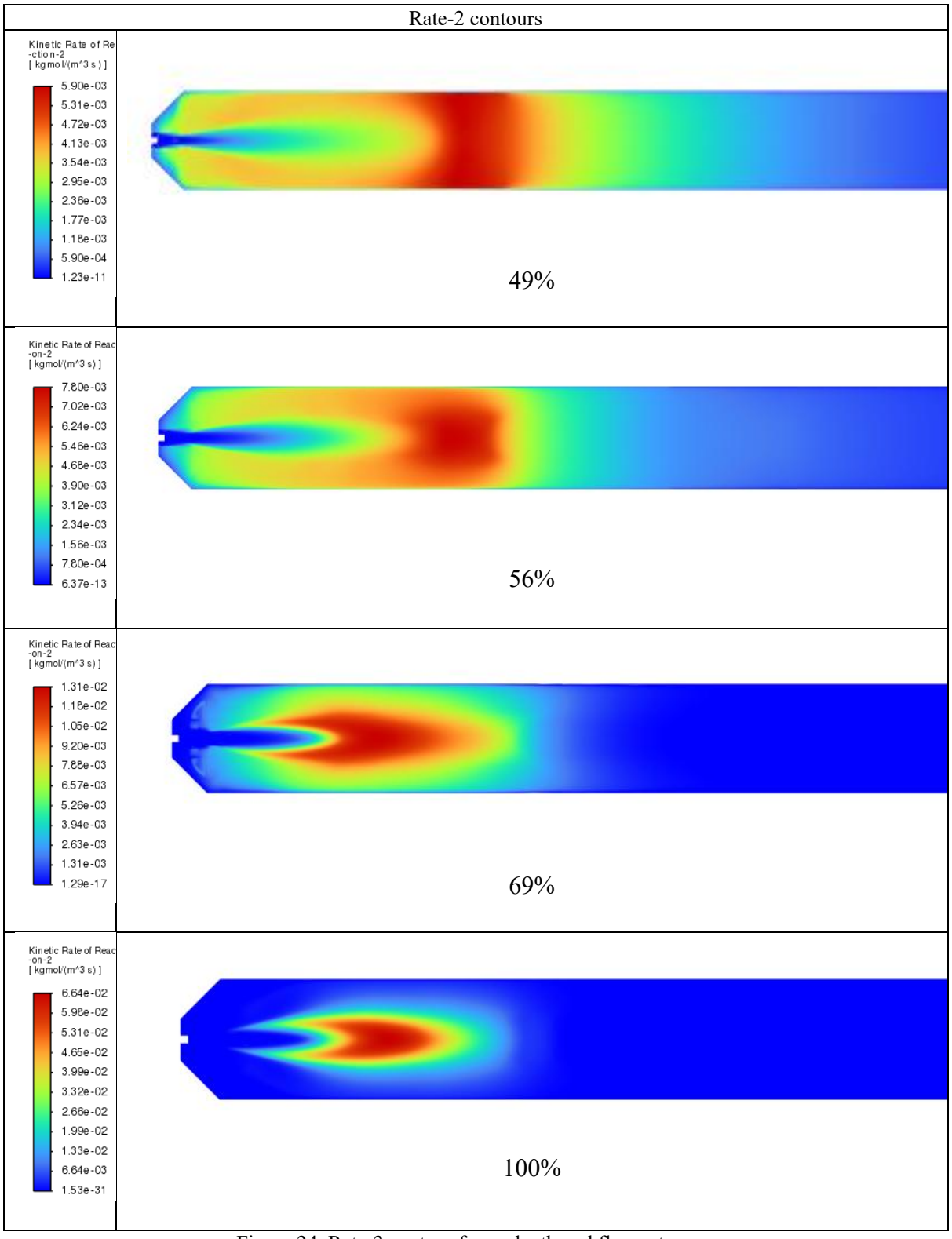

Figure 24. Rate-2 contour for each ethanol flow rate case

As ethanol is increased, reaction-1 produces more CO that concentrates in the mixing region at a higher rate, which is then converted further to CO_2 immediately in the same region by reaction-2. At lower reaction temperatures, reaction-1 rates are lower and more spatially spread out, promoting the presence of CO in a wider area to be further converted into CO_2 in the second reaction. However, the lower reaction-2 rate allows CO to be present more significantly both downstream and radially.

As the fluid moves further downstream of the reaction zone, the non-zero reaction-2 rate at downstream allows more conversion of CO into CO_2. This mechanism explains the presence of leftover CO at the downstream that is not being converted into CO_2 and the increasing presence of downstream CO_2 at lower reaction temperatures and lower ethanol flow rates.

4.9. Product species comparison with PSR model

Tables 4.11-4.14 show the comparison of the measured outlet products between the CFD model and the PSR model in mol fractions. The PSR model was used for this comparison due to the unavailability of individual product mol fraction data from the experiment. Overall, the product of the reaction in the CFD model showed reasonable agreement with PSR model calculations, which were done analytically. The highest difference between the two models is in the CO production in the 56% case. The underprediction is likely attributable to the fluid flow behavior that was not a part of the PSR model. The PSR model assumes a perfectly mixed domain, while the CFD model captured the effects of non-perfect mixing caused by plug-flow-like behavior, which allows the species to flow downstream before completing oxidation. The CO concentrations for all cases match the experiment more closely than the PSR model, suggesting that the experiment and the CFD model capture fluid-flow behavior that was not present in the PSR model. The overall agreement with the PSR model suggests that the finite-

rate chemistry, thermophysical properties, and reaction rates can predict the chemical reaction reasonably well compared to the semi-analytical calculations.

Table 4. 16. Product mol fraction comparison, 49% fuel flow rate

49% ethanol flow rate			
	Mol fraction (mol/mol)		
Species	CFD model	PSR model	% difference
C_2H_5OH	0.00000	0.00000	-
O_2	0.00290	0.00390	25.64000
N_2	0.12450	0.12430	0.13000
CO	0.00076	0.00060	26.16667
CO_2	0.02020	0.01900	6.36000
H_2O	0.85260	0.85200	0.07000

Table 4. 17. Product mol fraction comparison, 56% fuel flow rate

56% ethanol flow rate			
	Mol fraction (mol/mol)		
Species	CFD model	PSR model	% difference
C_2H_5OH	0.00000	0.00000	-
O_2	0.00640	0.00600	6.83000
N_2	0.14500	0.14480	0.12000
CO	0.00008	0.00004	49.68072
CO_2	0.02160	0.02160	0.18000
H_2O	0.82690	0.82750	0.07000

Table 4. 18. Product mol fraction comparison, 69% fuel flow rate

69% ethanol flow rate			
	Mol fraction (mol/mol)		
Species	CFD model	PSR model	% difference
C_2H_5OH	0.00000	0.00000	-
O_2	0.00725	0.00690	4.82000
N_2	0.17230	0.16970	1.52000
CO	0.00001	0.00000	-
CO_2	0.02860	0.02550	11.96000
H_2O	0.79630	0.79790	0.20000

Table 4. 19. Product mol fraction comparison, 100% fuel flow rate

100% ethanol flow rate			
	Mol fraction (mol/mol)		
Species	CFD model	PSR model	% difference
C_2H_5OH	0	0.00000	-
O_2	0.00845	0.01040	18.75
N_2	0.22625	0.22520	0.466
CO	0.00000	0.00000	-
CO_2	0.03704	0.03300	12.24
H_2O	0.72824	0.73140	0.43

4.10. Reactants mole fraction distribution

Figure 25 shows the ethanol mol fraction contour for all the test cases taken up to 200 mm downstream. Across all the test cases, the bulk region of the reactor consistently showed near-zero presence of ethanol, indicating that ethanol is completely consumed in the reaction shortly after entering the reactor.

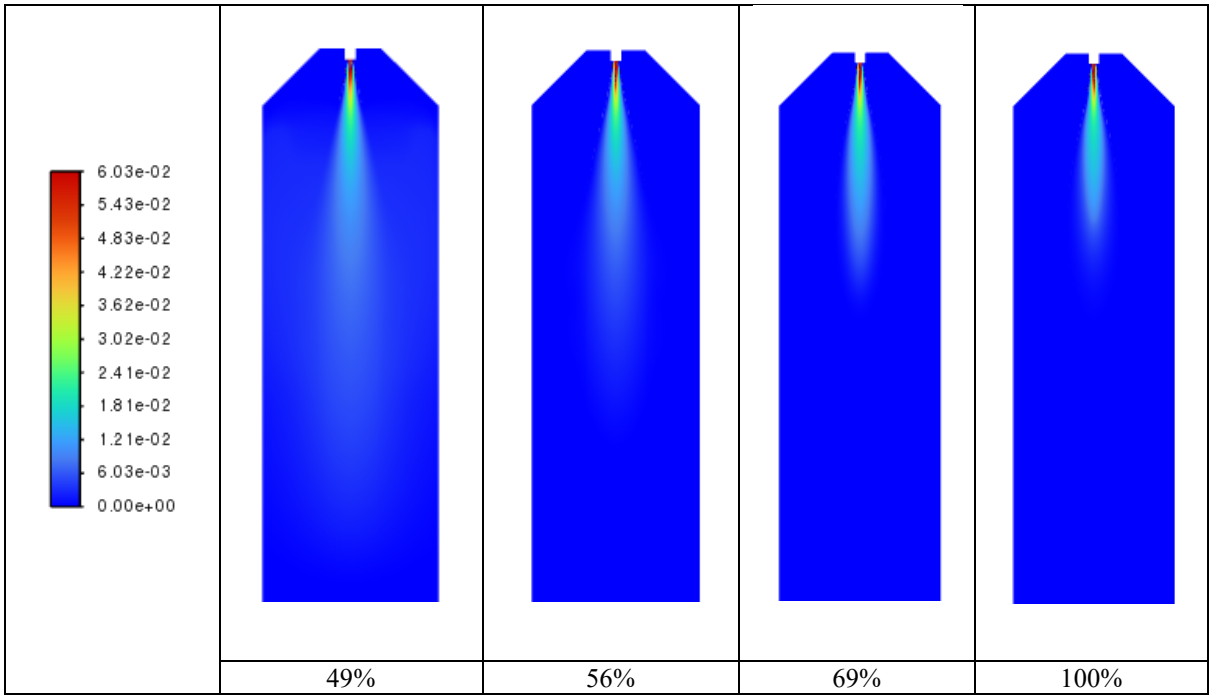

Figure 25. Ethanol mol fraction distribution

The ethanol jet length decreases with ethanol flow rate. This is due to the higher kinetic rate of ethanol consumption with higher reaction-1 kinetic rate. As more ethanol % is introduced into the reactor, the ethanol consumption rate (reaction rate-1) increases, which increases the reaction temperature. The increase in the reaction rate provides a shorter runway for the first reaction to occur, making the ethanol burn earlier upstream from the nozzle. The ethanol jet is longer and more dispersed downstream at lower reaction temperatures, while

becoming shorter and more concentrated at higher reaction temperatures. This behavior is consistent with the kinetic rate distribution shown in section 4.7.

Figure 26 shows the oxygen mol fraction contours for all the test cases taken up to 200 mm downstream. For all cases, leftover oxygen is present inside the reactor. This phenomenon has been confirmed experimentally and analytically, due to the use of lean fuel mixture with the maintained air-to-fuel ratio of $\phi = 1.2$. With this air-to-fuel ratio, oxygen is expected to always be present regardless of the chemical kinetics.

The leftover oxygen from the reaction zone is observed to fill out space within the reaction during steady state condition. Some of leftover oxygen from the first reaction that did not immediately get consumed by the first reaction were available downstream to be used in converting CO to CO_2.

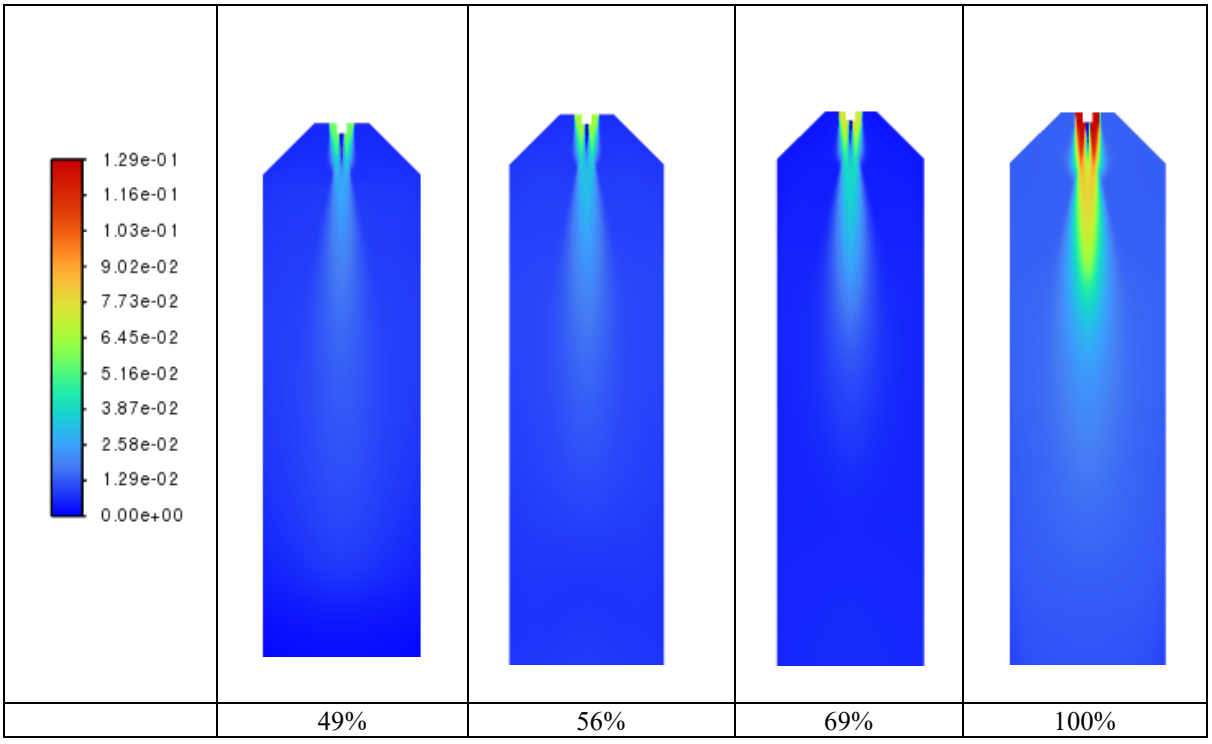

Figure 26. O2 mol fraction distribution

The amount of leftover oxygen downstream from the first reaction was present to be used in reaction-2 to convert the remaining downstream CO into CO_2, providing additional

reaction zone in lower ethanol % cases. With increasing ethanol flow rates, oxygen concentration was also increased by the appropriate amount to maintain $\phi = 1.2$.

4.11. CO_2 formation

Figure 27 shows the CO_2 mol fraction contours for all the test cases taken up to 200 mm downstream. CO_2 production increases with ethanol flow rate.

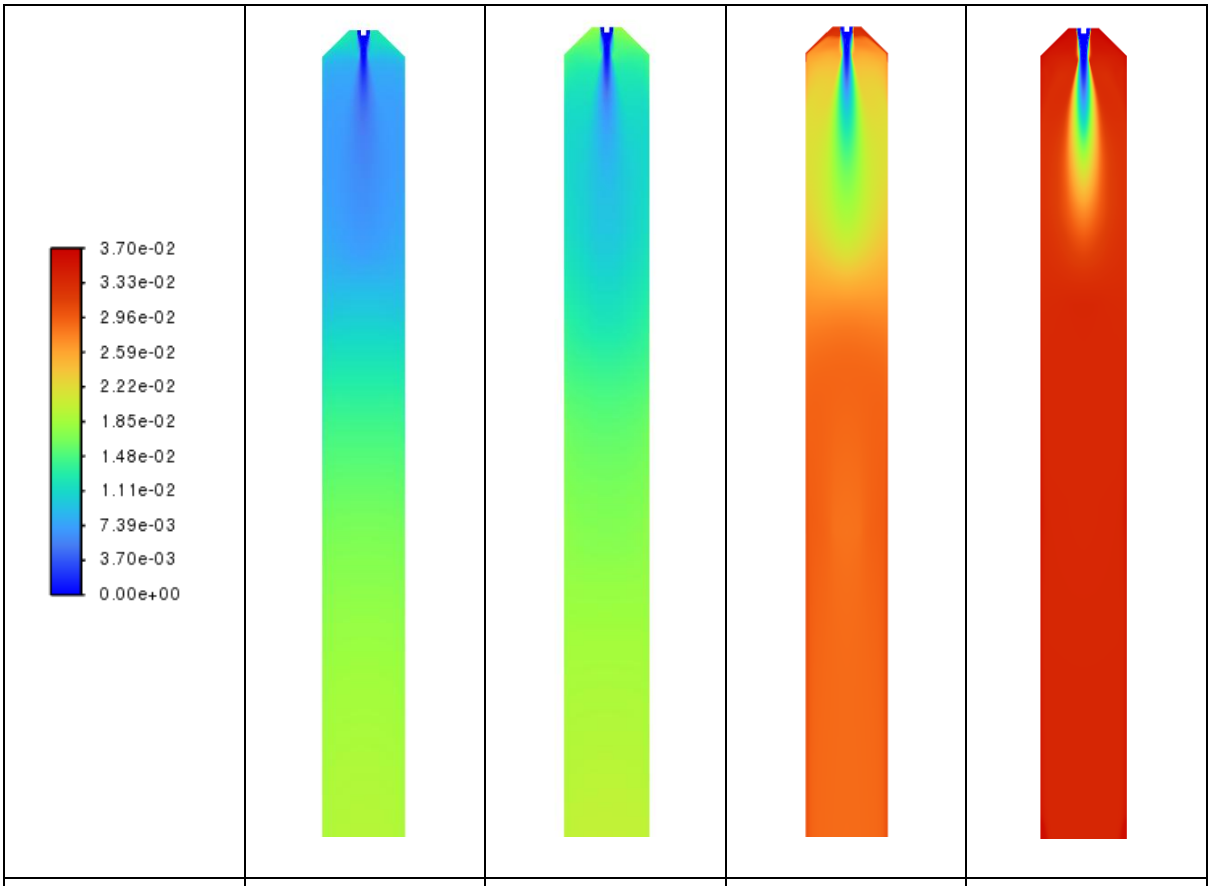

Figure 27. CO_2 distribution

Higher ethanol flow rate provides more hydrocarbon to be converted into CO_2. As has been previously established, the increase in ethanol flow rate additionally provides higher rates of oxidation and heat generation. The CFD model, the PSR model, and the experiment show a similar overall trend of CO_2 increase with ethanol flow rate.

At the lower temperature cases up to 68% ethanol, the $CO \rightarrow CO_2$ conversion rate is not as strong to completely produce CO_2 in the main reaction zone as the 100% ethanol case. Instead, the reaction zone was initially dominated by CO.

The CO conversion rates in the lower fuel loadings are more spatially spread out, creating more reaction zone downstream to produce CO_2. With lower concentrations of CO and fuel, heat generation becomes weaker, resulting in lower downstream temperatures.

As ethanol flow rate % increases, higher CO_2 formation takes place upstream and forms a more uniform CO_2 distribution along the reactor. For the 100% ethanol dilution case, CO_2 formation happens more immediately in the main reaction zone and provides the reactor with uniform CO_2 distribution along the reactor at steady state.

The concentration of CO_2 along the reactor in lower-temperature cases is inversely proportional to the CO concentration. As more CO initially formed downstream, more of it is being converted into CO_2. This mechanism provides more CO_2 as CO becomes less present when the fluid moves further downstream.

Chapter 5. Conclusions

A 2D axisymmetric CFD model for a lab-scale SCWO reactor is presented. This study characterized the thermodynamics, species distribution, and hydrodynamic behavior of the SCWO reactor based on two-step ethanol oxidation. UW SCWO reactor was operated with four different fuel loadings (49%, 56%, 69%, and 100%). Comparison with experimental data validated the modeling approach over the range of operating temperatures. The CFD model predicted reaction temperatures within 8.81% of the experimental and semi-analytical model results. The CFD model was also able to predict the CO concentration by the end of the reaction within 28.42% of the experiment. This finding suggests that Helling et al.'s two-step kinetic mechanism, within the published uncertainty bounds, was able to reasonably model ethanol oxidation within the SCWO reactor under the conditions of 25 MPa and temperatures up to 650 °C for the test cases. The temperature and spatial distribution of C_2H_5OH, O_2, CO and CO_2 showed good agreement with the experiment. The two-step mechanism model still predicted earlier heat generation than the experiment. The two-step mechanism has the advantage over the single-step mechanism; it can characterize the delayed heat release from ethanol oxidation and therefore predict the reactor center temperature better than the single-step mechanism. The study provides insight into future design improvements and upscaling of SCWO reactors.

Future studies that may improve upon the findings are needed, such as additional validation against more experimental data points, a more comprehensive CFD modeling using more than two-step kinetics, and a comparison study on how well the 2D axisymmetric model fares against a 3D CFD model. Future studies that may build upon this work include incorporating PFAS destruction into the CFD model to study the mechanism of PFAS destruction.

References

[1] R. K. Helling and J. W. Tester, "Oxidation of Simple Compounds and Mixtures in Supercritical Water: Carbon Monoxide, Ammonia, and Ethanol," *Environmental Science and Technology,* 1988.

[2] A. F. Peritore, E. Gugliandolo, S. Cuzzocrea, R. Crupi, and D. Britti, "Current Review of Increasing Animal Health Threat of Per- and Polyfluoroalkyl Substances (PFAS): Harms, Limitations, and Alternatives to Manage Their Toxicity," in *International Journal of Molecular Sciences* vol. 24, ed: Multidisciplinary Digital Publishing Institute (MDPI), 2023.

[3] S. National Institute of Environmental Health, "Perfluoroalkyl and Polyfluoroalkyl Substances (PFAS)," ed.

[4] E. a. M. National Academies of Sciences, "Introduction," in *Guidance on PFAS Exposure, Testing, and Clinical Follow-Up.* Washington (DC): National Academies Press, 2022.

[5] Itrc, *History and use of per- and polyfluoroalkyl substances (PFAS)*. 2017.

[6] S. E. Fenton *et al.*, "Per- and Polyfluoroalkyl Substance Toxicity and Human Health Review: Current State of Knowledge and Strategies for Informing Future Research," in *Environmental Toxicology and Chemistry* vol. 40, ed: Wiley Blackwell, 2021, pp. 606–630.

[7] A. United States Environmental Protection, "Our Current Understanding of the Human Health and Environmental Risks of PFAS."

[8] L. P. Padhye *et al.*, "The PFAS roadmap–Navigating a path together to improved management," *Sustainability Science and Technology,* vol. 3, no. 1, p. 012501, 2026/02/16 2026, doi: 10.1088/2977-3504/ae286f.

[9] S. Yang, S. Fernando, T. M. Holsen, and Y. Yang, "Inhibition of Perchlorate Formation during the Electrochemical Oxidation of Perfluoroalkyl Acid in Groundwater," *Environmental science & technology letters,* vol. 6, no. 12, pp. 775–780, 2019, doi: 10.1021/acs.estlett.9b00653.

[10] J. Radjenovic, N. Duinslaeger, S. S. Avval, and B. P. Chaplin, "Facing the Challenge of Poly- and Perfluoroalkyl Substances in Water: Is Electrochemical Oxidation the Answer?," *Environmental science & technology,* vol. 54, no. 23, pp. 14815–14829, 2020, doi: 10.1021/acs.est.0c06212.

[11] R. K. Singh, S. Fernando, S. F. Baygi, N. Multari, S. M. Thagard, and T. M. Holsen, "Breakdown Products from Perfluorinated Alkyl Substances (PFAS) Degradation in a Plasma-Based Water Treatment Process," *Environmental science & technology,* vol. 53, no. 5, pp. 2731–2738, 2019, doi: 10.1021/acs.est.8b07031.

[12] H. McIntyre, V. Minda, E. Hawley, R. Deeb, and M. Hart, "Coupled photocatalytic alkaline media as a destructive technology for per- and polyfluoroalkyl substances in

aqueous film-forming foam impacted stormwater," *Chemosphere (Oxford),* vol. 291, no. Pt 1, p. 132790, 2022, doi: 10.1016/j.chemosphere.2021.132790.

[13] H. Zhang, J.-X. Chen, J.-P. Qu, and Y.-B. Kang, "Photocatalytic low-temperature defluorination of PFASs," *Nature (London),* vol. 635, no. 8039, pp. 610–617, 2024, doi: 10.1038/s41586-024-08179-1.

[14] C. D. Vecitis, Y. Wang, J. Cheng, H. Park, B. T. Mader, and M. R. Hoffmann, "Sonochemical Degradation of Perfluorooctanesulfonate in Aqueous Film-Forming Foams," *Environmental science & technology,* vol. 44, no. 1, pp. 432–438, 2010, doi: 10.1021/es902444r.

[15] K. Zhang, J. Huang, G. Yu, Q. Zhang, S. Deng, and B. Wang, "Destruction of Perfluorooctane Sulfonate (PFOS) and Perfluorooctanoic Acid (PFOA) by Ball Milling," *Environmental science & technology,* vol. 47, no. 12, pp. 6471–6477, 2013, doi: 10.1021/es400346n.

[16] N. Wang *et al.*, "Complete Defluorination and Mineralization of Perfluorooctanoic Acid by a Mechanochemical Method Using Alumina and Persulfate," *Environmental science & technology,* vol. 53, no. 14, pp. 8302–8313, 2019, doi: 10.1021/acs.est.9b00486.

[17] N. Yang *et al.*, "PFAS destruction and near-complete defluorination of undiluted aqueous film-forming foams at ambient conditions by piezoelectric ball milling," *Environmental science & technology,* vol. 59, no. 3, pp. 1854–1863, 2025.

[18] J. Li, B. R. Pinkard, S. Wang, and I. V. Novosselov, "Review: Hydrothermal treatment of per- and polyfluoroalkyl substances (PFAS)," *Chemosphere,* vol. 307, p. 135888, 2022/11/01/ 2022, doi: https://doi.org/10.1016/j.chemosphere.2022.135888.

[19] C. Austin, J. Li, S. Moore, A. Purohit, B. R. Pinkard, and I. V. Novosselov, "Destruction and defluorination of PFAS matrix in continuous-flow supercritical water oxidation reactor: Effect of operating temperature," *Chemosphere (Oxford),* vol. 327, p. 138358, 2023, doi: 10.1016/j.chemosphere.2023.138358.

[20] M. J. Krause *et al.*, "Supercritical Water Oxidation as an Innovative Technology for PFAS Destruction," *Journal of environmental engineering (New York, N.Y.),* vol. 148, no. 2, pp. 1–8, 2022, doi: 10.1061/(ASCE)EE.1943-7870.0001957.

[21] J. Li, C. Austin, S. Moore, B. R. Pinkard, and I. V. Novosselov, "PFOS destruction in a continuous supercritical water oxidation reactor," *Chemical engineering journal (Lausanne, Switzerland : 1996),* vol. 451, p. 139063, 2023, doi: 10.1016/j.cej.2022.139063.

[22] B. R. Pinkard, S. Shetty, D. Stritzinger, C. Bellona, and I. V. Novosselov, "Destruction of perfluorooctanesulfonate (PFOS) in a batch supercritical water oxidation reactor," *Chemosphere (Oxford),* vol. 279, p. 130834, 2021, doi: 10.1016/j.chemosphere.2021.130834.

[23] S. Hao, Y.-J. Choi, B. Wu, C. P. Higgins, R. Deeb, and T. J. Strathmann, "Hydrothermal Alkaline Treatment for Destruction of Per- and Polyfluoroalkyl Substances in Aqueous Film-Forming Foam," *Environmental Science & Technology,* vol. 55, no. 5, pp. 3283–3295, 2021/03/02 2021, doi: 10.1021/acs.est.0c06906.

[24] S. Hao, Y. J. Choi, R. A. Deeb, T. J. Strathmann, and C. P. Higgins, "Application of Hydrothermal Alkaline Treatment for Destruction of Per- and Polyfluoroalkyl Substances in Contaminated Groundwater and Soil," *Environmental Science & Technology,* vol. 56, no. 10, pp. 6647–6657, 2022/05/17 2022, doi: 10.1021/acs.est.2c00654.

[25] S. Hao *et al.*, "Hydrothermal Alkaline Treatment (HALT) of Foam Fractionation Concentrate Derived from PFAS-Contaminated Groundwater," *Environmental Science & Technology,* vol. 57, no. 44, pp. 17154–17165, 2023/11/07 2023, doi: 10.1021/acs.est.3c05140.

[26] O. Soker, S. Hao, B. G. Trewyn, C. P. Higgins, and T. J. Strathmann, "Application of Hydrothermal Alkaline Treatment to Spent Granular Activated Carbon: Destruction of Adsorbed PFASs and Adsorbent Regeneration," *Environmental science & technology letters,* vol. 10, no. 5, pp. 425–430, 2023, doi: 10.1021/acs.estlett.3c00161.

[27] C. Austin, A. L. Purohit, C. Thomsen, B. R. Pinkard, T. J. Strathmann, and I. V. Novosselov, "Hydrothermal Destruction and Defluorination of Trifluoroacetic Acid (TFA)," *Environmental Science & Technology,* vol. 58, no. 18, pp. 8076–8085, 2024/05/07 2024, doi: 10.1021/acs.est.3c09404.

[28] B. R. Pinkard, C. Austin, A. L. Purohit, J. Li, and I. V. Novosselov, "Destruction of PFAS in AFFF-impacted fire training pit water, with a continuous hydrothermal alkaline treatment reactor," *Chemosphere (Oxford),* vol. 314, p. 137681, 2023, doi: 10.1016/j.chemosphere.2022.137681.

[29] B. Pinkard *et al.*, "Degradation and Defluorination of Ultra Short-, Short-, and Long-Chain PFASs in High Total Dissolved Solids Solutions by Hydrothermal Alkaline Treatment□Closing the Fluorine Mass Balance," *ACS ES&T engineering,* vol. 4, no. 11, pp. 2810–2818, 2024, doi: 10.1021/acsestengg.4c00378.

[30] J. Li, B. R. Pinkard, S. Wang, and I. V. Novosselov, "Review: Hydrothermal treatment of per- and polyfluoroalkyl substances (PFAS)," *Chemosphere (Oxford),* vol. 307, no. Pt 2, p. 135888, 2022, doi: 10.1016/j.chemosphere.2022.135888.

[31] A. Loppinet-Serani, C. Aymonier, and F. Cansell, "Current and foreseeable applications of supercritical water for energy and the environment," *ChemSusChem,* vol. 1, no. 6, pp. 486–503, 2008, doi: https://doi.org/10.1002/cssc.200700167.

[32] M. Möller, P. Nilges, F. Harnisch, and U. Schröder, "Subcritical water as reaction environment: fundamentals of hydrothermal biomass transformation," *ChemSusChem,* vol. 4, no. 5, pp. 566–579, 2011, doi: https://doi.org/10.1002/cssc.201000341.

[33] A. L. Purohit *et al.*, "Design of a small-scale supercritical water oxidation reactor. Part II: Numerical modeling," *Industrial & Engineering Chemistry Research,* vol. 60, no. 30, pp. 11458–11469, Aug 2021, doi: https://doi.org/10.1021/acs.iecr.1c00932.

[34] M. Bermejo and M. Cocero, "Supercritical water oxidation: a technical review," *AIChE journal,* vol. 52, no. 11, pp. 3933–3951, 2006.

[35] J. Li, C. Austin, S. Moore, B. R. Pinkard, and I. V. Novosselov, "PFOS destruction in a continuous supercritical water oxidation reactor," *Chem. Eng. J.,* vol. 451, p. 139063, 2023/01/01/ 2023, doi: https://doi.org/10.1016/j.cej.2022.139063.

[36] C. Austin, J. Li, S. Moore, A. Purohit, B. R. Pinkard, and I. V. Novosselov, "Destruction and defluorination of PFAS matrix in continuous-flow supercritical water oxidation reactor: Effect of operating temperature," *Chemosphere,* p. 138358, 2023/03/09/ 2023, doi: https://doi.org/10.1016/j.chemosphere.2023.138358.

[37] J. T. McDonough *et al.*, "Validation of supercritical water oxidation to destroy perfluoroalkyl acids," *Remediation Journal,* vol. 32, no. 1-2, pp. 75–90, 2022.

[38] M. J. Krause *et al.*, "Supercritical Water Oxidation as an Innovative Technology for PFAS Destruction," *Journal of Environmental Engineering,* vol. 148, no. 2, p. 05021006, 2022.

[39] C. G. Scheitlin *et al.*, "Application of Supercritical Water Oxidation to Effectively Destroy Per- and Polyfluoroalkyl Substances in Aqueous Matrices," *ACS ES&T Water,* vol. 3, no. 8, pp. 2053–2062, 2023/08/11 2023, doi: 10.1021/acsestwater.2c00548.

[40] S. Rosansky *et al.*, "Field Demonstration of PFAS Destruction in Various Alcohol-Resistant AFFFs Using Supercritical Water Oxidation (SCWO)," *ACS ES&T Water,* vol. 4, no. 10, pp. 4486–4496, 2024/10/11 2024, doi: 10.1021/acsestwater.4c00499.

[41] J. Li, S. Wang, Y. Li, Z. Jiang, T. Xu, and Y. Zhang, "Supercritical water oxidation and process enhancement of nitrogen-containing organics and ammonia," (in English), *Water research,* ; Review vol. 185, p. 116222, 2020 Oct 15 (Epub 2020 Jul 2020, doi: https://doi.org/10.1016/j.watres.2020.116222.

[42] B. Yang, Q. Ma, X. Peng, Q. Wang, J. Huang, and J. Hao, "Enhanced denitrification of aniline and its derivatives by catalysts, anions, and co-fuels during supercritical water oxidation process," *The Journal of Supercritical Fluids,* vol. 203, p. 106077, 2023/12/01/ 2023, doi: https://doi.org/10.1016/j.supflu.2023.106077.

[43] B. Yang *et al.*, "Supercritical water oxidation of aniline, nitrobenzene, and indole: Effect of catalysts on nitrogen conversion mechanism," *The Journal of Supercritical Fluids,* vol. 188, p. 105680, 2022/09/01/ 2022, doi: https://doi.org/10.1016/j.supflu.2022.105680.

[44] C. Yang, D. Wang, Q. Tang, and J. Y. MacRae, "Removal of aniline from water by an Fe (II)-nano-Fe_3O_4@ PAC heterogeneous catalyst in a Fenton-like process," *Environmental Technology,* vol. 42, no. 4, pp. 545–557, 2021, doi: https://doi.org/10.1080/09593330.2019.1637462.

[45] H. Ma *et al.*, "Abatement of aniline in supercritical water using oxygen as the oxidant," *Industrial and Engineering Chemistry Research,* vol. 51, no. 28, pp. 9475–9482, Jul 18 2012, doi: https://doi.org/10.1021/ie3012819.

[46] J. Li, J. Hu, S. Wang, and D. Xu, "Reaction characteristics and process optimization of ammonia degradation by supercritical water co-oxidation with alcohol fuel," *Chemical Engineering Research and Design,* vol. 223, pp. 538–549, 2025, doi: https://doi.org/10.1016/j.cherd.2025.10.013.

[47] J. Li, C. Austin, S. Moore, N. Consolazio, S. Wang, and I. V. Novosselov, "Pyridine Degradation in Autogenic Supercritical Water Oxidation," *Journal of Environmental Chemical Engineering,* p. 121667, 2026/02/07/ 2026, doi: https://doi.org/10.1016/j.jece.2026.121667.

[48] J. Li, C. Austin, S. Moore, D. Xu, S. Wang, and I. V. Novosselov, "Transformation of aniline and nitroaromatics in autogenic supercritical water oxidation," *The Journal of Supercritical Fluids,* vol. 235, p. 107002, 2026/09/01/ 2026, doi: https://doi.org/10.1016/j.supflu.2026.107002.

[49] B. R. Pinkard, S. Shetty, D. Stritzinger, C. Bellona, and I. V. Novosselov, "Destruction of perfluorooctanesulfonate (PFOS) in a batch supercritical water oxidation reactor," *Chemosphere,* vol. 279, p. 130834, 2021/09/01/ 2021, doi: https://doi.org/10.1016/j.chemosphere.2021.130834.

[50] K. E. Carter and J. Farrell, "Oxidative destruction of perfluorooctane sulfonate using boron-doped diamond film electrodes," *Environmental science & technology,* vol. 42, no. 16, pp. 6111–6115, 2008.

[51] J. N. Meegoda, B. Bezerra de Souza, M. M. Casarini, and J. A. Kewalramani, "A Review of PFAS Destruction Technologies," in *International Journal of Environmental Research and Public Health* vol. 19, ed: MDPI, 2022.

[52] J. Li *et al.*, "Ammonia and organic carbon transformation in autogenic continuous flow supercritical water oxidation reactor," *Journal of Environmental Chemical Engineering,* vol. 13, no. 5, 2025/10// 2025, doi: 10.1016/j.jece.2025.117910.

[53] P. A. Marrone and G. T. Hong, "Corrosion control methods in supercritical water oxidation and gasification processes," *The Journal of Supercritical Fluids,* vol. 51, no. 2, pp. 83–103, 12// 2009, doi: http://dx.doi.org/10.1016/j.supflu.2009.08.001.

[54] T. Voisin *et al.*, "Solubility of inorganic salts in sub-and supercritical hydrothermal environment: application to SCWO processes," *The Journal of Supercritical Fluids,* vol. 120, pp. 18–31, 2017.

[55] J. Baldyga, "Turbulent mixer model with application to homogeneous, instantaneous chemical reactions," *Chemical Engineering Science,* vol. 44, no. 5, pp. 1175–1182, 1989, doi: 10.1016/0009-2509(89)87016-2.

[56] C. H. Oh, R. J. Kochan, T. R. Charlton, and A. L. Bourhis, "Articles Thermal-Hydraulic Modeling of Supercritical Water Oxidation of Ethanol," 1996. [Online]. Available: https://pubs.acs.org/sharingguidelines

[57] J. P. Serin, J. Mercadier, F. Marias, P. Cezac, and F. Cansell, "USE OF CFD FOR THE DESIGN OF INJECTORS FOR SUPERCRITICAL WATER OXIDATION."

[58] N. Zhou, A. Krishnan, F. Vogel, and W. A. Peters, "A computational model for supercritical water oxidation of organic toxic wastes," *Advances in Environmental Research,* vol. 4, no. 1, pp. 75–90, 2000/6// 2000, doi: 10.1016/S1093-0191(00)00011-3.

[59] H. R. Holgate, P. A. Webley, J. W. Tester, and R. K. Helling, "Carbon Monoxide Oxidation in Supercritical Water: The Effects of Heat Transfer and the Water-Gas Shift Reaction on Observed Kineticst," in "586 Energy & Fuels," 1992, vol. 6. [Online]. Available: https://pubs.acs.org/sharingguidelines

[60] S. C. E. Leung *et al.*, "Emerging technologies for PFOS/PFOA degradation and removal: A review," in *Science of the Total Environment* vol. 827, ed: Elsevier B.V., 2022.

[61] E. F. Houtz, C. P. Higgins, J. A. Field, and D. L. Sedlak, "Persistence of perfluoroalkyl acid precursors in AFFF-impacted groundwater and soil," *Environmental Science and Technology,* vol. 47, no. 15, pp. 8187–8195, 2013/8// 2013, doi: 10.1021/es4018877.

[62] M. Veciana *et al.*, "Electrochemical oxidation processes for PFAS removal from contaminated water and wastewater: fundamentals, gaps and opportunities towards practical implementation," in *Journal of Hazardous Materials* vol. 434, ed: Elsevier B.V., 2022.

[63] S. Wang *et al.*, "Photocatalytic degradation of perfluorooctanoic acid and perfluorooctane sulfonate in water: A critical review," *Chemical Engineering Journal,* vol. 328.

[64] J. Radjenovic and D. L. Sedlak, "Challenges and Opportunities for Electrochemical Processes as Next-Generation Technologies for the Treatment of Contaminated Water," in *Environmental Science and Technology* vol. 49, ed: American Chemical Society, 2015, pp. 11292–11302.

[65] B. Nzeribe and S. Mededovic, "Physico-Chemical Processes for the Treatment of Per- And Polyfluoroalkyl Substances (PFAS): A review," *Critical Reviews in Enviromental Sciences and Technology,* 2019.

[66] C. E. Schaefer, C. Andaya, A. Maizel, and C. P. Higgins, "Assessing Continued Electrochemical Treatment of Groundwater Impacted by Aqueous Film-Forming Foams," *Journal of Environmental Engineering,* vol. 145, no. 12, 2019.

[67] Q. Zhuo *et al.*, "Degradation of perfluorinated compounds on a boron-doped diamond electrode," *Electrochimica Acta,* vol. 77, pp. 17–22, 2012.

[68] S. Witt, N. Rancis, M. Ensch, and V. Maldonado, "Electrochemical destruction of 'forever chemicals': The right solution at the right time," *Electrochem. Soc. Interface,* 2020.

[69] S. Liang *et al.*, "Field demonstration of coupling ion-exchange resin with electrochemical oxidation for enhanced treatment of per- and polyfluoroalkyl substances (PFAS) in groundwater," *Chemical Engineering Journal Advances,* vol. 9, 2022/3// 2022, doi: 10.1016/j.ceja.2021.100216.

[70] R. K. Singh and N. Multari, "Rapid removal of poly- and perfluorinated compounds from investigation-derived waste (IDW) in a pilot-scale plasma reactor," *Environ. Sci. Technol.,* vol. 53, pp. 11375–11382, 2019.

[71] D. Palma, C. Richard, and M. Minella, "State of the art and perspectives about non-thermal plasma applications for the removal of PFAS in water," *Chemical Engineering Journal Advances,* vol. 10, pp. 100253–100253, 2022/5// 2022, doi: 10.1016/j.ceja.2022.100253.

[72] Y. Wang, "Sono2Photocatalytic Degradation of Organic Pollutants in Water," in "PROGRESS IN CHEMISTRY," 2008, vol. 20. [Online]. Available: http://www.cnki.net

[73] Y. Zhu *et al.*, "Adsorption and solid-phase photocatalytic degradation of perfluorooctane sulfonate in water using gallium-doped carbon-modified titanate nanotubes," *Chemical Engineering Journal,* vol. 421, pp. 129676–129676, 2021/10// 2021, doi: 10.1016/J.CEJ.2021.129676.

[74] L. Rodriguez-Freire, R. Balachandran, R. Sierra-Alvarez, and M. Keswani, "Effect of sound frequency and initial concentration on the sonochemical degradation of perfluorooctane sulfonate (PFOS)," *Journal of Hazardous Materials,* vol. 300, pp. 662–669, 2015/12// 2015, doi: 10.1016/J.JHAZMAT.2015.07.077.

[75] R. James Wood, T. Sidnell, I. Ross, J. McDonough, J. Lee, and M. J. Bussemaker, "Ultrasonic degradation of perfluorooctane sulfonic acid (PFOS) correlated with sonochemical and sonoluminescence characterisation," *Ultrasonics Sonochemistry,* vol. 68, pp. 105196–105196, 2020/11// 2020, doi: 10.1016/J.ULTSONCH.2020.105196.

[76] B. G. Loganathan, K. S. Sajwan, E. Sinclair, K. Senthil Kumar, and K. Kannan, "Perfluoroalkyl sulfonates and perfluorocarboxylates in two wastewater treatment facilities in Kentucky and Georgia," *Water Research,* vol. 41, no. 20, pp. 4611–4620, 2007/12// 2007, doi: 10.1016/j.watres.2007.06.045.

[77] J. Wang *et al.*, "Critical Review of Thermal Decomposition of Per- and Polyfluoroalkyl Substances: Mechanisms and Implications for Thermal Treatment Processes," in *Environmental Science and Technology* vol. 56, ed: American Chemical Society, 2022, pp. 5355–5370.

[78] S. J. Moore, B. R. Pinkard, A. L. Purohit, J. C. Kramlich, P. G. Reinhall, and I. V. Novosselov, "Design of a Small-Scale Supercritical Water Oxidation Reactor. Part I: Experimental Characterization," *Industrial and Engineering Chemistry Research,* vol. 60, no. 30, pp. 11450–11457, 2021/8// 2021, doi: 10.1021/acs.iecr.1c00900.

[79] C. Berg *et al.*, "Developing innovative treatment technologies for PFAS-containing wastes," *Journal of the Air & Waste Management Association,* vol. 72, no. 6, pp. 540–555, 2022/6// 2022, doi: 10.1080/10962247.2021.2000903.

[80] Z. Jiang, Y. Li, S. Wang, C. Cui, C. Yang, and J. Li, "Review on mechanisms and kinetics for supercritical water oxidation processes," in *Applied Sciences (Switzerland)* vol. 10, ed: MDPI AG, 2020.

[81] J. Li, A. Kazakov, M. Chaos, and F. L. Dryer, "Chemical Kinetics of Ethanol Oxidation."

[82] K. B. Fackler, M. F. Karalus, I. V. Novosselov, J. C. Kramlich, and P. C. Malte, "Experimental and numerical study of NOx formation from the lean premixed combustion of CH4 mixed with CO2 and N 2," *Journal of Engineering for Gas Turbines and Power,* vol. 133, no. 12, 2011, doi: 10.1115/1.4004127.

[83] I. V. Novosselov and P. C. Malte, "Development and application of an eight-step global mechanism for CFD and CRN simulations of lean-premixed combustors," *Journal of Engineering for Gas Turbines and Power,* vol. 130, no. 2, p. 021502, 2008.

[84] A. L. Purohit, P. C. Malte, I. V. Novosselov, and J. C. Kramlich, "Role of NNH in Low-NOx Hydrogen Combustion."

[85] D. Mateos, J. R. Portela, J. Mercadier, F. Marias, C. Marraud, and F. Cansell, "New approach for kinetic parameters determination for hydrothermal oxidation reaction," *Journal of Supercritical Fluids,* vol. 34, no. 1, pp. 63–70, 2005/5// 2005, doi: 10.1016/j.supflu.2004.10.013.

[86] G. Anitescu, Z. Zhang, and L. L. Tavlarides, "A kinetic study of methanol oxidation in supercritical water," *Industrial and Engineering Chemistry Research,* vol. 38, no. 6, pp. 2231–2237, 1999, doi: 10.1021/ie980610w.

[87] P. A. Webley and J. W. Tester, "Articles Fundamental Kinetics of Methane Oxidation in Supercritical Water," in "Energy & Fuels," 1991, vol. 5. [Online]. Available: https://pubs.acs.org/sharingguidelines

[88] E. E. Brock, Y. Oshima, and P. Savage, "Kinetics and Mechanism of Methanol Oxidation in Supercritical Water," *Journal of Physical Chemistry,* 1996.

[89] B. Pinkard, J. Kramlich, P. Reinhall, and I. Novosselov, "Gasification Kinetics in Continuous Supercritical Water Reactors," in *Advanced Supercritical Fluids Technologies*: IntechOpen, 2020.

[90] C. K. Westbrook and F. L. Dryer, "Simplified Reaction Mechanisms for the Oxidation of Hydrocarbon Fuels in Flames," *Combustion Science and Technology,* vol. 27, no. 1-2, pp. 31–43, 1981/12// 1981, doi: 10.1080/00102208108946970.

[91] A. L. Purohit, A. Nalbandyan, P. C. Malte, and I. V. Novosselov, "NNH mechanism in low-NOx hydrogen combustion: Experimental and numerical analysis of formation pathways," *Fuel,* vol. 292, p. 120186, 2021/05/15/ 2021, doi: https://doi.org/10.1016/j.fuel.2021.120186.

[92] R. K. Chakrabarty, I. V. Novosselov, N. D. Beres, H. Moosmüller, C. M. Sorensen, and C. B. Stipe, "Trapping and aerogelation of nanoparticles in negative gravity," *Ambient Observations of Aerosols, Novel Aerosol Structures,* p. 100, 2014.

[93] R. K. Chakrabarty, H. Moosmüller, M. A. Garro, and C. B. Stipe, "Observation of superaggregates from a reversed gravity low-sooting flame," *Aerosol Science and Technology,* vol. 46, no. 1, pp. i–iii, 2012.

[94] R. K. Chakrabarty, I. V. Novosselov, N. D. Beres, H. Moosmüller, C. M. Sorensen, and C. B. Stipe, "Trapping and aerogelation of nanoparticles in negative gravity

hydrocarbon flames," *Applied Physics Letters,* vol. 104, no. 24, p. 243103, 2014/06/16 2014, doi: 10.1063/1.4884057.

[95] C. B. Stipe, B. S. Higgins, D. Lucas, C. P. Koshland, and R. F. Sawyer, "Inverted co-flow diffusion flame for producing soot," *Review of scientific instruments,* vol. 76, no. 2, p. 023908, 2005.

[96] J. Davis, K. Tiwari, and I. Novosselov, "Soot morphology and nanostructure in complex flame flow patterns via secondary particle surface growth," *Fuel,* vol. 245, pp. 447–457, 2019/06/01/ 2019, doi: https://doi.org/10.1016/j.fuel.2019.02.058.

[97] J. Davis, E. Molnar, and I. Novosselov, "Nanostructure transition of young soot aggregates to mature soot aggregates in diluted diffusion flames," *Carbon,* 2019.

[98] G. Mahamuni *et al.*, "Excitation–Emission Matrix Spectroscopy for Analysis of Chemical Composition of Combustion Generated Particulate Matter," *Environmental Science & Technology,* vol. 54, no. 13, pp. 8198–8209, 2020/07/07 2020, doi: 10.1021/acs.est.0c01110.

[99] C. P. West *et al.*, "Molecular Composition and the Optical Properties of Brown Carbon Generated by the Ethane Flame," *ACS Earth and Space Chemistry,* vol. 4, no. 7, pp. 1090–1103, 2020/07/16 2020, doi: 10.1021/acsearthspacechem.0c00095.

[100] J. Schanzenbächer, J. D. Taylor, and J. W. Tester, "Ethanol oxidation and hydrolysis rates in supercritical water," *The Journal of Supercritical Fluids,* vol. 22, no. 2, pp. 139–147, 2002/2// 2002, doi: 10.1016/S0896-8446(01)00119-X.

[101] S. Bai, "SCWO experiment report - University of Washington," 2024.

[102] Novosselov, "Schematic of UW SCWO Reactor," ed.

[103] A. Inc, "ANSYS Fluent 12.0 Theory Guide - 1.2 Continuity and Momentum Equations."

[104] A. Inc, "Shear-Stress Transport (SST) k-w model - AFS ENEA."

[105] T. National Institute of Standards and, *National Institute of Standards and Technology (NIST) Chemistry Webbook SRD 69 - Thermophysical Properties of Fluid Systems - https://webbook.nist.gov/chemistry/fluid*. 2026.

[106] A. Inc, "AFS ENEA - 8.4.3 Defining the Viscosity Using Kinetic Theory," 2025.

[107] I. Novosselov, P. Malte, S. Yuan, R. Srinivasan, and J. Lee, "Chemical reactor network application to emissions prediction for industial dle gas turbine," in *ASME turbo expo 2006: Power for land, sea, and air*, 2006: American Society of Mechanical Engineers, pp. 221–235.

[108] A. Kaluri, P. Malte, and I. Novosselov, "Real-time prediction of lean blowout using chemical reactor network," *Fuel,* vol. 234, pp. 797–808, 2018/12/15/ 2018, doi: https://doi.org/10.1016/j.fuel.2018.07.065.

[109] S. Gupta, P. Malte, S. L. Brunton, and I. Novosselov, "Prevention of lean flame blowout using a predictive chemical reactor network control," *Fuel,* vol. 236, pp. 583–588, 2019.

[110] M. F. Karalus, K. B. Fackler, I. V. Novosselov, J. C. Kramlich, and P. C. Malte, "A skeletal mechanism for the reactive flow simulation of methane combustion," presented at the ASME Turbo Expo 2013: Turbine Technical Conference and Exposition, San Antonio, Texas, USA, June 3–7, 2013.

[111] Y. Guan and I. Novosselov, "Damkohler Number Analysis in Lean Blow-Out of Toroidal Jet Stirred Reactor," *Journal of Engineering for Gas Turbines and Power,* vol. 140, no. 10, p. 104501, 2018.

[112] B. B. Bastl, Marek; Egermaier, Jiří; Michálková, Kristýna; Turnerová, Eva, "Isogeometric analysis for turbulent flowTurbulence Modeling for CFD," 2016.

[113] A. Inc, "Ansys Fluent 12.0 Theory Guide - 26.2.1. First-Order Accuracy vs. Second-Order Accuracy."

[114] A. Inc, "ANSYS Fluent 12.0 Theory Guide - 18.4.3 Pressure-Velocity Coupling."

[115] A. Inc, "ANSYS Fluent 12.0 Theory Guide - Composition-Dependent Density for Multicomponent Mixtures," 2025.

Appendix

7.1. PSR model setup

The rate calculation was on a molar basis (mol/L-s). The mol and mass fractions of the reacting species were first converted to molar concentrations using the mixture density and species molecular weight.

$$C = Y \cdot \frac{\rho_{mixture}}{M_w}$$

The molar concentration C was then used to calculate the rates r_1 and r_2 on the molar concentration basis. The r_1 and r_2 were then converted back to mass fraction basis (1/s) and used as the input for the rate of change of the species mass fractions, $\frac{dY}{dt}$.

Based on the stoichiometry and the molecular weight of each species in the reaction, the rate of change for the species concentrations were modeled to be a set of ordinary differential equations (ODEs) given by

$$\frac{dY_{C_2H_5OH}}{dt} = -r1$$

$$\frac{dY_{O_2}}{dt} = -1.39r_1 - 0.57r_2$$

$$\frac{dY_{CO}}{dt} = 1.22r_1 - r_2$$

$$\frac{dY_{CO_2}}{dt} = 1.57r_2$$

$$\frac{dY_{H_2O}}{dt} = 1.173\, r_1$$

The following figure shows the agreement between the temperature prediction of the PSR model and the experiment after modeling the effects of heat transfer.

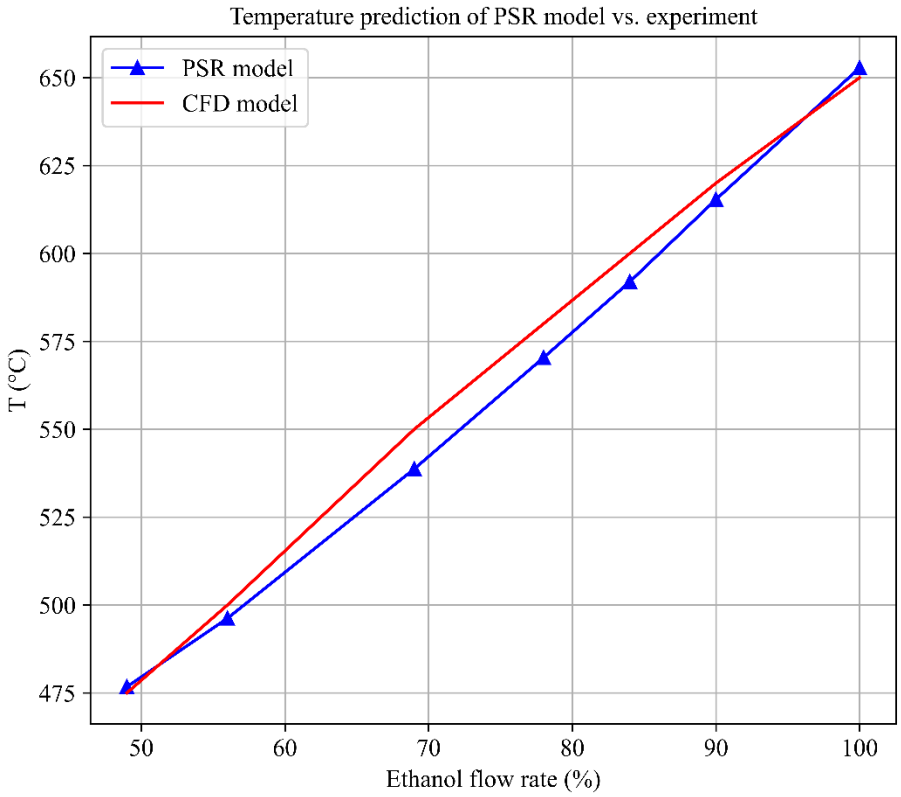

Figure A. 1.Temperature prediction of PSR model vs. experiment

7.2. Meshing details

The domain was discretized/meshed into structured quadrilateral elements. The mesh size at the reactor head and the reaction zones are at ~0.1 mm, with variations of the size given by inflation as domain reaches the centerline axis and the shear layers where the species were expected to mix during the reacting flow. The smallest elements at the expected shear layer and the center of the inlets are 0.015 mm, with gradually increasing size as they further go laterally.

The fine mesh structure of ~0.1 mm goes from the reactor head to approximately 45% of the reactor length (~160 mm) to well define the fluid dynamics in the reaction zone. As the domain goes further downstream from ~160 mm, the mesh gradually grows in size to become 0.25 mm. The downstream elements are structured rectangularly and uniform. Figure 22 and 23 shows the mesh model at the reactor head and near the inlets.

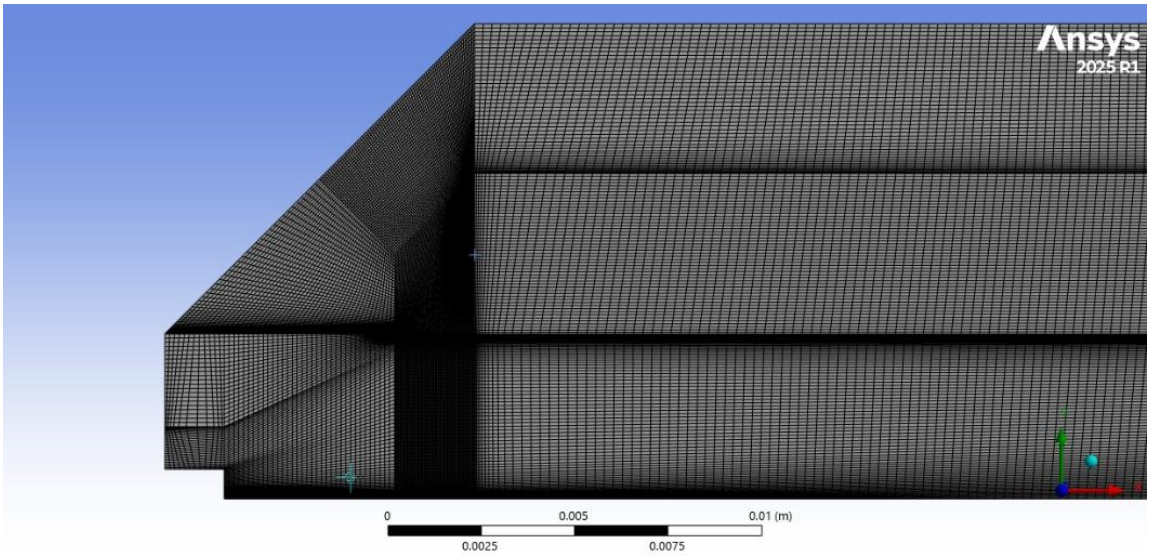

Figure A. 2. Meshing at the reactor head and near the reaction zone.

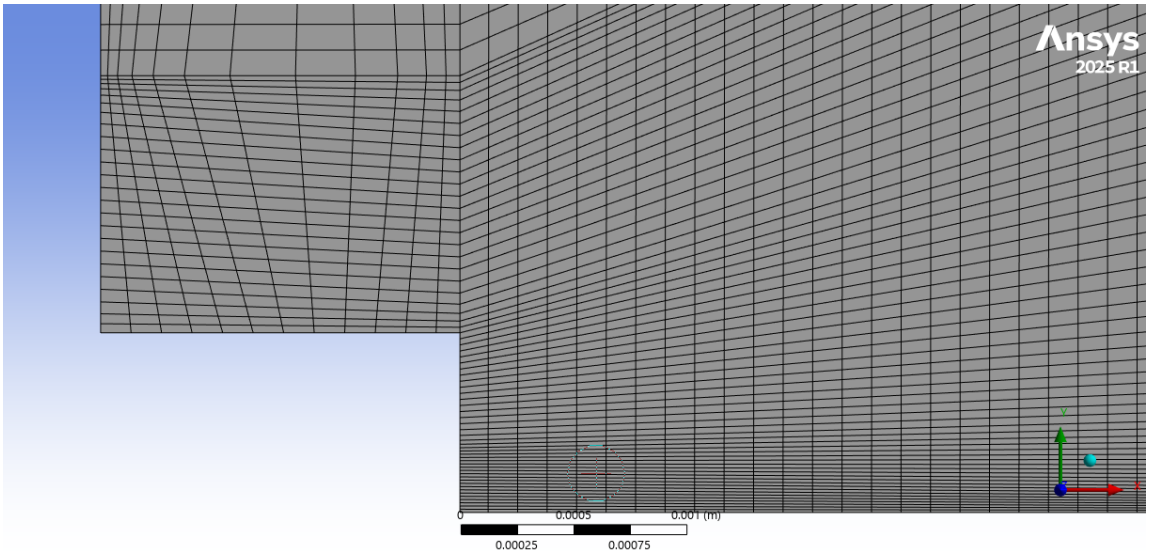

Figure A. 3. Mesh sizing at the inlets and the reactor head, showing finer mesh size at the expected reaction layer.

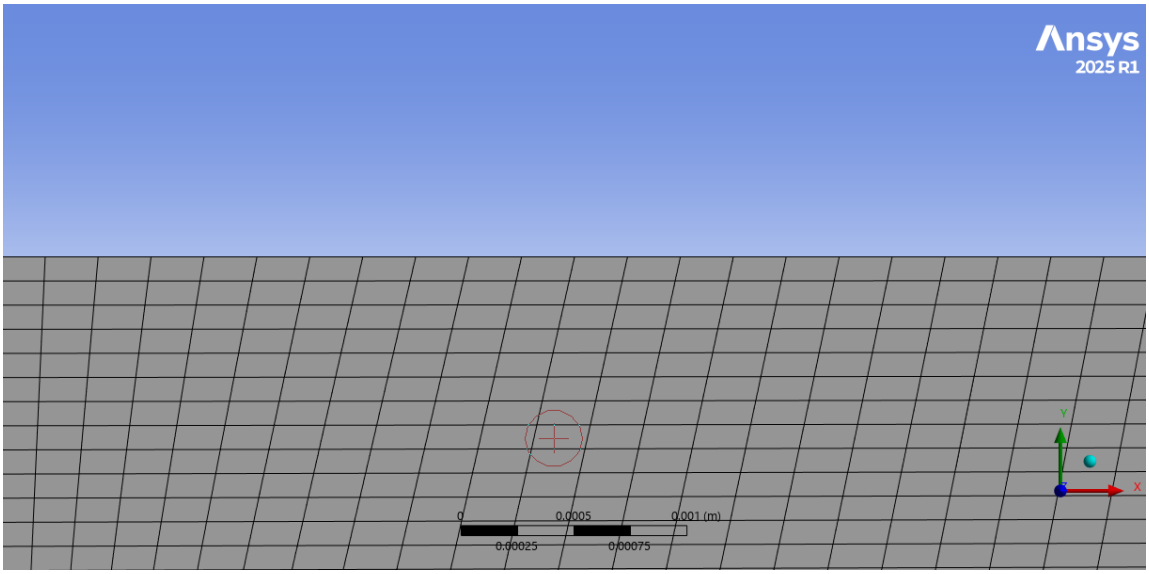

Figure A. 4. Mesh sizing in the wall boundary

Where Δs is the maximum element width in the wall boundary. The calculation of Δs with the expected average bulk velocity of 0.005 m/s, the water-dominated supercritical mixture density of ~700-800 kg/m^3 and the target y+ of 1.0 yielded Δs = ~0.18 mm.

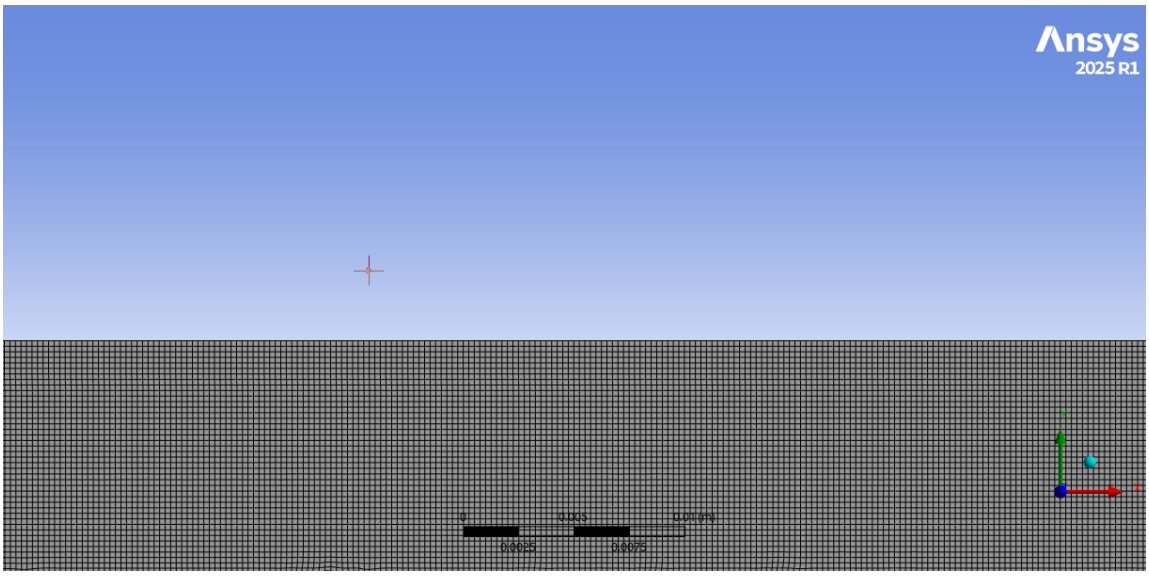

Figure A. 5. Mesh sizing at the downstream.

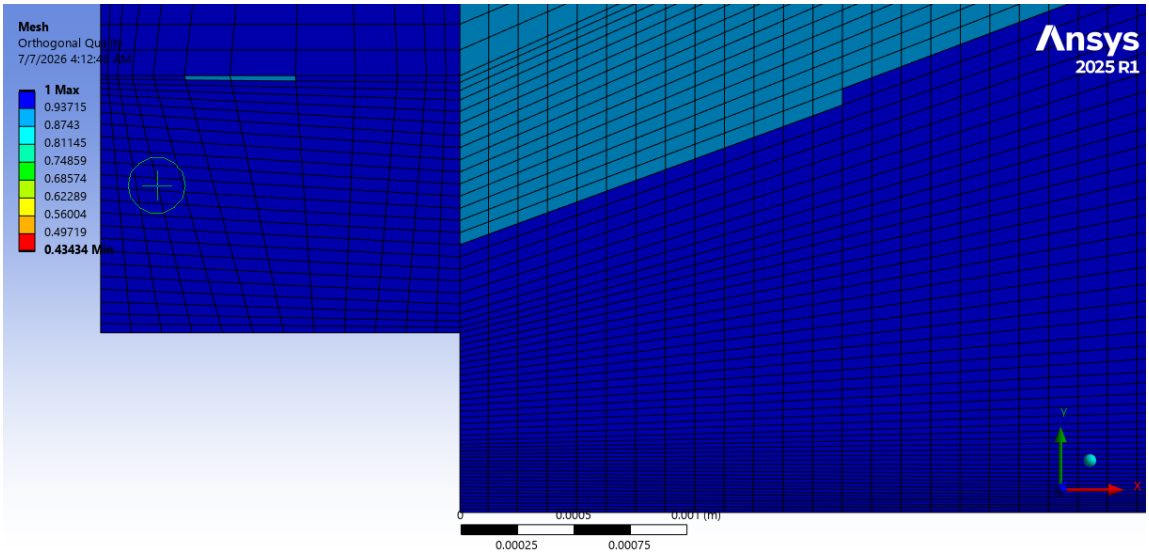

Figure A. 6. Element quality (shown at the inlets and near the reaction zone).

7.3. Mesh refinement

Mesh refinement was conducted to determine the resolution needed to achieve convergence of CO within the domain. The following figure shows that coarser mesh resolution was unable to reach the convergence on the distribution of CO.

Case	CO Contour
(1)	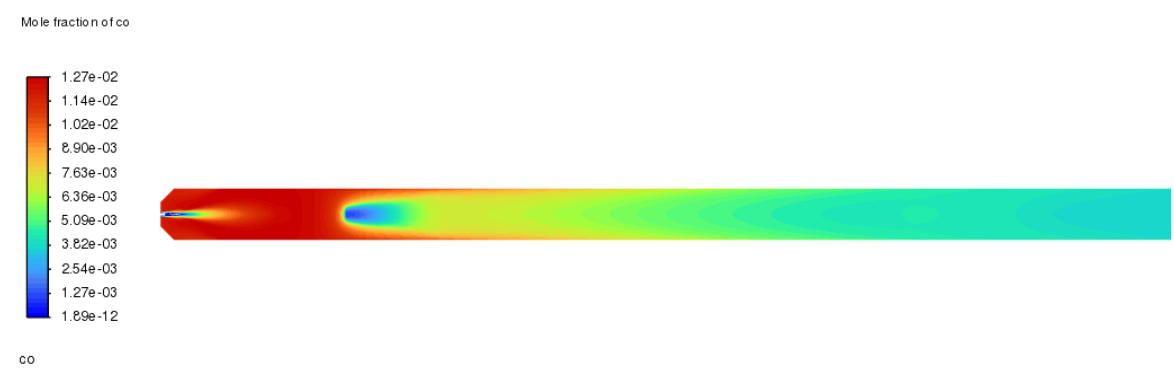
(2)	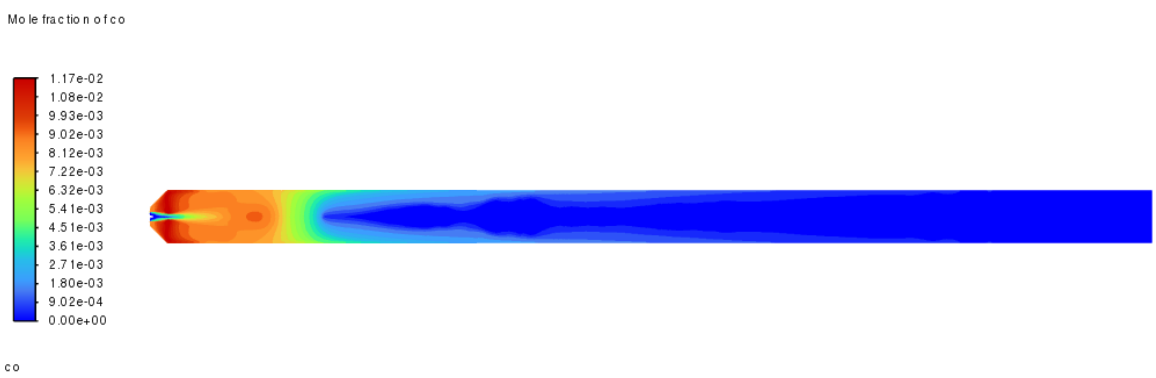
(3)	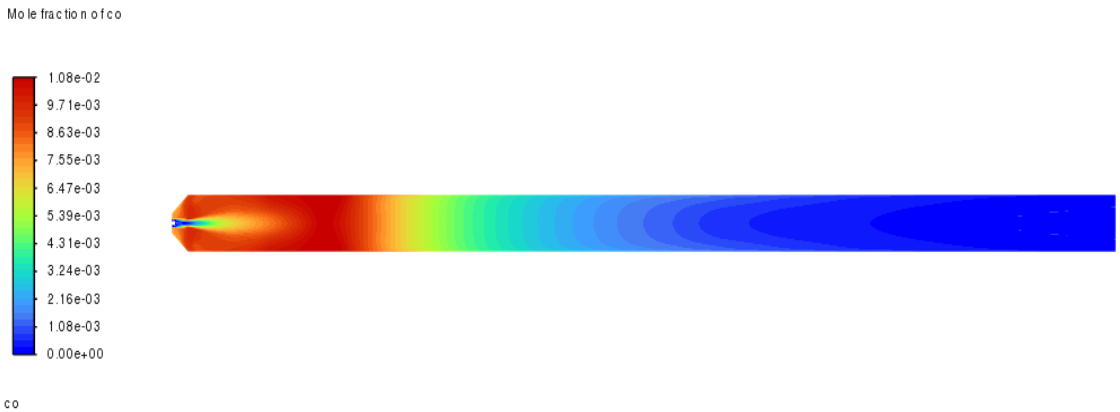

Figure A. 7. Mesh refinement for the 49% flow rate case

7.4. Governing equations – detailed

7.4.1. Governing equations – continuity and momentum equations

The mass conservation equation is given by [103]

$$\frac{\partial \rho}{\partial t} + \nabla \cdot (\rho \vec{u}) = S_m$$

The source S_m is the mass added to the continuous phase from the dispersed second phase. The first term represents the rate of mass change in a fluid element against time, and the second term represents the mass flow rate of the fluid coming in and out of the element (volume dilatation). For 2D axisymmetric geometries, the continuity equation is given by

$$\frac{\partial \rho}{\partial t} + \frac{\partial}{\partial x}(\rho u_x) + \frac{\partial}{\partial r}(\rho u_r) + \frac{\rho v_r}{r} = S_m$$

Where u denotes the velocity, x denotes the axial direction, r denotes the radial direction, and z is the swirl direction.

Based on the Navier-Stokes (NS) conservation of momentum equation, the momentum conservation for a 2D axisymmetric fluid flow in the axial and radial directions respectively are defined [103] as:

$$\frac{\partial}{\partial t}(\rho u_x) + \frac{\partial}{\partial x}(r\rho u_x u_x) + \frac{1}{r}(r\rho u_r u_x) = -\frac{\partial p}{\partial x} + \frac{1}{r}\frac{\partial}{\partial x}\left[r\mu\left(2\frac{\partial u_x}{\partial x} - \frac{2}{3}\nabla \cdot \vec{u}\right)\right] + \frac{1}{r}\frac{\partial}{\partial r}\left[r\mu\left(\frac{\partial u_x}{\partial r} + \frac{\partial u_r}{\partial x}\right)\right] + F_x$$

(x-momentum)

And

$$\frac{\partial}{\partial t}(\rho u_r) + \frac{1}{r}\frac{\partial}{\partial x}(r\rho u_x u_r) + \frac{1}{r}\frac{\partial}{\partial r}(r\rho u_r u_r) = -\frac{\partial p}{\partial r} + \frac{1}{r}\frac{\partial}{\partial x}\left[r\mu\left(\frac{\partial u_r}{\partial x} + \frac{\partial u_x}{\partial x}\right)\right]$$

$$+\frac{1}{r}\frac{\partial}{\partial r}\left[r\mu\left(2\frac{\partial u_r}{\partial r} - \frac{2}{3}(\nabla\cdot\vec{u})\right)\right] - 2\mu\frac{u_r}{r^2} + \frac{2}{3}\frac{\mu}{r}(\nabla\cdot\vec{u}) + \rho\frac{u_z^2}{r}\ F_r$$

(radial momentum),

Where:

$$\nabla\cdot\vec{u} = \frac{\partial u_x}{\partial x} + \frac{\partial u_r}{\partial r} + \frac{u_r}{r}$$

The momentum equation has multiple elements. The $\frac{\partial}{\partial t}$ term – the transient term, represents the rate of change of the momentum with respect to time. The spatial derivatives of the $\rho\vec{v}\vec{v}$ terms represent the change of momentum as the fluid goes along the space. In lieu of Newton's second law, the momentum change (force) depends on the forces caused by three modeled forces:

(1) The pressure gradient acting normal on the fluid element (the first term on the right-hand side),

(2) The shear forces acting parallel on the surface of the fluid element, which is represented by the stress tensor (the second and third terms on the right-hand side), and

(3) The body forces due to the weight of the fluid element (the last term on the right-hand side).

The momentum, continuity, energy, and species transport equations can be represented as a general scalar transport equation. The continuity and momentum equations are discretized

for the spatially discrete CFD domain using the first-order upwind scheme. Generalizing the velocity into a scalar quantity ϕ, the discretization of the equations [113] is given by

$$\frac{\partial \rho \phi}{\partial t}\,\partial x \partial y \partial z + \sum_{f}^{Nfaces} \rho_f \overrightarrow{u_f}\,\phi_f \cdot \vec{A}_{face} = \sum_{f}^{Nfaces} \Gamma_\phi \nabla \phi_f \cdot \vec{A}_{face} + S_\phi \partial x \partial y \partial z$$

The values of the scalar quantity ϕ (such as velocity) on each face of the element are predicted using the upstream value of $\phi_{upstream}$, upwind relative to the direction of the normal velocity. In the first-order scheme, quantities at the cell faces are determined by assuming that the cell-centre values of any field variable represent a cell-average value and hold throughout the entire cell so that $\phi_f = \phi_{center}$.

When the mesh structure is modeled as quadrilaterals and the flow is aligned with the mesh faces, the use of first-order upwind is acceptable and yields better convergence than the second-order scheme [113].

The interpolation for the pressure gradient term in the momentum equation is carried out using a coupled algorithm. The coupled algorithm solves the momentum and pressure-based continuity equations together, compared to the pressure-based segregated algorithms (SIMPLE, PISEC) which solve the momentum equation and pressure correction equations separately [114]. The coupled algorithm had proven to be able to properly accommodate high gradients in density [33, 83, 91] which is the occurrence in the supercritical system and is able to yield a gradually faster convergence than the segregated algorithms. For this reason, the coupled algorithm was used as the pressure coupling.

7.4.2. Governing equation - energy equation

The energy equation was incorporated to model the thermodynamics of the reaction, such as chemical heat generation, convective heat transfer, and the resulting buoyancy due to

density gradients. The general form of the energy equation used in this model was derived from the NS equation and given by

$$\frac{\partial}{\partial t}(\rho E) + \nabla \cdot \left(\vec{u}(\rho E + p)\right) = \nabla \cdot \left(k_{eff} \nabla T\right) + S_h$$

The density and k_{eff} (effective thermal conductivity) are shared by the phases. The source term, S_h, contains contributions from radiation, as well as any other volumetric heat sources. The energy equation in this model was also discretized using first order upwind.

7.4.3. Species transport

Similarly, the species transport equation follows the general scalar transport equation and follows the general form:

$$\frac{\partial}{\partial t}(\rho Y_i) + \nabla \cdot (\rho u Y_i) = -\nabla \cdot J_i + R_i + S_i$$

The density and k_{eff} (effective thermal conductivity) are shared by the phases. The source term, S_h, contains contributions from radiation, as well as any other volumetric heat sources.

J_i is the mass diffusion. R_i is the net rate of production of species *i* by chemical reaction. S_i is the rate of creation from the dispersed phase. The species transport equation was discretized and solved for each species in this model (ethanol, oxygen, carbon monoxide, carbon dioxide, nitrogen, and water).

The discretization predicts the local mass fraction of each species, Y_i , through the solution of a convection-diffusion equation for the *i*th species. The turbulent diffusion calculation is proportional to the turbulent diffusivity and the mixture viscosity, and reciprocal

to the turbulent Schmidt number. Meaning, as the flow becomes more turbulent, the distribution of the species within the reactor will be more diffused. The energy equation in this model was also discretized using first-order upwind.

$$\mu(T) = 2.67 * 10^{-6} \sqrt{\left(\frac{M_\omega T}{\sigma^2 \Omega}\right)}$$

$$k(T) = \frac{15}{4}\left(\frac{R}{M_w}\right)\mu\left(\frac{4}{15} * \frac{c_p M_w}{R} + \frac{1}{3}\right)$$

Where M_w is the molecular weight and σ and Ω are the Lennard-Jones kinetic parameters. The coupling between μ and k provided a consistent definition of the two properties. The use of Lennard-Jones kinetic theory model for CO and C_2H_5OH was considered appropriate given the unavailability of their thermophysical data for temperatures above 220°C and had proven to give a reasonable agreement with experiment results [1] and was computationally stable.

The properties of the rest of the species (C_2H_5OH, N_2, O_2, CO_2) were observed to be monotonically linear with increase in temperature and are available in the operating temperature range of 300-1100°C and 25 MPa. The polynomial coefficients for their properties are given in Tables 3.13-3.16.

The mixture density was modeled as volume-weighted mixing law. The mixture density was obtained from the individual contributions of the species defined by their volume fractions (mass fractions divided by their individual densities) [115].

$$\rho_{mixture} = \frac{1}{\sum_i \frac{Y_i}{\rho_i}}$$

The specific heat of the mixture was modeled using the specific heat mixing law.

$$c_{p\,mixture} = \sum_i Y_i c_{p,i}$$

The thermal conductivity of the mixture was modeled as ideal-gas mixing law. The mixture thermal conductivity was computed based on kinetic theory as

$$k_{mixture} = \sum_i^N \frac{X_i k_i}{\sum_j X_j \phi_{ij}}$$

Where ϕ_{ij} denotes the interaction factor between species i (the reference species) and the other interacting species j, and X is the mol fraction of each species.

Similarly, the viscosity of the mixture was modeled as mass weighted mixing law. The mixture viscosity was calculated based on kinetic theory as

$$\mu = \sum_i^N \frac{X_i \mu_i}{\sum_j X_j \phi_{ij}}$$

$$\phi_{ij} = \frac{\left[1 + \left(\frac{\mu_i}{\mu_j}\right)^{\frac{1}{2}} \left(\frac{M_{w,j}}{M_{w,i}}\right)^{\frac{1}{4}}\right]^2}{\left[8\left(1 + \frac{M_{w,i}}{M_{w,j}}\right)\right]^{\frac{1}{2}}}$$

Where M_w denotes the molecular weight of the individual species.

7.5. Thermophysical properties – detail

The following tables provide the polynomial coefficients of the thermophysical properties for each species. The coefficients were obtained from polynomial fits of the NIST thermophysical properties, and from reference [1].

Table A. 1. Density polynomial coefficients

Species	Temperature range (°C)	a	b	c	d	e	F	g
C_2H_5OH	300-1100	-1.11E+03	1.47E+01	-3.84E-02	3.80E-05	-1.30E-08	-	-
O_2	300-1100	1.07E+03	-4.09E+00	6.95E-03	-5.45E-06	1.61E-09	-	-
N_2	300-1100	6.41E+02	-1.73E+00	1.50E-03	-	-	-	-
CO	300-1100	6.57E+02	-1.82E+00	1.62E-03	-	-	-	-
CO_2	300-1100	5250.33	-25.52	0.048	-4.05E-05	1.25E-08	-	-
H_2O	300-670	-6.29E+04	9.19E+02	-5.43E+00	1.69E-02	-2.90E-05	2.62E-08	-9.74E-12
	670-1200	2.38E+04	-1.19E+02	2.46E-01	-2.66E-04	1.60E-07	-5.03E-11	6.51E-15

Table A. 2. Specific heat polynomial coefficients [1]

Species	Temperature range (°C)	a	b	c	d	E
C_2H_5OH	300-591	-7.32E+02	1.16E+01	-3.83E-03	3.80E-05	-1.30E-08
	591-1100	1.75E+04	-3.21E+01	1.81E-02	-	-
O_2	300-1100	2.81E+03	-9.54E+00	1.89E-02	-1.60E-05	5.00E-09
N_2	300-1100	3062.19	-11.2076	0.0245793	-2.42E-05	9.03E-09
CO_2	300-364	6.02E+04	-5.51E+02	1.72E+00	-1.77E-03	-
	364-1100	1.44E+04	-6.70E+01	1.25E-01	-1.03E-04	3.11E-08
H_2O	249.85-326.85	6.85E+04	-2.41E+02	2.28E-01	-	-
	326.85-356.85	6.06E+05	-2.00E+03	1.67E+00	-	-
	356.85-376.85	8.92E+06	-2.82E+04	2.23E+01	-	-
	376.85-384.85	3.35E+08	-1.03E+06	7.92E+02	-	-
	384.85-386.85	-1.01E+08	3.23E+05	-2.57E+02	-	-
	386.85-394.85	2.61E+08	-7.82E+05	5.86E+02	-	-
	394.85-426.85	4.94E+06	-1.41E+04	1.01E+01	-	-
	426.85-576.85	1.18E+06	-4.37E+03	5.40E+00	-2.23E-03	-

Table A. 3. Thermal conductivity polynomial coefficients

Species	Temperature range (°C)	a	B	c	d	e	f	G	h	i
O_2	300-1100	0.0269784	3.82E-05	9.61E-09	-	-	-	-	-	-
N_2	300-1100	0.0692909	-0.000247	7.04E-07	-7.51E-10	2.99E-13	-	-	-	-
CO_2	300-1100	1.256694	-0.008429	2.28E-05	-3.01E-08	1.95E-11	-4.98E-15			
H_2O	300-346.85	-1.69E-20	5.85E-17	-8.83E-14	7.54E-11	-3.98E-08	1.33E-05	-2.77E-03	3.31E-01	-1.72E+01
	346.85-426.85	5.74E-15	-2.27E-11	3.50E-08	-2.29E-05	-3.56E-04	1.04E+01	-6.78E+03	1.91E+06	-2.10E+08
	426.85-1100	4.74E-21	-3.50E-17	1.13E-13	-2.08E-10	2.38E-07	-1.75E-04	7.98E-02	-2.08E+01	2.37E+03

Table A. 4. Viscosity polynomial coefficients

Species	Temperature range (°C)	a	b	c	D	e	f	g
O_2	300-1100	1.85E-05	3.30E-08	-	-	-	-	-
N_2	300-1100	3.76E-05	-1.20E-07	3.62E-10	-3.89E-13	1.54E-16	-	-
CO_2	300-1100	1.256694	-0.008429	2.28E-05	-3.01E-08	1.95E-11	-4.98E-15	-
H_2O	300-346.85	1.06E-17	-3.13E-14	3.83E-11	-2.49E-08	9.09E-06	-1.77E-03	1.44E-01
	346.85-426.85	1.38E-14	-5.53E-11	9.19E-08	-8.15E-05	4.06E-02	-1.08E+01	1.19E+03
	426.85-1100	2.80E-16	-1.06E-12	1.49E-09	-8.88E-07	2.16E-04	-	-

Table A. 5. Molecular weights of the species

Species	Molecular weight, M_w (kg/kmol)
C_2H_5OH	46.07
O_2	31.99
N_2	28.01
CO	28.01
CO_2	44.01
H_2O	18.01

The following figures show the thermophysical behavior of water and carbon monoxide at the supercritical phase.

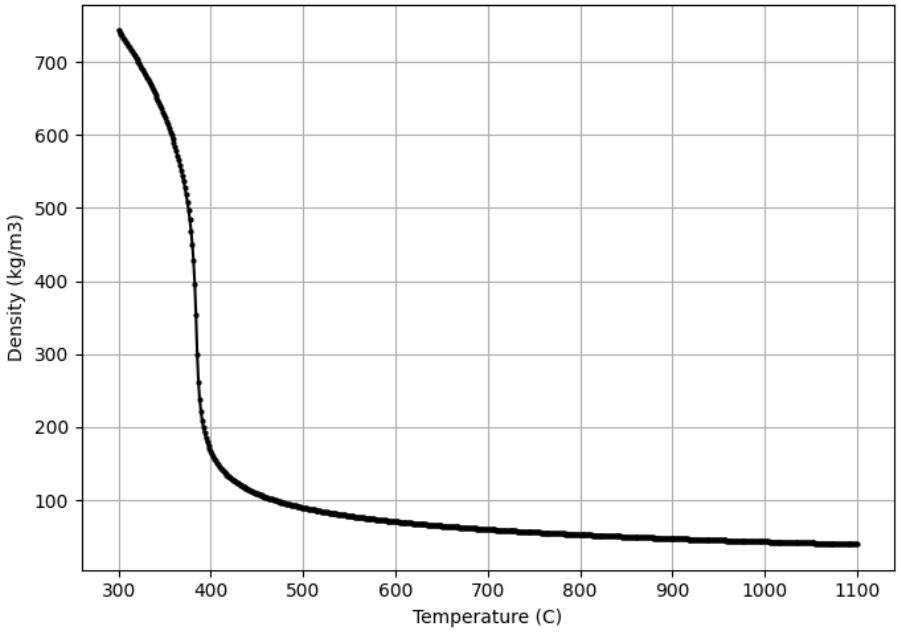

Figure A. 8. Density of supercritical water at 25 MPa (NIST, 2026)

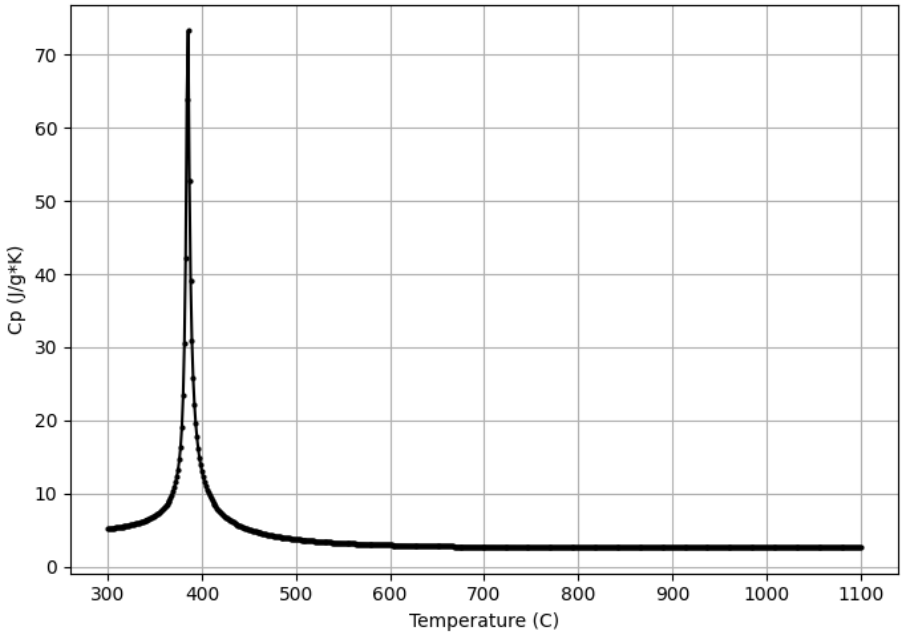

Figure A. 9. Specific heat of scH2O at 25 MPa (NIST, 2026)

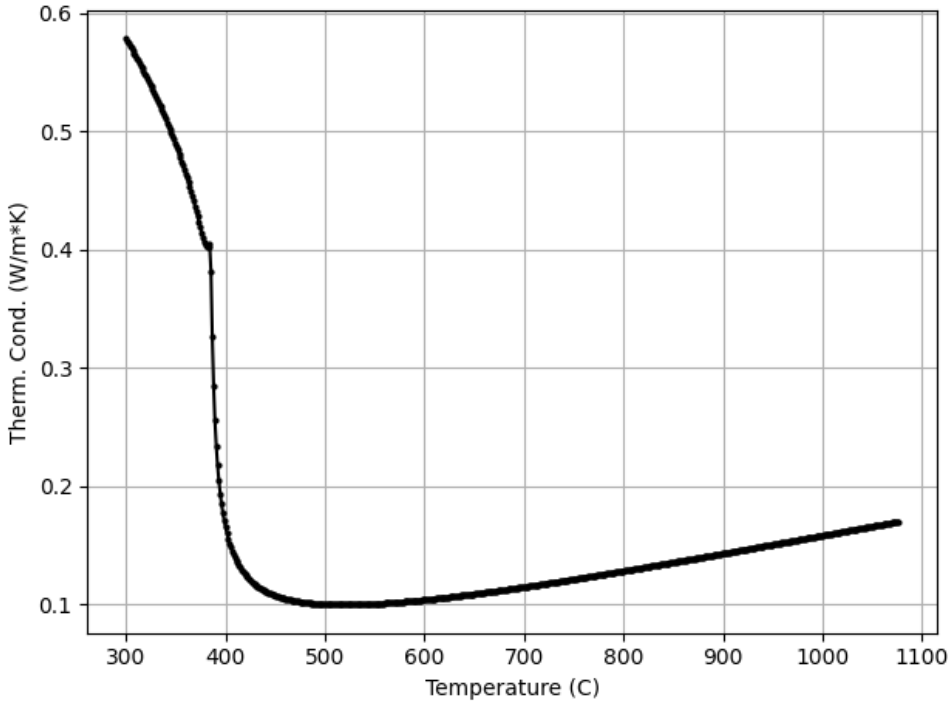

Figure A. 10. Thermal conductivity of scH2O at 25 MPa (NIST, 2026)

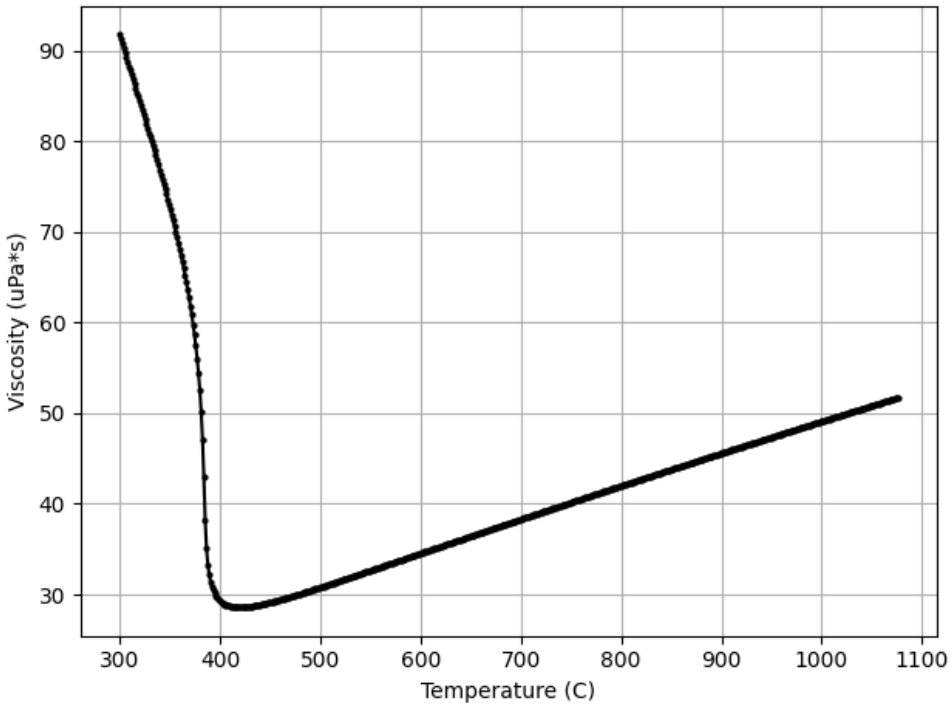

Figure A. 11. Viscosity of scH2O at 25 MPa (NIST, 2026)

.

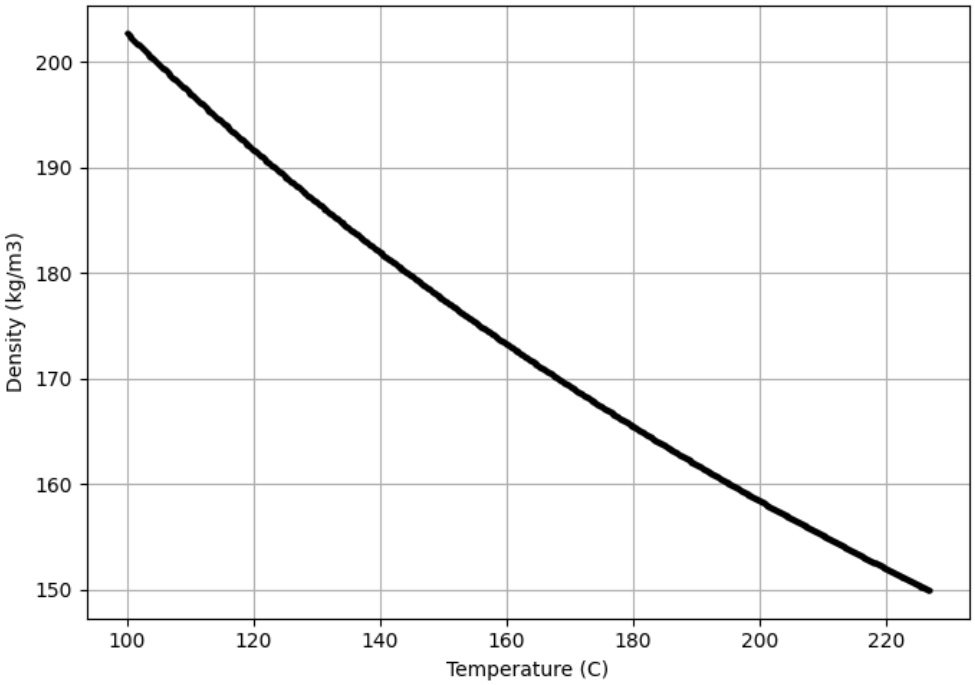

Figure A. 12. Density of supercritical CO (25 MPa, 100-220°C) (NIST)

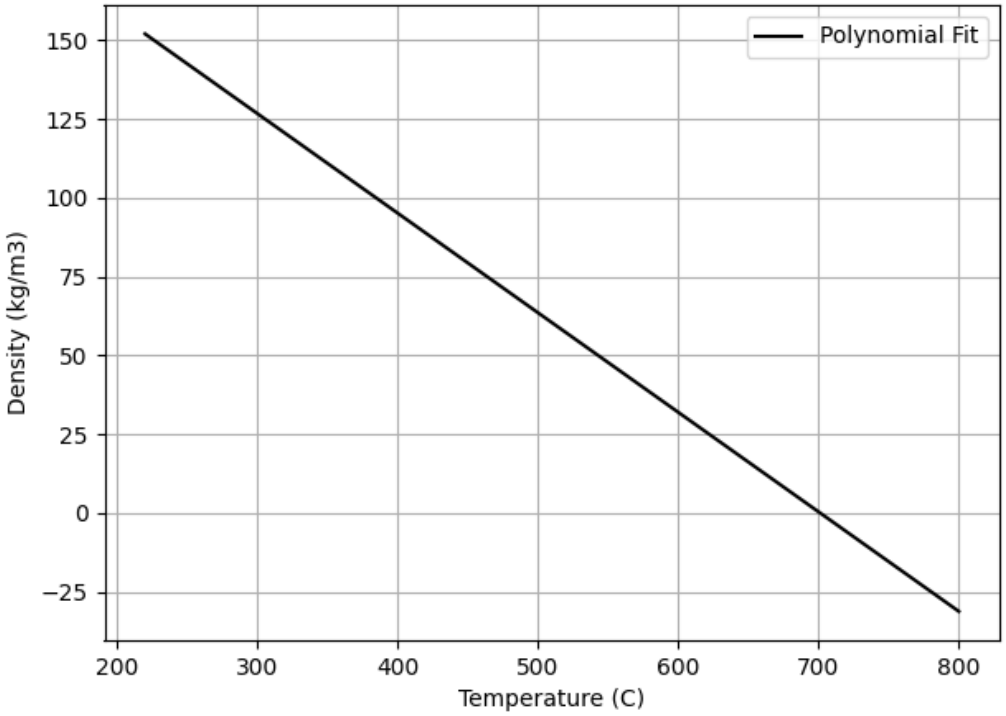

Figure A. 13. Extrapolated density of supercritical CO

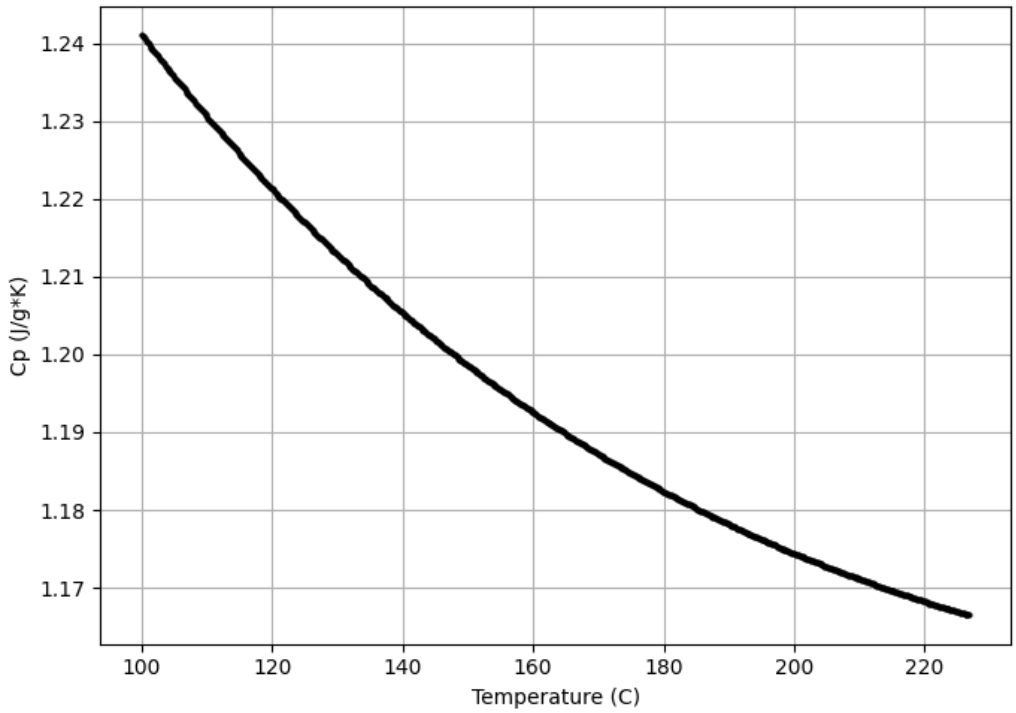

Figure A. 14. Specific heat of supercritical CO (NIST)

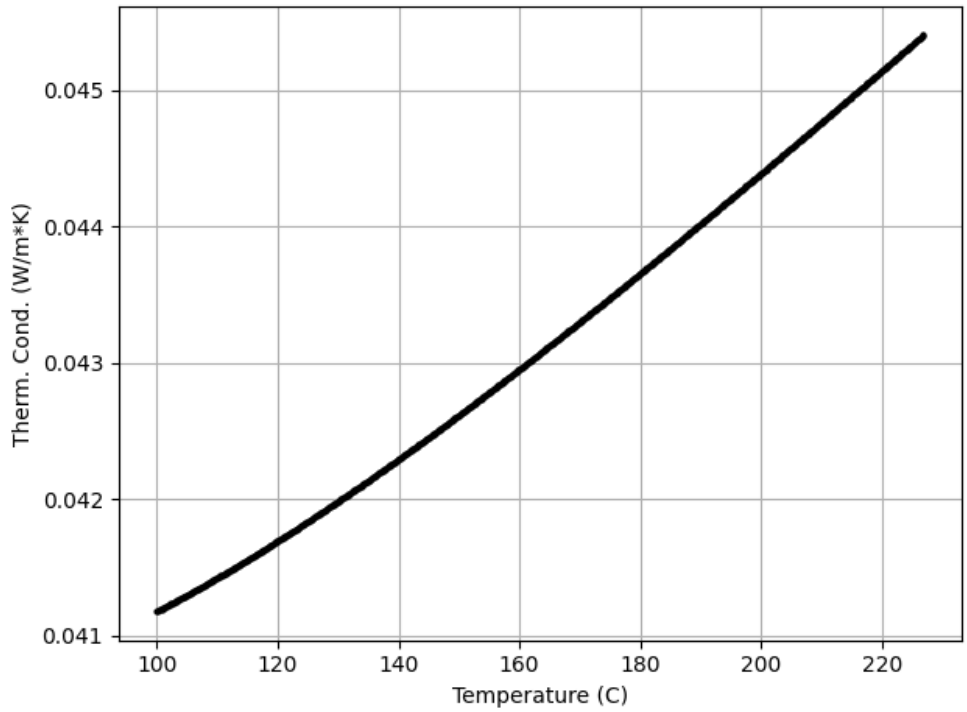

Figure A. 15. Thermal conductivity of CO (NIST)

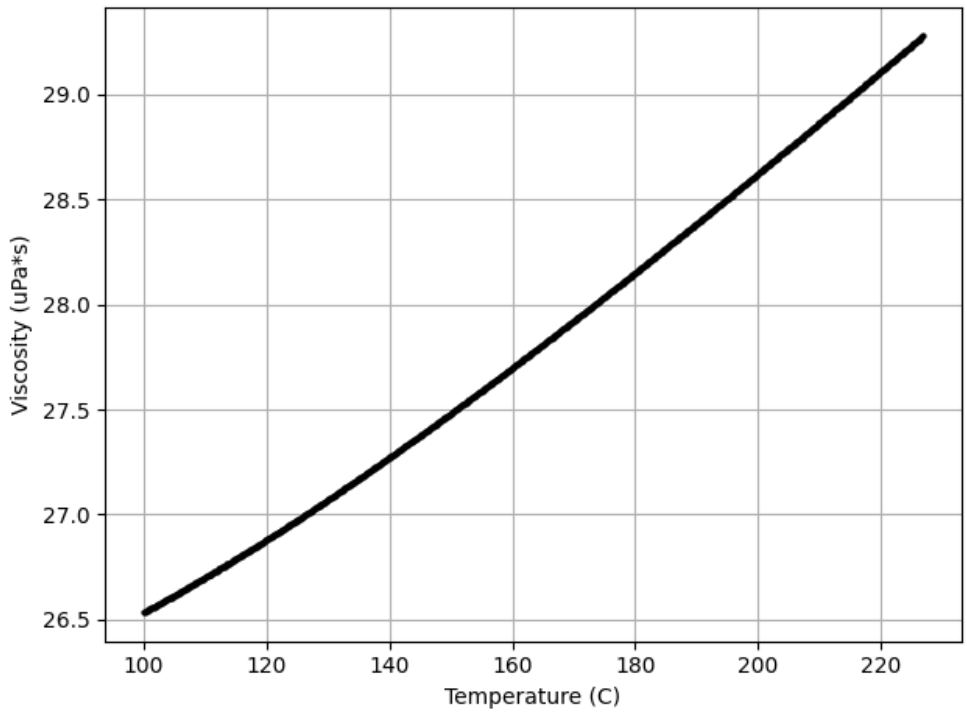

Figure A. 16. Viscosity of CO (NIST)

7.6. Mixture flow rate calculation – detail

The fuel inlet transports both H_2O and C_2H_5OH as a mixture. It was estimated from the NIST thermophysical properties data at 25 MPa and 400 C [105] that

$$\rho_{C_2H_5OH} = 0.772\ g/ml$$

$$\rho_{H_2O} = 1.008\ g/ml$$

Using the mass-weighted mixing law for the 5 mol% ethanol solution,

$$\rho_{mixture} = 972.763\,\frac{kg}{m^3}$$

The density was held constant across all cases which introduces a maximum mass flow rate deviation by 1.4% at the lowest flow rate case. Multiplying the $\rho_{mixture}$ with the total mixture flow rate of 10 ml/min, mass flow rate of the fuel line mixture was obtained to be

$$\dot{m}_f = 0.000162\ kg/s$$

The mol fraction of ethanol was calculated from the 5 mol% ethanol.

$$x_{C_2H_5OH} = f * 5\ mol\%$$

Where f is the flow rate percentage for each case. The mass fraction of C_2H_5OH was obtained from

$$y_{C_2H_5OH} = \frac{x_{C_2H_5OH} \cdot M_{w,C_2H_5OH}}{x_{C_2H_5OH} \cdot M_{w,C_2H_5OH} + x_{H_2O} \cdot M_{w,H_2O}}$$

Where x_{H_2O} was obtained from $1 - x_{C_2H_5OH}$. y_{H_2O} in the fuel line was also the remainder of the fraction; $1 - y_{C_2H_5OH}$.

The calculation for the oxidant line consists of the flow rate in the air line and the water line. It was assumed that air is composed of 79% N_2 and 21% O_2. Using the mass-weighted density of air $\rho_{air} = 119.87\ kg/m^3$ at 25 MPa and 400 °C, and assuming the air to be near-ideal gas, the $\dot{m}_{air}$ was calculated as

$$\dot{m}_{air} = \frac{Q_{air}[SLPM]}{\bar{v}_{standard}} * 60 * M_{w,air}$$

Where $\bar{v}_{standard}$ is the specific volume of air on the standard conditions (1 atm, 25 °C). For the water line, $\dot{m}_{H_2O}$ was obtained from

$$\dot{m}_{H_2O} = \rho_{H_2O\ (25\ MPa, 400\ °C)} * Q_{H_2O}$$

Since Q_{H_2O} was kept constant at 10 ml/min,

$$\dot{m}_{H_2O} = 0.00169\ kg/s$$

Thus, the total mass flow rate of air and water in the oxidant line was obtained from

$$\dot{m}_{oxidant} = \dot{m}_{air} + \dot{m}_{H_2O}$$

The fractions of the species in the oxidant line were obtained from

$$y_{N_2} = \frac{y_{N_2,relative\ to\ air} * \dot{m}_{air}}{\dot{m}_{oxidant}}$$

$$y_{O_2} = \frac{y_{O_2,relative\ to\ air} * \dot{m}_{air}}{\dot{m}_{oxidant}}$$

$$y_{H_2O} = 1 - y_{N_2} - y_{O_2}$$

The calculated fuel and oxidant inlet flow rates, temperatures, and species fractions are tabulated below for each of the simulated 49%, 56%, 69%, and 100% of 5 mol% ethanol flow rate cases.

7.7. Residual plots

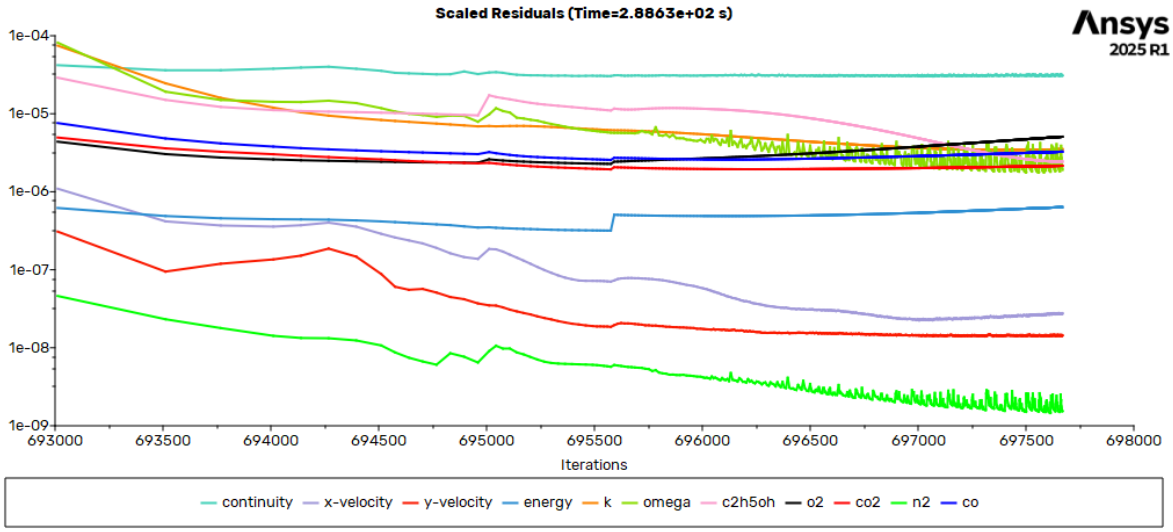

Figure A. 17. Residual history - 56%

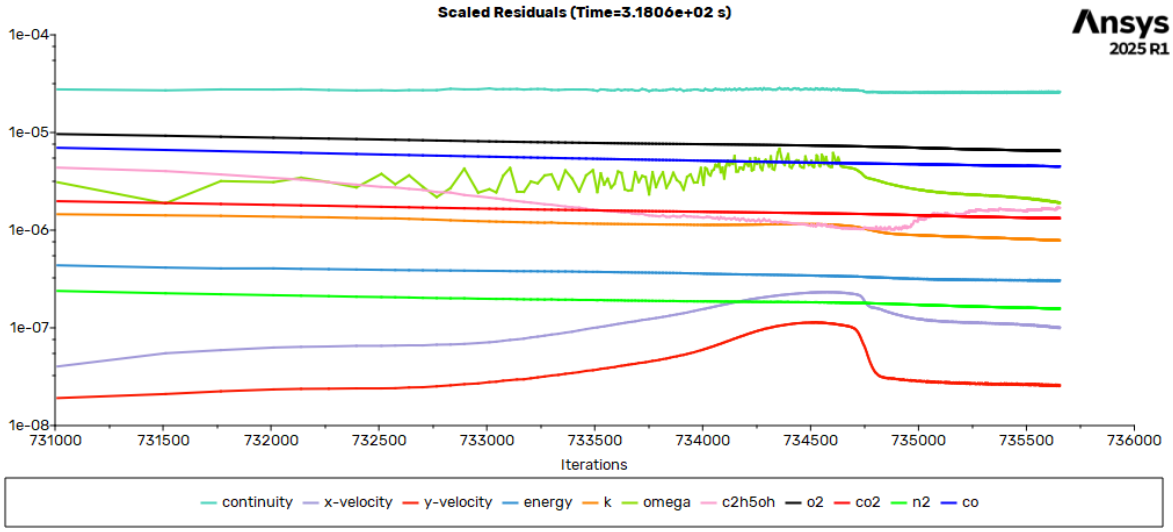

Figure A. 18. Residual history - 69%

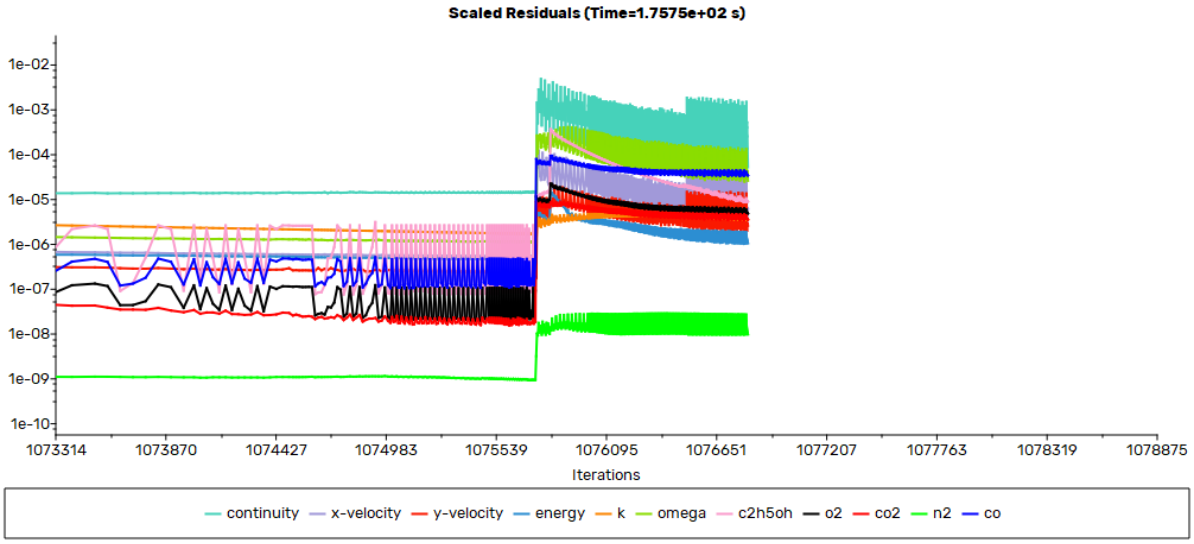

Figure A. 19. Residual history, 100%

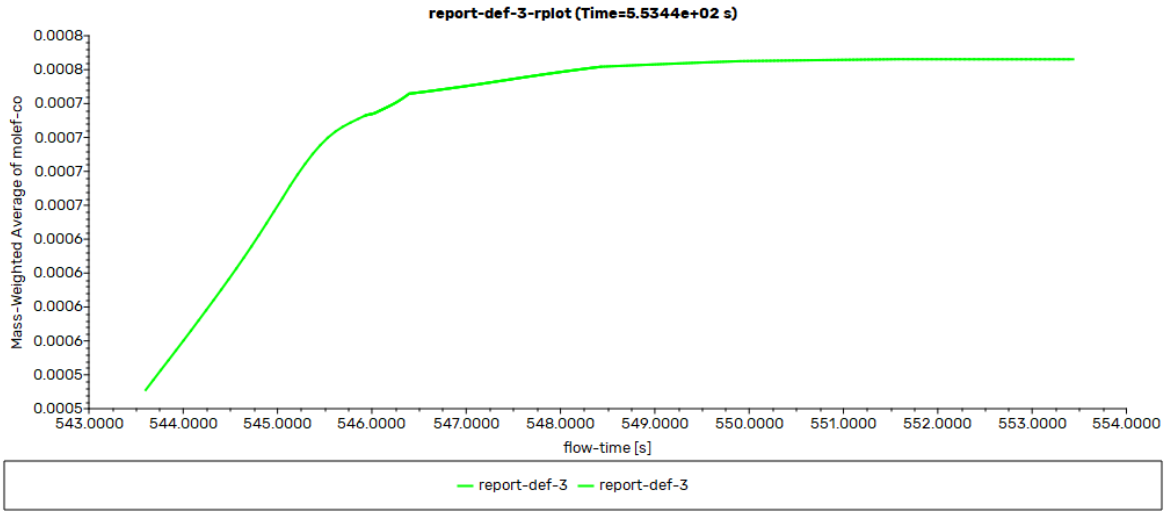

Figure A. 20. CO monitor per time step - 49% flow rate

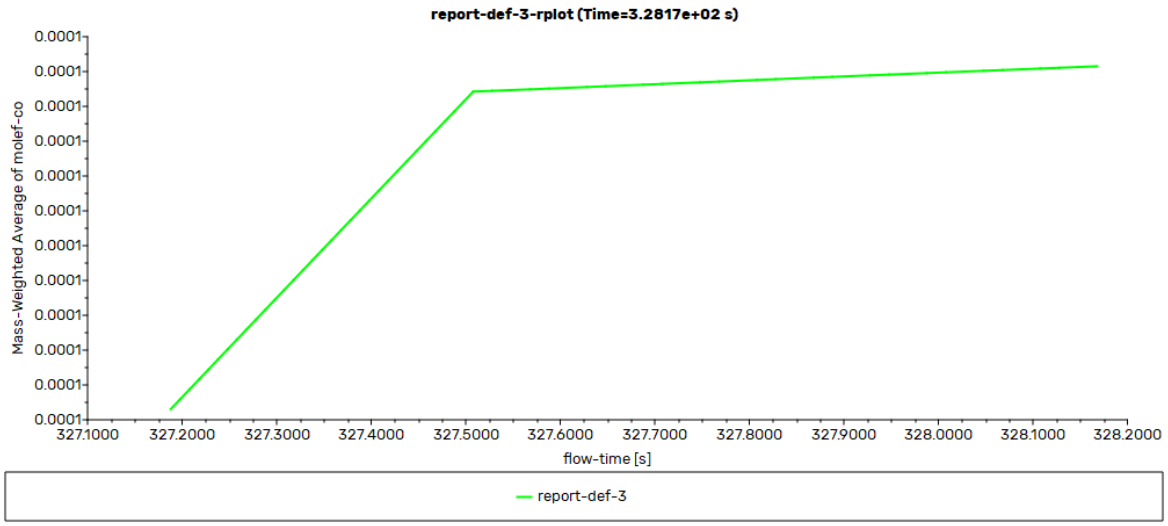

Figure A. 21. CO monitor per time step - 56% flow rate